

Preparations for Next Generation Liquid-phase Studies of Super-heavy Elements

*Combining the New Flow Solvent Extractor
with the SISAK Alpha-Detection System*

Solveig Birgitte Aker Wulff



Thesis for the Master's
Degree in Chemistry

60 study points

Department of Chemistry
Faculty of Mathematics and Natural Sciences

UNIVERSITETET I OSLO

10/2017

Preparations for Next Generation Liquid-phase Studies of Super-heavy Elements

*Combining the New Flow Solvent Extractor with the
SISAK Alpha-Detection System*

Solveig Birgitte Aker Wulff

2017

Preparations for Next Generation Liquid-phase Studies of Super-heavy Elements

Combining the New Flow Solvent Extractor with the SISAK Alpha-Detection System

Solveig Birgitte Aker Wulff

<http://www.duo.uio.no/>

Trykk: Representralen, Universitetet i Oslo

Abstract

The work presented in this master thesis was part of a collaborative effort to build and test the next generation of liquid-phase apparatuses for studies of the super-heavy elements. The performed work was; to set up and commission a new experiment station for tests and development of super-heavy element (SHE) chemistry apparatus at the cyclotron at the Nuclear Physics Institute in Řež, Czech Republic; investigate production yields of relevant SHE homologues; test performance of a new membrane phase separator (gas/liquid and liquid/liquid) system with Re-isotopes; test if the old SISAK alpha liquid scintillation detector-cells could be used together with the new system; participate in a measurement to enhance the determination of the cross section excitation function for making ^{266}Bh with a ^{23}Na ion beam. Some more details are given below.

The SHE homologues for chemistry tests and apparatus development in Řež were produced by irradiating natural target foils with a $^3\text{He}^{+2}$ beam. The cross sections of $^{88/90/95\text{m}}\text{Mo}$, $^{169/170/173}\text{Hf}$, $^{172/173/174}\text{Ta}$, $^{174/175/177}\text{W}$ and $^{178/179}\text{Re}$, produced from natural foils were investigated.

In RIKEN, investigations were performed on how short-lived ^{170}Re and ^{174}Re can be transferred from the carrier gas into liquid phase with a “Membrane Degasser”, and how rapid they could be extracted and separated in the new “Flow Solvent Extraction” system was investigated. The transport times and chemical yields through this system was investigated. The possibility of combining the Membrane Degasser and Flow Solvent Extraction system with the liquid scintillation detectors previously used in SISAK experiments was investigated. The systems worked well together, as long as the pumping mechanism of the detector system was placed after the detector-cell, causing there to be close to no backpressure affecting the membrane system.

The production cross section and excitation function of ^{266}Bh was investigated for future use in chemical studies of bohrium in RIKEN with the GARIS preseparator. The reaction $^{248}\text{Cm}(^{23}\text{Na},\text{xn})^{271-\text{x}}\text{Bh}$ at 135,3 MeV incident beam energy was measured to be $15.8^{+20.8}_{-10.2}$ pb, confirming the maximum cross section of $^{248}\text{Cm}(^{23}\text{Na},\text{xn})^{266}\text{Bh}$ to be at 130.7 MeV incident beam energy.

Acknowledgements

The work during this thesis has for me been a lifetime experience, which I would like to give my gratitude to my supervisor Jon Petter Omtvedt for making possible. He has shown support and guided me through this master's degree and has been invaluable for its completion. I would like to thank him for his invaluable constructive feedback on this thesis and for answering any question I had.

I would like to thank the people I worked together with from the Czech Technical University in Prague and Nuclear Physics Institute of the Czech Academy of Sciences for their help, collaboration and the possibility to work at their facilities.

I would also like to thank Hiromitsu Haba, Yukiko Komori and the rest of the amazing people in the RIKEN research group, who were really welcoming to allow me to participate in their beam time experiments in RIKEN, Japan. Also thank you so much for answering any questions I had during the writing of this thesis.

Big thanks goes to Tor Bjørnstad, who helped me with the analysis at short notice when I was out of my depth.

I would like to acknowledge and thank a lot of my friends for being my support during the work, and especially during my writing. I won't list you all by names, but know that you all have been helpful! Also thank you all for being my personal English dictionaries and correcting my grammar. Special thanks to my friend Daniel Eriksen, for being my wall to bounce ideas and questions at whenever I felt progress was slow or at standstill. Also thank you Hans Lerum and Vegard Ovland for reading through my text to give me feedback.

Contents

Abstract	V
Acknowledgements	VII
Contents.....	IX
1 Introduction	1
2 Background and theory	3
2.1 Background.....	3
2.2 Theory.....	6
2.2.1 α -particles and detection	6
2.2.2 γ -rays and interaction with matter	10
2.2.3 Cyclotrons, linear accelerators and particle transport	11
2.2.4 Target chamber, gas-jet transport, recoil transfer chamber and physical preseparator	14
2.2.5 Gas-jet transport and chemistry apparatus	15
2.2.6 Super-heavy element research.....	16
3 Experiments performed in Řež, at the Isochronous Cyclotron U-120M.....	19
3.1 Background.....	21
3.2 Methods and instrumentation	22
3.2.1 The isochronous cyclotron U-120M	22
3.2.2 Target chamber and gas-jet system	23
3.2.3 Germanium detector	26
3.3 Analysis methods.....	27
3.3.1 Production of homologues	27
3.3.2 Beam energy loss and cross sections.....	27
3.4 Results and discussion	30
3.4.1 Produced nuclei from the cyclotron	30
3.4.2 Gas-jet transport yields.....	31
3.4.3 Cross sections	33
3.4.4 Errors/uncertainty	33
4 Tests of the new liquid-liquid membrane phase separator system connected to the physical preseparator GARIS and on-line SISAK liquid scintillation system.....	35
4.1 Background.....	37
4.2 Methods and instrumentation	38
	IX

4.2.1	RIKEN Heavy Ion LINAC (RILAC) and GARIS	38
4.2.2	Gas-jet system	39
4.2.3	Membrane liquid-liquid extraction system	39
4.2.4	Germanium detector	40
4.2.5	Rhenium experiment	41
4.2.6	Test of connecting the FSE/MPS system to the SISAK liquid scintillation detector system	44
4.3	Data acquisition and analysis methods	50
4.3.1	Gamma spectra	50
4.3.2	Transport time measurements	50
4.4	Experiments and results	56
4.4.1	Rhenium experiments	56
4.4.2	Connecting of the membrane system and SISAK detector system	62
4.5	Discussion	64
4.5.1	Rhenium	64
4.5.2	Connecting of the membrane system and SISAK detector system	64
5	Investigation of the maximum cross section of the $^{248}\text{Cm}(^{23}\text{Na},\text{xn})^{271-\text{x}}\text{Bh}$ reaction	67
5.1	Background	69
5.2	Methods and instrumentation	71
5.2.1	RIKEN Heavy Ion LINAC (RILAC), GARIS and gas-jet transport system	71
5.2.2	Detector system MANON II	71
5.3	Analysis, experiment and results	73
5.3.1	Measured α -correlations	73
5.3.2	Decay properties of ^{266}Bh	76
5.3.3	Cross section of ^{266}Bh	77
5.4	Discussion	78
6	Conclusion and future perspectives	81
	References	83
	Appendix A - Acronyms and abbreviations	87
	Appendix B – Propagation of uncertainty	89
	Appendix C - Řež experiments	91
	Calculations and analysis	91
	Calculations for the corrected values from the γ -spectra analysis.	91

Calculations for energy loss in the path through the target chamber.	91
Cross section calculations	92
Pictures of equipment and instruments	93
HPGe-spectrum with lutetium target.....	95
Appendix D – Rhenium experiment in RIKEN	97
Calculations and analysis	97
Calculations for the corrected values from the γ -spectra analysis.	97
Analysis of the transport time measurements	98
HPGe-spectrum from rhenium production.....	106
Pictures of equipment and instruments	107
List of chemicals	109
Appendix E – Bohrium experiment in RIKEN	111
Pictures of equipment and instruments	111
List of Figures	113
List of Tables.....	119

1 Introduction

The possibility to work towards learning more about the building blocks of our universe was part of what motivated me to take on this assignment. I have always been fascinated by the concept of creating elements that does not appear in nature, and especially those that disappear after a few seconds after they have been created. To be able to work towards performing chemistry with these special elements was an exciting idea, giving me an opportunity to participate in this really interesting field of study.

The second chapter of this thesis gives an overview of the background for the research performed during this assignment. It also include a review of the relevant theory that was needed in order to understand the methods and instrumentation used in this thesis. The aim of this thesis was directed at preparations to build and test the next generation of liquid-phase apparatuses for studies of the super-heavy elements. The research presented here is clearly divided into three different parts. These three parts are all directed towards performing liquid phase chemistry with super-heavy elements, but are distinctly different in instrumentation and execution. Therefore, they are presented in separate chapters.

In the third chapter of this work, the possibilities of producing a significant amount of the homologues of the SHEs to perform future model experiments was investigated. The homologues were produced by irradiating natural targets with a $^3\text{He}^{+2}$ beam. Aluminum catcher foils was used to study the total possible available amounts of the relevant homologues. A gas-jet system with He/KCl aerosols was used to transport the radionuclides to a nearby room. The transport yield of the gas-jet system was studied by comparing the produced amounts of the same nuclei measured with both the aluminum foil and the gas-jet collection. All the investigated homologue nuclei were β -emitters with subsequent γ -rays, and the γ -rays were detected using an HPGe-detector.

Using the amounts of nuclei measured with aluminum catcher foils, the cross sections of the molybdenum isotopes ($^{95\text{m}}\text{Mo}$, ^{90}Mo and ^{88}Mo), hafnium isotopes (^{173}Hf , ^{170}Hf and ^{169}Hf), tantalum isotopes (^{174}Ta , ^{173}Ta and ^{172}Ta), tungsten isotopes (^{177}W , ^{175}W and ^{174}W) and rhenium isotopes (^{179}Re and ^{178}Re) produced from natural zirconium-, ytterbium-, lutetium-, hafnium-, and tantalum foils were calculated.

The fourth chapter of this work contains the study of how short-lived rhenium isotopes (^{170}Re and ^{174}Re) can be transferred from the carrier gas into liquid phase with a “Membrane Degasser” and how rapid they could be extracted and separated in the new “Flow Solvent Extraction” system developed to replace the centrifuges in the liquid-liquid extraction system SISAK. The gas-jet system’s transport yield of ^{174}Re was investigated. In addition, the transport times of ^{170}Re through the system was investigated by measuring each added step in the total system. The chemical yield of rhenium after going through the Membrane Degasser, Flow Solvent Extraction and Membrane Phase Separator was investigated. The results from the measurements of the chemical yields has been analyzed and calculated by Y. Komori [1, 2].

The possibility of combining the Membrane Degasser and Flow Solvent Extraction system with the liquid scintillation detectors previously used in SISAK experiments was investigated. It was discovered that the systems worked well together as long as the pumping mechanism of the detector part of the system was placed after the detector cell, causing there to be close to no backpressure affecting the membrane system.

The fifth chapter of this work contains the results from participation in a “real” super-heavy element experiment: The production cross section and excitation function of ^{266}Bh was investigated. I.e. the reaction $^{248}\text{Cm}(^{23}\text{Na},\text{xn})^{271-\text{x}}\text{Bh}$ at 135.3 MeV incident beam energy (lab) was measured. The purpose was to get a clearer picture of the excitation function, in particular where the maximum is located. This was investigated for future use in chemical studies of bohrium in RIKEN with the GARIS preseparator. All the analysis and calculations in this part has been performed by H. Haba [3, 4].

2 Background and theory

2.1 Background

In the research of the super-heavy elements, atomic number 104 and up, the main objective is to investigate their basic chemical and physical properties. This is done to verify that they behave according to the systematic placement of these elements in the periodic table. The first time the elements was successfully arranged by atomic weight, grouping the similar elements under each other and leaving holes where no element fit, was in 1869 [5] by Mendeleev. Mendeleev's periodic table predicted more elements and their properties to be discovered. Since then, many more elements have been discovered and gradually filled out the holes in the table. Although there are no more holes in the periodic table, new elements are added at the bottom: Heavier elements are synthesized in large accelerator-laboratories and there is a constant push to "discover" the next one. For these super-heavy elements, their chemical properties is of the greatest interests, since if the predictions about their properties are correct, it confirms that our current understanding and models hold true even for the extreme cases the super-heavy elements represent.

The main goal of this thesis is to contribute to preparations for a future super-heavy element chemistry experiment, with either element 106 seaborgium or 107 bohrium. Such experiments is expected to be performed at the linear facilities at Rikagaku Kenkyusho (RIKEN) (translated: Institute of Physical and Chemical Research) in Wako-shi near Tokyo, Japan. Provided that the system performs convincingly, one of the systems that can be used for such chemistry studies could be the liquid-liquid extraction system investigated in this thesis, which uses membranes for phase separation instead of the complicated centrifuges formerly used (the "SISAK" system). Part of the work performed in this thesis was to investigate if the detector system used with the SISAK system could be used with the new membrane-based system.

Leading up to this work, there was planned to set up an experiment-facility in Řež in the Czech Republic. At this facility, experiments with the elements in the same group as the super-heavy elements, called homologues (Figure 1), would be performed. This gave the opportunity to participate in the commissioning experiments at the facility as a part of this thesis. The commissioning entailed testing out the production of many of the homologues, and isotopes of Tc, Re, W, Mo, Ta and Hf were produced.

Group→	1	2	3	4	5	6	7	8	9	10	11	12	13	14	15	16	17	18
↓Period	1	2																2
1	H																	He
2	Li	Be											B	C	N	O	F	Ne
3	Na	Mg											Al	Si	P	S	Cl	Ar
4	K	Ca	Sc	22	23	24	25	26	27	28	29	30	31	32	33	34	35	36
				Ti	V	Cr	Mn	Fe	Co	Ni	Cu	Zn	Ga	Ge	As	Se	Br	Kr
5	Rb	Sr	Y	40	41	42	43	44	45	46	47	48	49	50	51	52	53	54
				Zr	Nb	Mo	Tc	Ru	Rh	Pd	Ag	Cd	In	Sn	Sb	Te	I	Xe
6	Cs	Ba	La	72	73	74	75	76	77	78	79	80	81	82	83	84	85	86
				Hf	Ta	W	Re	Os	Ir	Pt	Au	Hg	Tl	Pb	Bi	Po	At	Rn
7	Fr	Ra	Ac	104	105	106	107	108	109	110	111	112	113	114	115	116	117	118
				Rf	Db	Sg	Bh	Hs	Mt	Ds	Rg	Cn	Nh	Fl	Mc	Lv	Ts	Og
			*	58	59	60	61	62	63	64	65	66	67	68	69	70	71	
				Ce	Pr	Nd	Pm	Sm	Eu	Gd	Tb	Dy	Ho	Er	Tm	Yb	Lu	
			*	90	91	92	93	94	95	96	97	98	99	100	101	102	103	
				Th	Pa	U	Np	Pu	Am	Cm	Bk	Cf	Es	Fm	Md	No	Lr	

Figure 1: Periodic table of element, where the bold square marks the homologues of the super-heavy elements 104-108. Figure reprinted from source [6].

To be able to do liquid chemistry with nuclei with short half-lives, experiments would be performed on-line with a continuous liquid-liquid extraction system. This system is called SISAK, which is an acronym for Short-lived Isotopes Studied by the AKUFVE method [7]. AKUFVE is a Swedish acronym for arrangement for continuous investigations of distribution ratios in liquid-liquid extraction. It is a system consisting of custom-made centrifuges made for fast and continuous separation of organic and aqueous phase after a liquid-liquid extraction.

In continuous liquid-liquid extraction, the radioactivity is transported with a carrier-gas which is dissolved into a diluted acid. The gas is then removed with a degasser, leaving the activity in the aqueous phase. The element under study is then extracted into an organic phase before the phases are separated and measured. The properties learned from the extraction tells something about the elements' chemistry. A simple SISAK setup is shown in Figure 2.

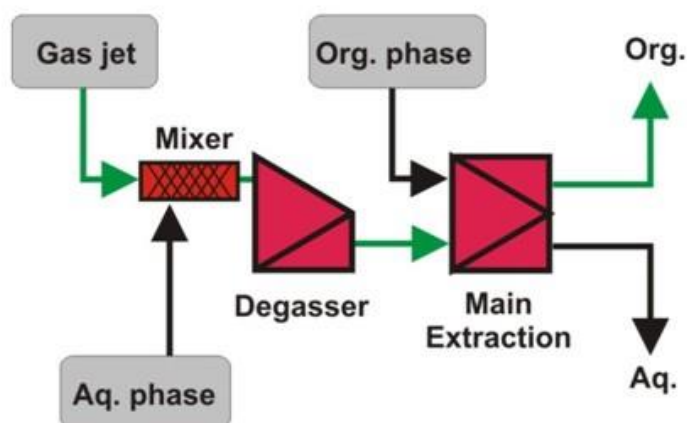


Figure 2: Schematic of a simple SISAK setup for continuous liquid-liquid extraction. Figure reprinted from source [8].

The SISAK system previously used in experiments with superheavy elements consisted of up to five centrifuges for phase separation and degassing. Combined with a custom made scintillation detector system for α -liquid scintillation with flow-through cells, the SISAK system has been used to successfully perform liquid chemistry with superheavy elements [7]. To operate and service the custom built centrifuges is not trivial, making such a complex setup

both labor intensive and demanding. During about ten years of SHE experiments with the SISAK system, it became more and more obvious that although the system works, and is the fastest available chemistry apparatus for SHE studies in liquid phase in existence, a more stable system that are much easier to operate is needed for experiments on elements beyond $Z=105$. Such experiments need to run continuously for weeks or longer [9].

A new chemical separation system has recently been developed for use in experiments with superheavy elements, where the centrifuges are replaced with simple membrane systems [1, 10-12] for both degassing and phase separation. The first idea to use membranes instead of centrifuges in continuous liquid-liquid extraction was developed in Mainz in collaboration with Institut für Mikrotechnik Mainz to use with MicroSISAK [13, 14]. Based on the idea developed for MicroSISAK, a prototype Membrane Degasser (MDG) in a more practical size than for MicroSISAK was developed for the ordinary SISAK system and tested at Oslo Cyclotron Laboratory (OCL) [9, 15]. In addition to simplifying the SISAK system, its development enabled high yields at lower flow-rates (down to 0.1-0.2 mL/s). Another MDG, working at high aqueous flow-rates (0,1-0,4 mL/s) was later developed and tested in a collaboration between the Oslo group and Japanese colleagues from Tokai (K. Ooe et al.) and RIKEN (Y. Komori et al.) [11]. Recently, RIKEN has developed a new MDG by modifying the MDG from UiO/JAEA collaboration [16]. This new MDG has a high efficiency at low flow-rates ~ 1 mL/min. In the work presented here, this MDG was investigated to determine if the transport time through the device is fast enough for super-heavy element experiments on nuclei with only a few seconds half-life.

Experiments with 107 bohrium's heavy homologue was performed together with a research group lead by H. Haba in RIKEN, Japan, where the transport yields, transport times and chemical yields of the were investigated with short-lived nuclei to see if the new membrane system could be optimized for use in a bohrium experiment.

This membrane system has a flow-rate of ~ 1 mL/min, compared to the high (0.3-1.0 mL/sec) flowrate of the centrifuge system. In this work it was investigated if the old detector system used with SISAK and in the high flow-rate regime could be adopted to the new membrane based system operating at much lower flow-rates. These tests were performed in collaboration with Y. Komori, who has developed the new membrane separation system, during a four week visit to her laboratories and the RIKEN accelerator facility in Japan.

During the work in Japan, the opportunity to participate in a physics experiment with bohrium arose. This provided experience and insight in a full-scale experiment with a super-heavy element. This hands on experience, where a physical preseparator was used to remove most of the unwanted byproducts from the nuclear reaction as is required for chemistry experiments, has given better insight on how such experiments are performed. The experiment measured the excitation function of the bohrium isotope ^{266}Bh , which is necessary to know in order to select the right beam-energy for future chemistry experiments with on this element.

2.2 Theory

2.2.1 α -particles and detection

Liquid scintillation

There exist many methods for radiation detection. These methods vary with the type of radiation and the purpose of the detection. When studying super-heavy elements, it is wanted ideally to detect every single occurrence, and to detect all the occurrences with a good energy resolution. This will enhance the identification of the real events from the background made by unwanted by-products in the nuclear reactions. Liquid scintillation (LS) detection is one method for detecting radioactivity. The scintillation cocktail consists of an organic solvent and a solute/scintillator. When an α -emitting nuclei decays, it sends out a helium nucleus [17]. The α -particle is charged, and in liquid scintillation solution it will interact (primarily) with the solvent molecules in the cocktail, which leads to ionization and excitation of the solvent. When the solvent then deexcite, the energy will transfer to the scintillator, which then transfers the energy and sends out light.

Because the relative high mass and charge of the α -particle, it will cause a high density of ionizations and excitations, and will have a low ability to penetrate matter. The amount of energy transferred to the surroundings per unit distance is defined as the Linear Energy Transfer (LET) value [17]. The high ionization density in the path of the α particle will give ionizing quenching [7]. β -particles and electrons in general has a lower LET-value, and will distribute the excitations and ionizations over a larger volume. Because of this, there are less ionizing quenching for electrons, and the light-pulse emitted will have a higher intensity per unit particle kinetic energy when compared to the intensity of the pulses from α -radiation. This causes the amount of light generated from an α -particle compared to an electron (from β -decay, or Compton scattering of γ -radiation) to be about 10 times lower [18]. The lower amount of light from the α -particle causes the energy from the α -, β - and γ -radiation to be in the same order of magnitude, and the light output of a 4 MeV α -particle will be observed as the same as a 0,4 MeV β -particle. Because of this, a method is needed to separate between the light from α - and β -/ γ -events. How this is achieved is explained in the following pages.

Delocalized π -electrons in the solute are excitable by radiation, and when the scintillator de-excites, it emits photons. Internal conversion is the name of transition between excited states where the multiplicity is the same, $S_3 \rightarrow S_1$, whilst intersystem crossing is the transition between states where the multiplicity is different, $T_1 \rightarrow S_0$, as seen on Figure 3. Both the single and triple excited states send out light which is possible to detect with a photomultiplier tube. Deexcitation from the first excited level of the singlet series and to the ground state gives emission of a fast and short light-pulse (fluorescence). The deexcitation from the first level of the triplet series to the ground level is delayed by intersystem crossing, and gives a delayed emission of a longer light-pulse (phosphorescence) [19].

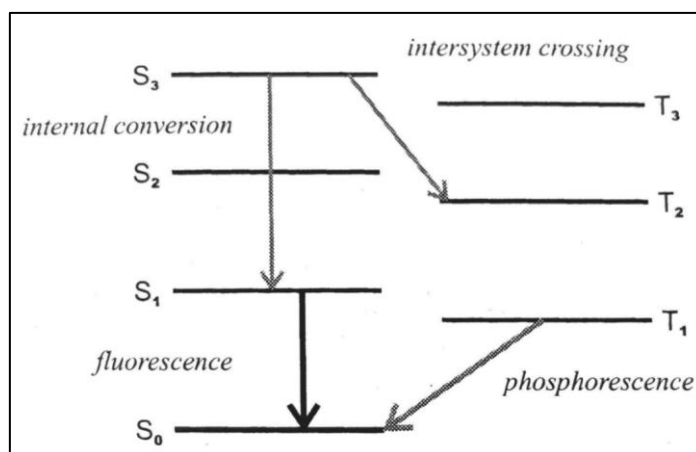


Figure 3: Schematic of the different possible deexcitation paths of the excited states of an aromatic compound's π -electron system. Figure reprinted from [1].

As the time before an excited singlet state deexcite is in the magnitude of 10^{-9} to 10^{-7} seconds [20], the fluorescence will be emitted promptly, and is the fast component in scintillating light. The time before a triplet excited state decay is much longer, of the magnitude of 10^{-4} to 10 seconds, as it is a forbidden transition with spin change of the electron [18]. The amount of triplet excited states increases with the LET-value, which means that α -particles produces a higher percentage triplet excited states than both β - and γ - radiation [21]. These triplet excited molecules mainly decay by interacting with another triplet excited molecule. This will, as shown in Equation 1, give one molecule in the ground state and another in a singlet excited state.

$$T_1 + T_1 = S_1 + S_0 \quad (1)$$

The singlet excited state then decays, producing the slow component of the scintillator light (Figure 4). Analyzing the light from the scintillator with regards to the time sinking-time of the light-pulse is called Pulse-Shape Discrimination (PSD). In the optimal case, PSD can eliminate β - and γ -particles with a certainty of 99.9 % [18]. This gives the possibility to do α -spectrometry close to entirely without the overlap of β or γ from i.e. background radiation.

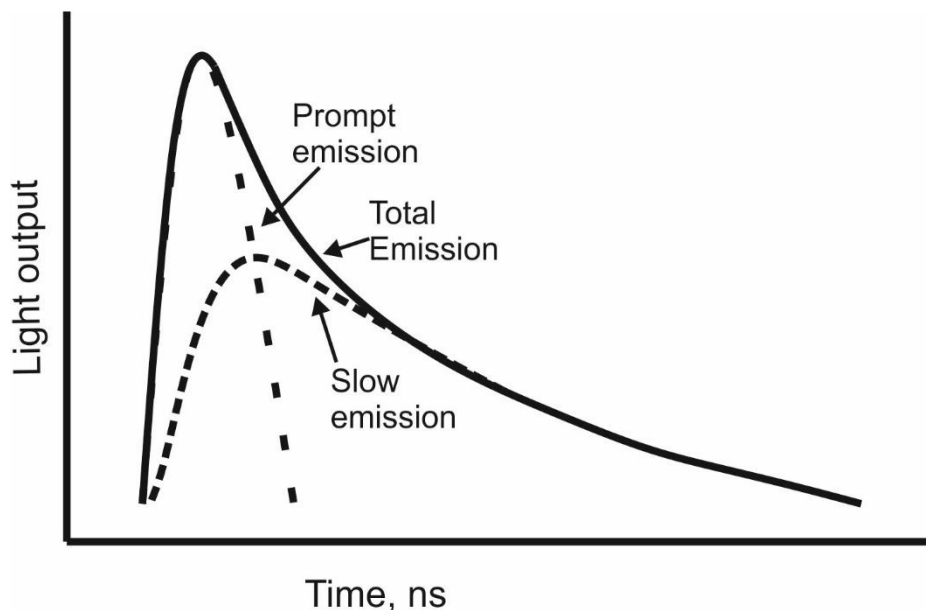


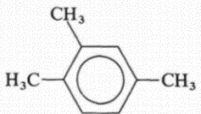
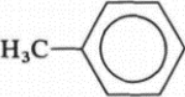
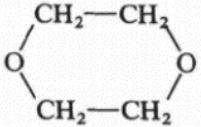
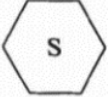
Figure 4: Graph illustrating a scintillator light pulse with a fast and a slow component and the total light output.

Transfer of excitation energy to the light emitting scintillator molecules can be hindered in several ways. This effect is called quenching. Some examples of quenchers are dissolved oxygen in the cocktail or the cocktail having a color [19]. Quenching caused by light-absorbing components stops the light emitted from reaching the detector, while chemical quenching is when the energy is stopped from transferring from solvent to scintillator.

Scintillator solution

The solvent in the scintillation solution is important for dissolving the sample and for absorbing the energy from the nuclear radiation [19]. The initial excitation happens in the solvent, and it is important that the solvent has an efficient production of excited states. Molecules with available low-lying energy levels in addition to nonbinding electrons (π) are the type of molecules that easily produce excited states [19]. Effective solvents of this type are aromatic-type compounds, which also are liquids at room temperature. A list of commonly used solvents are given in Table 1.

Table 1: A list of commonly used solvents and their structure [19].

Solvent	Structure
1,2,4-Trimethylbenzene	
p-Xylene	
Toluene	
Benzene	
Dioxane	
Cyclohexane	

The solute in the scintillation solution is a highly efficient fluor, and is added since most solvents alone are not efficient scintillators [19]. The solute accepts the energy from the excited solvent molecules, and gets excited to one of its excited states. The solute will then return to the ground state and, as mentioned earlier, will release heat and in some instances, fluorescence. The concentration of the solute influence the efficiency of the energy transfer from the solvent, as the ratio of solvent and solute has to be as ideal as possible for transfer of excitation energy [18, 19].

A secondary solute can be added to the scintillation solution to increase the scintillation efficiency. The ratio between the secondary and primary solute will affect the amount of self-absorption in the scintillation cocktail. The right amount of secondary solute will decrease the amount of self absorption, increasing the scintillation efficiency [19].

Liquid scintillation detection

The light emitted from an α -event in the scintillation solution, gives intense enough light-pulses to be detected with only one scintillation detector, unlike low energy β -particles, which requires two detectors and a noise reduction by coincidence measurements [19]. To ensure that as much of the light from the α -event is measured, the detector cell and the edges of the light guide leading to the photocathode has to be reflective. The light will then be directed towards the photocathode even if it was emitted in the opposite direction [18].

When exiting the scintillator solution, the emitted light enters a light guide leading to the photocathode. The photocathode is not equally sensitive across its surface, and the purpose of the light guide is to spread the emitted light over a larger area of the photocathode regardless of where in the scintillator cell the light is emitted from [18]. A longer light guide will spread the light more, but will lead to an amount of light-loss. The photocathode, as shown in Figure 5, produces electrons relative to the amount of light hitting it, and the electrons are accelerated to the first dynode. The electron that hits the dynode knocks free more electrons, which are accelerated to the next dynode. This continues to further dynodes, causing a cascade of electrons to which eventually hit the anode [19, 21].

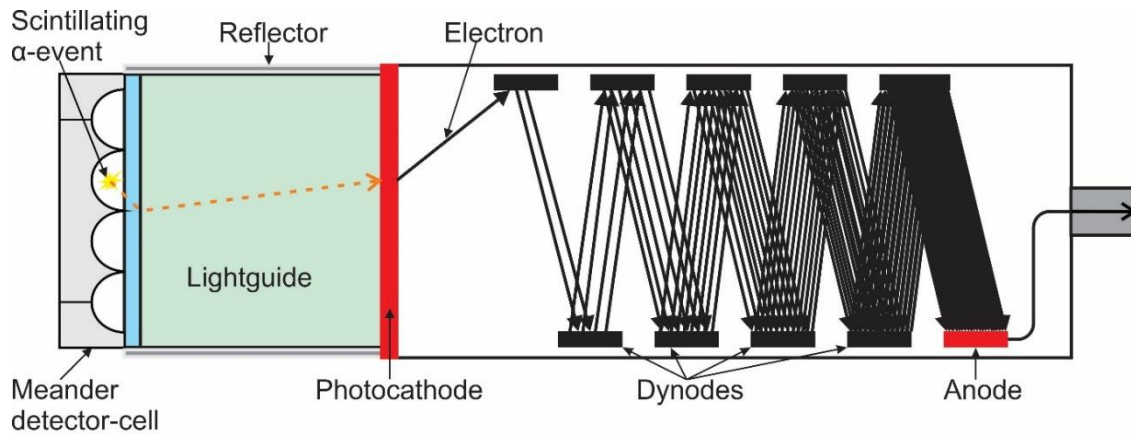


Figure 5 Schematic of a photomultiplier tube connected to a light guide and a meander detector cell.

More information about the electronics connected to the detector is described in Chapter 4.2.6 in this thesis.

2.2.2 γ -rays and interaction with matter

Photons ejected from the nucleus of a decaying atom is called a γ -ray. γ -rays often follow or accompanies α - or β - decay, or electron capture [17]. As γ -rays are neutral entities, they will not directly ionize or excite surrounding atoms as charged particles do. Even so, γ -rays will interact with matter, but in an indirect way. Such interactions occur when there is a collision between the γ -ray and the electron, i.e. when the wave function of the photon and electron overlap significantly. These kind of interactions are mainly the Photoelectric effect, Compton Effect and Pair formation. They are routinely described in textbooks, and will not be explained here [17, 21].

When detecting γ -rays, the detected number of counts is not the total amount of activity present. The count rate has to be corrected for I_γ which is the intensity of the gamma line compared to the amount of emitted radioactivity, and ε_γ which is the efficiency of the gamma detector. The total activity (R) is then calculated from the measured amounts of counts (A) shown in Equation 2 [9]:

$$R_\gamma = \varepsilon_\gamma * I_\gamma * A \quad (2)$$

2.2.3 Cyclotrons, linear accelerators and particle transport

The Cyclotron

A charged particle that moves through a magnetic field will be affected by a force (named the Lorentz force) [17] acting perpendicular to the movement direction. This means that if placed in a uniform magnetic field, a moving particle will travel in a circular orbit. Basic principle dictates that a charged particle will get accelerated if placed in an electromagnetic field. By combining these principles, E. Lawrence invented the cyclotron to accelerate charged particles to high kinetic energies. The idea was to place two hollow D-shaped electrodes back to back inside the uniform magnetic field of a large electromagnet. There is a gap between the two D-shaped electrodes that creates a drift region where a passing particle will be accelerated. The D-shaped electrodes has to be inside a vacuum chamber. If they are not, the particles will collide with gas-molecules, causing them to lose their energy by scattering. A schematic of the principle of the cyclotron is shown in Figure 6.

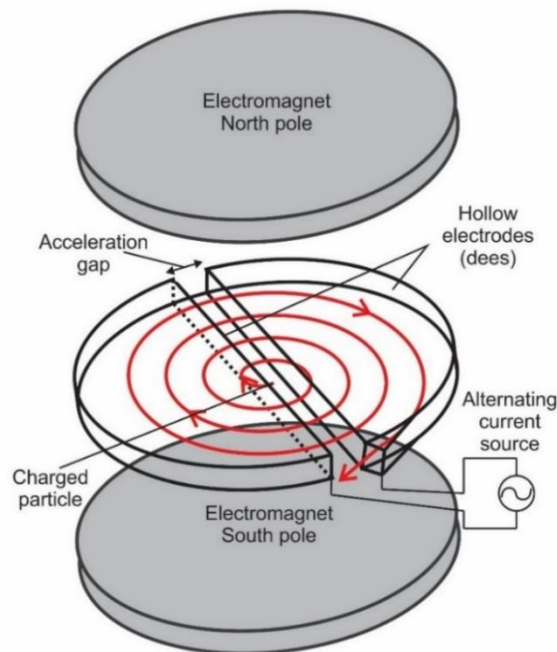


Figure 6: Schematic of the concept of a cyclotron.

The particle to be accelerated starts in the center of the circle and is accelerated across the gap and into a drift region. There, the particle will experience forces as described and move in a circular path. As the particle drifts, the polarity of the voltage is switched, and when the particle then returns to the accelerating gap, it is again accelerated across it to the other drift region. As the speed of the particle decides the radius of the circular path, when the speed increases the particle will move in a spiral-like pattern. When the particle is accelerated enough, it will reach the edge of the cyclotron and can be extracted [17]. Actual cyclotrons are built on these principles, but are more advanced. A more detailed description of how today's actual machines are outside the scope of this thesis, but is easily available in multiple textbooks and manufacturer's brochures.

The Linear Accelerator (LINAC)

A different type of particle accelerator than the cyclotron described above is the linear accelerator. In this type of machine, the particles are accelerated in a straight path instead of being forced to move in a circular path by the magnetic field. This makes it possible to accelerate ions that are too heavy to accelerate in a cyclotron [17]. In a linear accelerator (LINAC) the beam enters at an already significant velocity, usually supplied from a cyclotron [9, 17]. The accelerator consists of the main accelerator tube with vacuum and the hollow tubular electrodes inside it. Using an electric field, the hollow electrodes can be made to attract or repel the particles in the beam.

The particle is first attracted to the first electrode, and after passes through the electrode, or drift tube, the electric field is switched. The next electrode is then attracting the beam, while the previous one is repelling it. This causes the beam to be accelerated in the gaps between the electrodes, and to drift inside the drift tubes. To keep the acceleration uniform, the time spent inside the drift tubes along the accelerator has to be kept constant, so the drift tubes' length increases with the increase of the speed [17]. A schematic of a linear accelerator is shown in Figure 7.

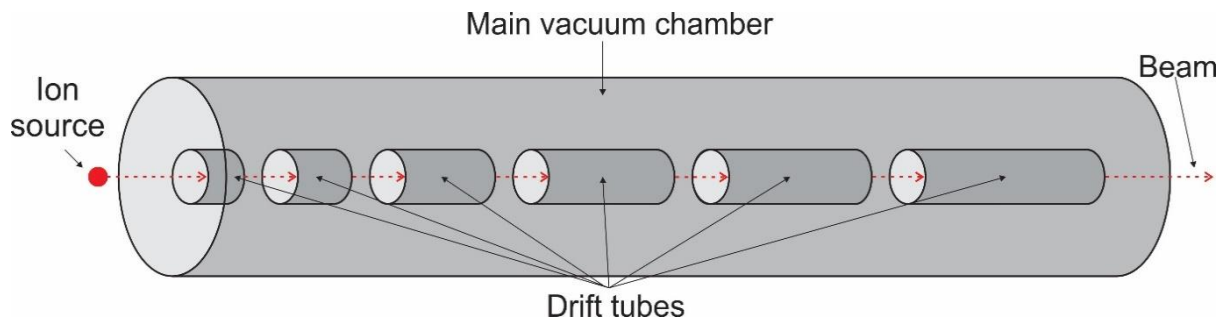


Figure 7: Schematic of a linear accelerator.

Particle beam transport

When accelerating particles, the goal is usually to induce specific nuclear reactions by shooting them inside nuclei of a certain type. The nuclei being shot at with the accelerated particles are called a target. For super-heavy element research, the target is usually a thin metal foil, to allow the recoiling atom to exit the foil. To perform experiments inside an accelerator directly is difficult, both due to high radiation and the limited space available inside the accelerator. Because of this, it is better to transport the accelerated beam to a shielded location with more space available than inside the accelerator [17].

When traveling at an angle to a uniform field created between two surfaces, charged particle beams will be deflected. To focus or defocus the beam, the particle beam can travel through

dipoles (two magnetic poles), quadrupoles (four magnetic poles) or fields created by more surfaces [17]. As mentioned in the section about cyclotrons, a moving charged particle will be affected by the Lorentz force when moving in a magnetic field, which causes the particle to curve. Because of this, a magnetic dipole can be used to control the direction of a particle beam by changing the magnetic field of the magnet, and thereby the magnetic rigidity of the particle [22]. A quadrupole focuses in a plane, and defocuses in the other. Using two quadrupoles where the magnetic fields are 90 degrees relative to each other will focus the beam in both planes. To transport accelerated beams over long distances, without losing a significant amount of beam, a combination of magnetic dipoles and quadrupoles are used.

Nuclear reactions, cross sections and reaction rates

A nuclear reaction is denoted as $X(a,b)Y$, where X is the target nuclei, a is the projectile, b is the emitted particle after the reaction and Y is the residual produced in the reaction [17, 23]. When the beam from a particle accelerator hits a target, the probability of the occurrence of a specific nuclear reaction is defined by the reaction cross section (σ) [24]. The cross section is given in the unit barn [17], which is equal to an area of 10^{-24} cm².

The target is a thin metal foil of a specific thickness. The thickness, x , of the part of the target where the reaction product manage to escape the foil, is called the active part of the target. Number of atoms, N , is the number of target nuclei. Target nuclei refers here only to the species of atoms that participate in the nuclear reaction [24].

If the beam has an intensity of I particles per second, which hits a target foil of thickness x containing N number of atoms/area, and the cross section is known, Equation 3 below can be used to calculating the rate of the nuclear reaction [9].

$$R = \sigma * I * N * x \quad (3)$$

By using Equation 3, a known reaction rate and cross section, the flux is calculated. This flux can be used to calculate the cross sections of other reactions with the same flux. In addition to depend on the intensity of the beam and the thickness of the target, the cross section also varies with the beam energy. By measuring the cross section for one reaction over a range of energies, it will give the reaction's so-called "excitation function". An example of an excitation function for the reaction $^{181}\text{Ta}({}^3\text{He},\text{xn})$ is shown in Figure 8. As seen on the figure, the more energy the projectile has, the more neutrons are ejected from the compound nucleus.

The compound nucleus is the intermediate specie formed when the beam particle and target nucleus combines. In a compound nucleus reaction, the energy of the projectile is distributed among all the nucleons of the compound nucleus. Unlike a direct nuclear reaction, where the recoil product has a lifetime of 10^{-22} s, the lifetime of a recoiled compound nucleus is in the order of 10^{-18} to 10^{-16} [17]. This is long enough to be identified as a definite specie. The compound nucleus "cools down" by ejecting particles and electromagnetic radiation (prompt γ -ray). The ejected particles are commonly neutrons, as shown in the excitation function for

^{181}Ta when bombarded with ^3He particles. Each neutron close to the potential surface is bound with about 8 MeV of energy. Because of this, for each extra 8 MeV of energy brought in by the projectile, an additional neutron is ejected. The internal fine structure of a given nucleus will change the excitation functions detailed shape [23]. Therefore, studies of the excitation functions can reveal details about the nuclear structure and nuclear bonding. In addition, the excitation function provides a way to calculate expected yields for given nuclear reactions. In this work the cross sections were measured with this in mind, as the cross sections is a way to calculate the expected production yield at the cyclotron in Řež. The measured cross sections were also used in the investigation of ^{266}Bh , where the maximum cross section would be used to give the highest yield of ^{266}Bh .

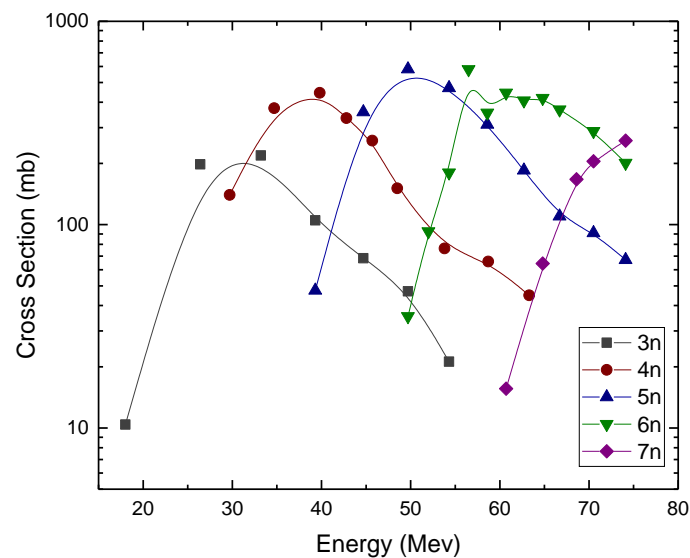


Figure 8: Excitation function for the $^{181}\text{Ta}(3\text{He}, xn)M$ reaction, where $M = ^{181}\text{Re}, ^{180}\text{Re}, ^{179}\text{Re}, ^{178}\text{Re},$ and ^{177}Re . The measured values are from the work of Hermes, F., et al.[25].

2.2.4 Target chamber, gas-jet transport, recoil transfer chamber and physical preseparator

The target chamber type generally used, when not using a preseparator, consists of an outer and inner target chamber. The outer target chamber is a part of the beam line, which transfer the high-energy ion beam to the experiment target site. Thus, it has to maintain the high-vacuum that is necessary for beam transport. For experiments like the ones described in this thesis, where transport from the radionuclide production site ("target chamber"), to a chemistry apparatus in a lab outside the cyclotron and beam-line vaults, are done with a gas-jet system as explained below, an inner chamber must be added. The inner chamber, which is pressurized, is constructed to allow the beam to enter and interact with a thin target foil. Due to the momentum imparted by the beam ions, nuclear reaction products will recoil out of the foil. The gas inside the inner target chamber will stop the ions.

For chemistry experiments which have apparatus that must be operated during an experiment, one need a transport mechanism for the reaction products to the lab, in which the chemistry

apparatus is located. This is performed by a technique where a gas seeded with aerosol particles is passed through the inner target chamber. Since ions adsorb on all available surfaces, they will adsorb on the aerosol particles. The aerosol particles are small and light enough to be carried with the gas through a tube into the laboratory. This method is very fast, typically it will take less than a second to transport aerosols through a 20 m tube with 1.5 – 2.0 mm inner diameter. Since the inner target chamber acts like a transfer chamber for the produced ions, it is common to refer to it as a Recoil Transfer Chamber (RTC) [9]. Different products from nuclear reactions will exit the target with different amounts of energy. The products are slowed by the helium gas, and have a certain range in the gas. If the range is longer than the depth of the RTC, some of the products will hit the back wall of the RTC and be lost. Some RTCs therefore have the possibility to vary its depth to accommodate for the range of the nuclei of interest.

By using this type of target chamber, there is no selection of which products from the nuclear reactions that are caught on the KCl aerosol. This can give high backgrounds of unwanted products in the measurements. A solution to this is to use a physical preseparator, e.g. GARIS as described later in Chapter 4.2.1, which is placed between the target and the RTC. The preseparator uses dipole and quadrupole magnets to bend off unwanted ions and selectively transport the wanted products to a recoil transfer chamber. This kind of physical preseparator has been used in experiments with super-heavy elements [26, 27], reducing the background from unwanted nuclei.

2.2.5 Gas-jet transport and chemistry apparatus

As mentioned in Chapter 2.2.4, transport of the products from the RTC to a chemical facility can be done by using a gas-jet transport system. The gas-jet systems seen in this work contains helium gas flowing through a KCl aerosol oven/generator. In this oven, KCl is heated, causing KCl aerosols to flow with the helium gas to the RTC. The helium gas containing the KCl aerosols are flushed through the RTC, where the nuclides produced in the nuclear reactions are adsorbed on the KCl aerosols. The gas-jet then provides a rapid transport of the products from the nuclear reactions to the chemistry apparatus.

The chemistry apparatus must then in the first stage dissolve the aerosols in a suitable liquid for the relevant aqueous phase chemical studies. The dissolving is challenging, since the volume of the gas is considerably larger than the volume of the aqueous phase. Typical volume ratios is several liters of gas to about one milliliter of liquid. To ensure that each aerosol particle, which might carry one or more of the product nuclei, will be contacted and dissolved in the aqueous phase under such conditions is not trivial. The SISAK system achieved high yields (> 80 %) by using efficient mechanical mixers followed by a centrifuge that separated the gas from the liquid [9]. This only worked because the aqueous flow was in the 0.5 to 2.0 mL/s range, which is 30 to 120 times higher liquid volumes than the 1 mL/min used by the equipment in this work. Instead of the centrifuges of the SISAK system, the new approach described in chapter 2.1 was developed to simplify the complicated SISAK setup.

2.2.6 Super-heavy element research

Super heavy elements, or transactinides, are the elements from number 104 rutherfordium [28] to the recently named element number 118 oganesson. The placing of the 104th to the 112th elements in the periodic table (Figure 9), under the 4d- and 5d-orbitals is based on the expectation that they will fill the 6d-orbitals similarly to how the 4d- and 5d- orbitals are filled. This places them in the group of transition metals. The elements which are in the same group in the periodic system, are referred to as each other's homologues [7].

Group→	1	2	3	4	5	6	7	8	9	10	11	12	13	14	15	16	17	18
↓Period																		
1	1 H																	2 He
2	3 Li	4 Be											5 B	6 C	7 N	8 O	9 F	10 Ne
3	11 Na	12 Mg											13 Al	14 Si	15 P	16 S	17 Cl	18 Ar
4	19 K	20 Ca	21 Sc	22 Ti	23 V	24 Cr	25 Mn	26 Fe	27 Co	28 Ni	29 Cu	30 Zn	31 Ga	32 Ge	33 As	34 Se	35 Br	36 Kr
5	37 Rb	38 Sr	39 Y	40 Zr	41 Nb	42 Mo	43 Tc	44 Ru	45 Rh	46 Pd	47 Ag	48 Cd	49 In	50 Sn	51 Sb	52 Te	53 I	54 Xe
6	55 Cs	56 Ba	57 La	* 72 Hf	73 Ta	74 W	75 Re	76 Os	77 Ir	78 Pt	79 Au	80 Hg	81 Tl	82 Pb	83 Bi	84 Po	85 At	86 Rn
7	87 Fr	88 Ra	89 Ac	* * 104 Rf	105 Db	106 Sg	107 Bh	108 Hs	109 Mt	110 Ds	111 Rg	112 Cn	113 Nh	114 Fl	115 Mc	116 Lv	117 Ts	118 Og
				* 58 Ce	59 Pr	60 Nd	61 Pm	62 Sm	63 Eu	64 Gd	65 Tb	66 Dy	67 Ho	68 Er	69 Tm	70 Yb	71 Lu	
				* 90 Th	91 Pa	92 U	93 Np	94 Pu	95 Am	96 Cm	97 Bk	98 Cf	99 Es	100 Fm	101 Md	102 No	103 Lr	

Figure 9: Periodic table of elements, bold line showing the super-heavy elements. Figure reprinted from source [6].

When making models to describe orbitals, it can be done without taking the relativistic part of the wave function into account. When the charge of the nucleus increases, the relativistic part of the wave function will get more and more prominent, causing deviations in the electronic structure of the orbitals [29, 30]. This means that calculations of the electronic configurations of the ground state might no longer accurately describe the actual configuration of the atoms electron structure [28, 31]. The increased charge of the nucleus causes the s- and p-orbitals to shrink, moving closer to the nucleus. This again, with the s-and p-orbitals shielding the nuclear charge, will expand the higher orbitals p, d and f. To predict the electron configurations and chemical properties of the transactinides, theoretical calculations are performed. Results from physical experiments are used to confirm or reject these calculations, and acts as input to guide subsequent calculations.

Super-heavy elements are made by irradiating a target with a heavy ion beam. A major challenge with making super-heavy elements is to find suitable projectiles and targets that have a high neutron to proton ratio. This is because the super-heavy elements, which have a high number of protons, need a higher ratio of neutrons to enhance its stability. This is the reason that the neutron rich ⁴⁸Ca isotope has been used as a projectile. ⁴⁸Ca is a double-magic nucleus,

and therefore the unusual high neutron to proton ratio is stabilized. When searching for elements which are beyond oganesson, ^{48}Ca is not suitable. This is because there is no available target which has the required number of protons ($Z=99$ for element 119 and $Z=100$ for element 120). Targets with $Z=99$ and 100 would be einsteinium and fermium, which are extremely difficult to produce in the amounts required to make a target for such super-heavy element experiments [17].

Since the production rates of the transactinides are low, from ~ 30 atoms / h for rutherfordium and dubnium to 1 atom / 3 days for copernicium [7, 28], experiments take place over the span of days to months. To prepare a chemical experiment that would work with the produced transactinide, they are first tested with the homologues, or pseudo-homologues, of the transactinide in question. The homologues are usually β - and γ -emitters, and most can be detected with a γ -detector with good resolution (e.g. a germanium detector).

Before performing a liquid-liquid extraction experiment on a specific transactinide element, the equipment and method is tested under conditions as close to a full scale super-heavy element experiment as possible. The minimum for these conditions implies that the radionuclides are transported to the chemical apparatus by a gas-jet transfer system, using the same aerosol carrier as in the planned super-heavy element experiment. To mimic the expected chemical behavior of the transactinide element, homologues are frequently used. Short-lived radionuclides, of a homologue if possible, would be used to determine the transport capabilities and yields. In addition, tests must also be performed to verify that the chemical system is compatible with the requirements of the heavy-ion target system's RTC. When using a preseparator between the target and the RTC, one must in particular ensure that there is no risk of breaking any foil that separates the high-vacuum zone of the accelerator, the mBar pressure zone of the physical preseparator, and the high-pressure (0.5-2 Bar) zone of the RTC. If such a foil breaks, it would risk that aggressive liquids are sucked into the preseparator and even into the accelerator, which could cause extensive damage.

Most super-heavy elements decay by α -emission, spontaneous fission and/or electron capture [32]. Lighter elements, like the relevant homologues of the super-heavy elements, will if produced on-line by an accelerator usually decay by β^+ and/or electron capture. Electron capture is non radiative, and detection of β^+ makes identification of nuclides difficult because of the continuous nature of β -decay. However, unlike detection of super-heavy elements, which are only produced in very low quantities, the relevant homologues can be made in large enough quantities to enable detection by γ -spectrometry. γ -spectrometry is highly nuclide specific due to the highly specific γ -ray energies emitted. This provides a major difference in the detection methods of super-heavy element- and homologue experiments, since the methods of detecting α -particles and γ -rays demands different equipment. This difference will affect the development of the chemistry apparatus, as the tests under similar conditions as super-heavy element experiments (β^+ -emitting homologues from an accelerator) would be performed in separate tests than the tests of a suitable α -detection system.

The half-lives of the super-heavy elements are in the region from μs to s. Because of the chemical reaction rates to achieve equilibrium, and too slow equipment, chemistry experiments only work with elements that have lifetimes over a few tenths of a second. To be able to detect the nuclides with a long enough lifetime, the systems for chemistry experiments has to be fast enough to transport the activity to the detector before it decays.

3 Experiments performed in Řež, at the Isochronous Cyclotron U-120M

3.1 Background

As explained in Chapter 2.2.4 about super-heavy element research, there is a need to develop and test experiments with the lighter homologues of the super-heavy elements. In the work presented in this part of the thesis, the commissioning of a facility to perform such homologue experiments are presented.

Radioactive isotopes of the homologues can be made with a relatively small accelerator that produces a beam with lower energy than what is used in a full-scale transactinide experiment (around 6 MeV/u [33]). Such machines usually only provide beam of light particles, not the heavy ions needed for experiments with super-heavy elements. Beam typical for such machines are ^1H , ^2H , ^3He and ^4He , since sources that produce hydrogen and helium ions are relatively simple and cheap. Since the homologues can be produced at these smaller facilities (compared to e.g. RIKEN), development of e.g. a new chemical separation system can with advantage be performed at such a facility, since obtaining beam time is much easier and cheaper.

For the super-heavy element research group in Oslo, production of and experiments with these homologues has previously been performed at the OCL (Oslo Cyclotron Laboratory) [7, 31, 34, 35]. However, the use of a ^3He beam at the OCL became too expensive to utilize within a sensible budget after the price increase of ^3He , which was due to “homeland security” needs in the US after the 9/11 terror attack. Because of this, part of the work in this thesis was to participate in building and commissioning a new experiment facility at the U-120M Cyclotron [36] at the Nuclear Physics Institute (NPI) [37] in Řež in the Czech Republic. The instrumentation and analysis methods used in this work is described in the next chapters. The work was done as a collaboration and joint project between UiO and Czech Technical University (CTU) in Prague.

3.2 Methods and instrumentation

3.2.1 The isochronous cyclotron U-120M

The cyclotron used in the Řež experiments was the isochronous cyclotron U-120M [36] (Figure 10) at the Nuclear Physics Institute, Department of Accelerators in Řež, Czech Republic. The cyclotron can accelerate light ions (H^+ , H^- , D^+ , D^- , ${}^3He^{2+}$ and ${}^4He^{2+}$) to moderate energies. For transport of the ions out of the accelerator, the cyclotron is equipped with an electrostatic-deflector extraction system. The voltage that can be applied to the deflector is usually the parameter that limits the maximum available beam energy from the machine. This is also the case for the ${}^3He^{2+}$ beam which was used in the experiments reported here, where the energy limit was 47 MeV. Minimum energy for the ${}^3He^{2+}$ beam from the machine is 18 MeV. It can be noted that after the experiments described here, the engineers in Řež managed to increase the maximum energy to 51,8 MeV [38].

The energy of the ion beam from the cyclotron used in this work was 47 MeV. Beam intensity was typically 200-350 nA (A rate of 300 nA corresponds to $9.36 \cdot 10^{11}$ incident particles per second).

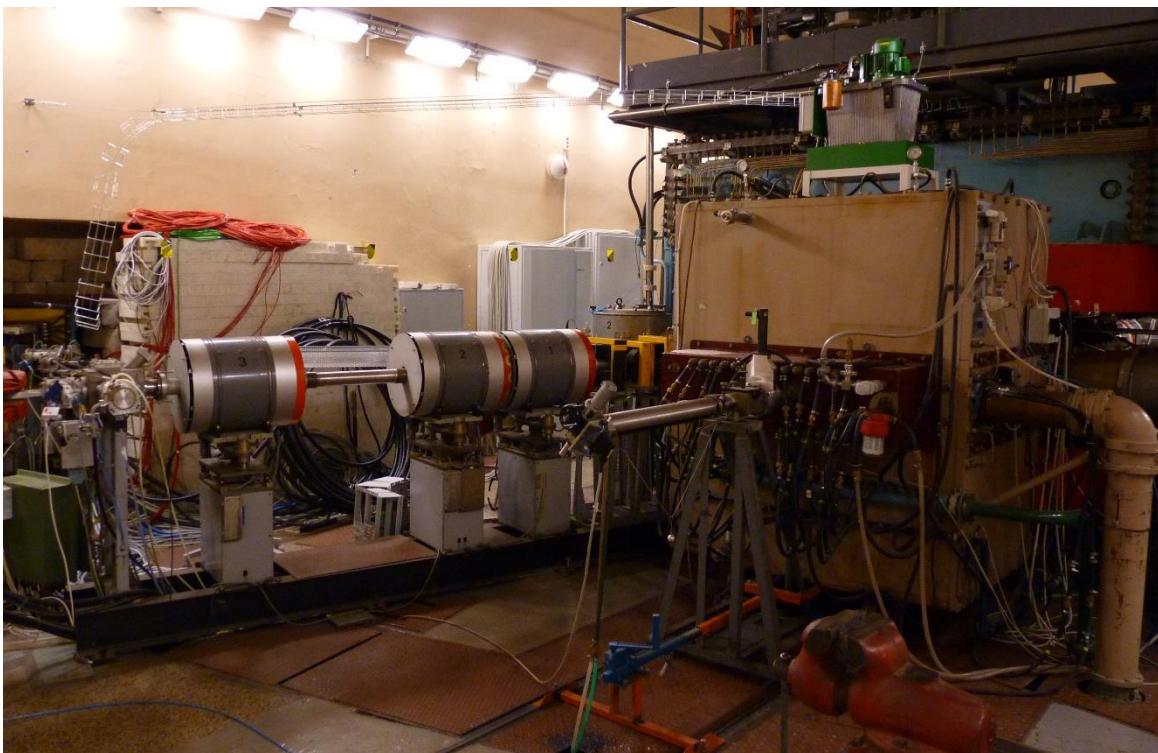


Figure 10: The Isochronous cyclotron U-120M at the Řež cyclotron facility.

3.2.2 Target chamber and gas-jet system

The setup used to transport nuclei from the target to the collection apparatus is as shown on Figure 11. The beam from the cyclotron enters through the 10 μm thick HAVAR-foil [39] window of the inner target chamber, going through 7 mm He-gas before hitting the 25 μm target foil. As explained in Chapter 2.2.3, when the beam hits the target, it will cause a compound nuclei reaction that produces the wanted radionuclide(s). From calculations with SRIM [40], which is a software package for calculating the range and stopping of ions in matter, the produced radio nuclei only have enough momentum to escape the last μm fraction of the target foil. The active part of the heaviest target used here, tantalum, was 0.06 μm , while the active part of the lightest target used here, zirconium, was 0.3 μm . This shows that the range of the nuclei is dependent on the momentum of the compound nucleus and on the target material. After going through the target, the beam travels 8 mm in He-gas before hitting another 10 μm HAVAR-foil, exiting the target chamber. The beam is stopped with a beam stop made of 20 mm thick carbon block. The carbon block is electrically insulated, and serves in addition as a faraday cup to measure the amount of beam that has passed through the target. A schematic of the target chamber is shown in Figure 11, and a picture of the target chamber is shown in Figure 55 in Appendix C.

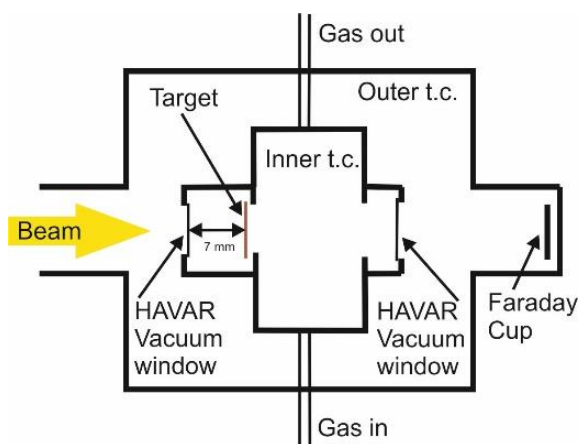


Figure 11: Simple schematic of the target chamber.

The targets used were 25 μm thick foils of natural zirconium (Zr), niobium (Nb), ytterbium (Yb), lutetium (Lu), hafnium (Hf) and tantalum (Ta). The thickness of the active part of the target, i.e. the downstream part which made ions that had enough momentum to escape the foil, is given in Table 2 on page 29. The foils were glued to a metal-holder with epoxy glue. To change between different targets, the target holder was removed from the target chamber and replaced with a different holder with a different target foil. Switching the targets had to be done manually, and care must therefore be taken to minimize radiation dose.

As shown on the schematic of the gas-jet system in Figure 12, the He-gas flows through the tube furnace with KCl salt heated to ~ 620 $^{\circ}\text{C}$, creating KCl aerosols in the He-gas. The flow of the He-gas was measured and controlled with a combined mass-flow meter/controller, which is digitally controlled from the computer. The He-gas flow was varied between 0.3 – 3.0 L/s. The aerosol-filled gas then went through the Cu-cooling coil outside the oven to lower the gas

temperature before it enters a ¼” outer diameter Swagelok Perfluoroaloxoy (PFA) tube (30 m) that is connected to the inner target chamber. In the Recoil Transfer Chamber (RTC), the products escaping the target will absorb on the surface of the KCl-aerosols and will be carried with the gas to the experiment station through a 30 m 1/8” outer diameter PFA capillary tube.

The gas was then transported to a valve, where the flow could be directed either to an experiment or to the bypass filter. With the valve in the experiment position, another valve decides if the gas would enter direct catch (DC) or a different experimental setup. In this experiment, the third section was also directed to bypass, but would in later experiments be used for an additional experiment to direct catch, but it was not used in this experiment. The gas was removed by vacuum pump.

The DC filter, Whatman Glass-Fiber/c 5.0 cm fiber-glass filters, was mounted in the filter holder for direct catch, and was removed and put in zip-lock bags for counting on a High-purity Germanium-detector (HPGe). For measurements using an aluminum catcher foil, the aluminum foil was attached to the back of the target holder with two strips of tape, as shown on Figure 13.

Rez Gas-jet setup for Direct Catch

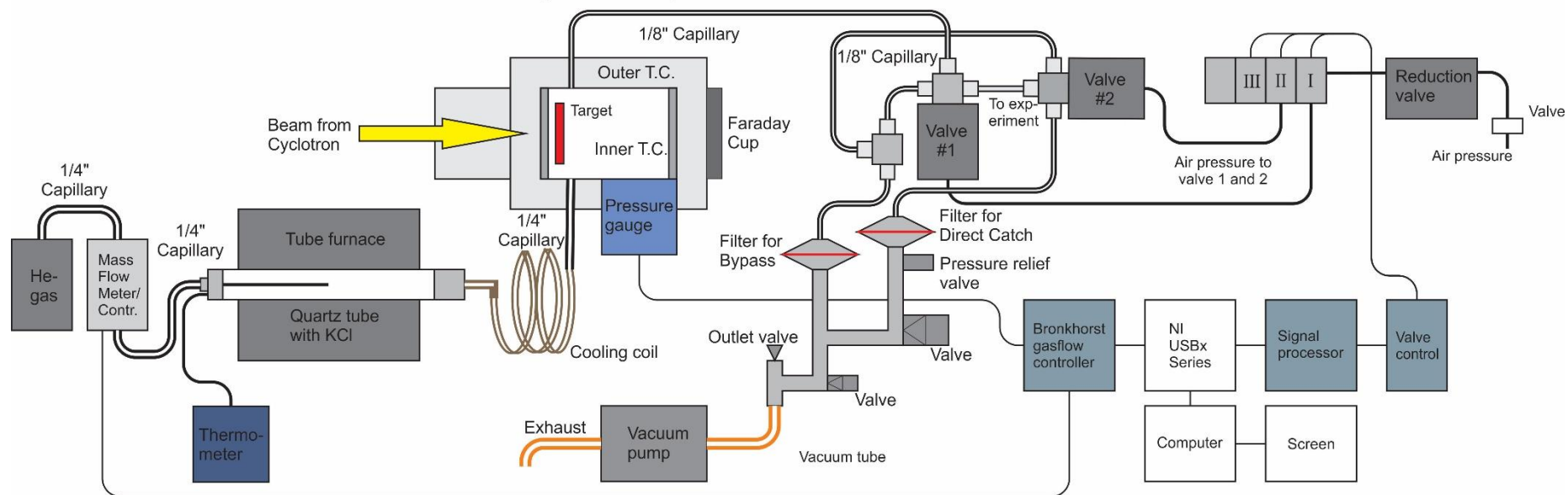


Figure 12: Schematic of the total setup of the gas-jet system commissioned in the Řež experiments.

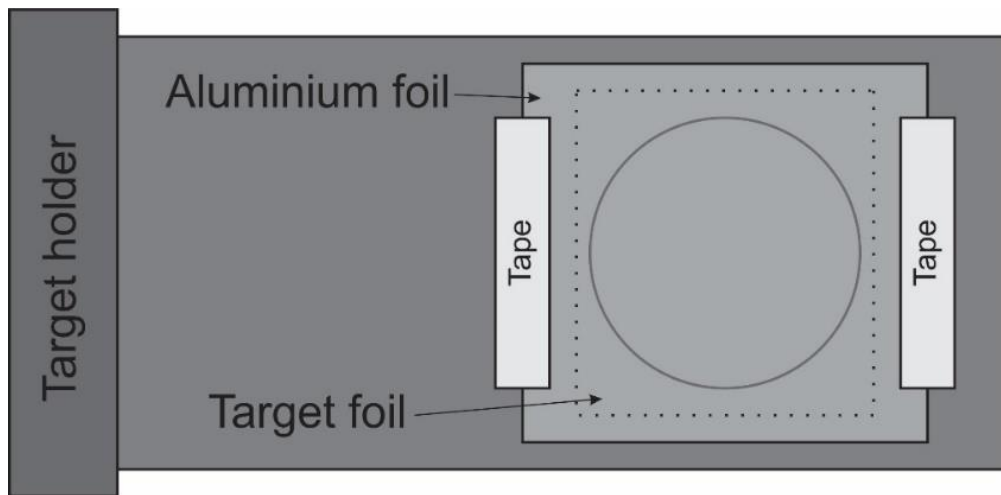


Figure 13: Target holder with aluminum foil mounted on the back with strips of tape.

3.2.3 Germanium detector

The detector used in the Řež experiments was an ORTEC GMX45-Plus HPGe detector connected with a DSPEC jr 2.0 integrated gamma spectrometer from ORTEC. Energy and efficiency calibration of the spectrometer were done with a set of standard sources (^{241}Am , ^{152}Eu , ^{137}Cs , ^{133}Ba and ^{60}Co) provided by the Czech Institute of Metrology.

All samples were detected at 15 cm distance from the detector, which was the shortest distance the detector was efficiency-calibrated for. The acquisition program used was Maestro [41] from ORTEC.

3.3 Analysis methods

3.3.1 Production of homologues

When analyzing the γ -spectra, only peaks with more than 200 net-counts, in the low-energy region below 511 keV, or significantly higher net-count than the background was marked as a region of interest (ROI). Multiplets were observed for some of the γ -lines, and was not used. This did not constitute a problem, as all nuclei of interest had at least two or more γ -lines that were not overlapped by neighboring lines in the measured spectra.

Using customized versions of Maestro's library files containing the nuclei and their strongest γ -rays of interest for each specific target, the peaks were identified and saved to a report-file. The report-files was used in further calculations of yield and cross sections. The calculations are shown in Appendix C, and the final results are presented in chapter 3.4.

An example of an analyzed spectrum from irradiation of lutetium is shown in Figure 14, and a larger version of the spectrum is shown in Appendix C.

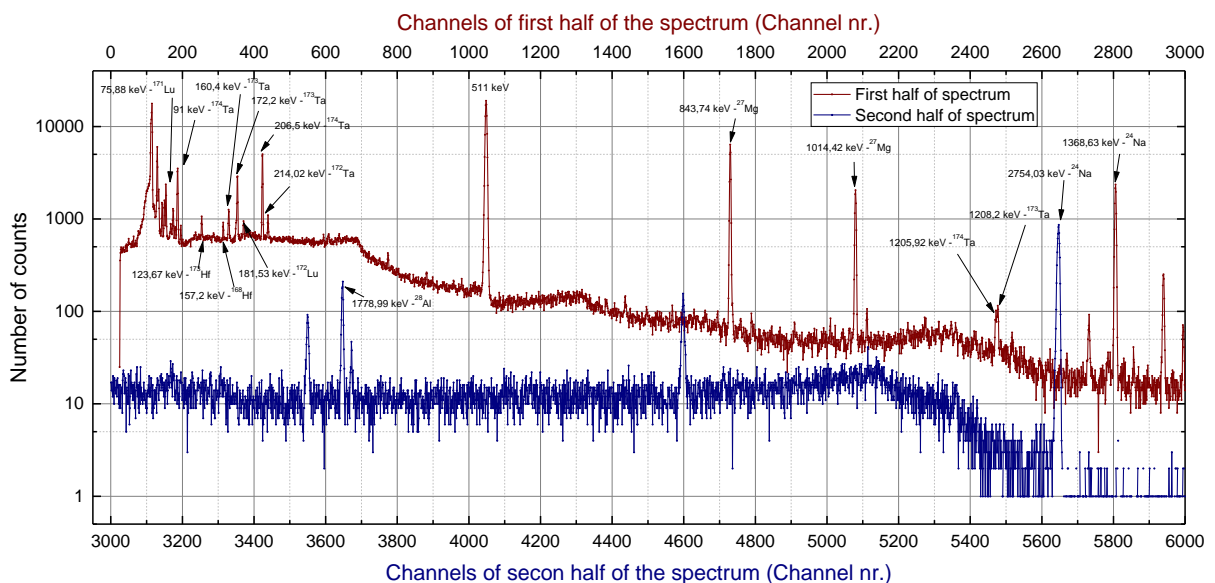


Figure 14: Example of a semi-logarithmic plot of an analyzed HPGe-spectrum. Target irradiated was natural lutetium. First half of the spectra is the red graph in the upper part and the second half of the spectra is the blue graph in the lower part.

3.3.2 Beam energy loss and cross sections

Energy loss calculations were done to know the real energy of the beam when it hit the active part of the target. The calculations of the energy loss of the $^3\text{He}^{2+}$ -beam and the range of the compound nuclei was done using SRIM [40] and fitting in Origin [42].

The energy of the recoiling compound nucleus was calculated for each target by using SRIM and the energy of the beam at the last few micrometers of the target. SRIM was then used to calculate the range of the compound nucleus where it would still exit the target. This range defines the active part of the target, i.e. the part where the nuclei can be transported to the experiment station are produced and able to escape the foil. In Figure 15, compound nuclei produced in the target is shown in three examples, where one compound nucleus does not exit the target, one has just enough energy to exit the target and the last exits the target with energy remaining.

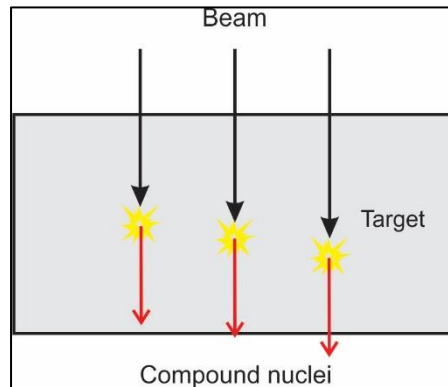


Figure 15: Schematic drawing showing compound nuclei made from a beam hitting a target. The reaction to the left happens too far into the target, and the energy of the compound nucleus is not enough to eject it from the target. The two other reactions happens far enough into the target so that the compound nucleus escapes. The reaction in the middle shows a reaction where the compound nucleus has just enough energy to exit the target.

Table 2 shows the calculated beam energy loss through the different targets, the energy of the ejected compound nuclei and the thickness of the active part of the target. Before going through the target, the beam loses 0.60 MeV when going through the HAVAR foil and 0.04 MeV when going through the helium gas between the HAVAR foil and the target.

Table 2: Table showing the loss of energy of the beam through the target, the energy of the ejected compound nucleus and the thickness of the active part of the target.

25 μm target	Beam energy loss through target, MeV	Energy of ejected compound nucleus, MeV	Thickness of active part of target, μm
Zirconium	1.14	1.44	0.43
Niobium	1.54	1.40	0.29
Ytterbium	1.37	0.77	0.15
Lutetium	1.43	0.76	0.11
Hafnium	1.91	0.73	0.08
Tantalum	2.38	0.72	0.06

The cross sections for the reactions $^{93}\text{Nb}({}^3\text{He}^{2+}, \text{xn})^{92-95}\text{Tc}$ are known, investigated by Bissem, H.H., et al. [43] and Kondratyev, S.N., et al. [44]. The excitation function from the data from both these works is shown in Figure 16. By using the cross sections from these investigations, the amount of incident particles in this work was calculated. This was done by performing the same type of irradiation on a niobium target. Using the calculated amount of incident particles,

the cross sections of the products from the five other target foils could be calculated as shown in Appendix C.

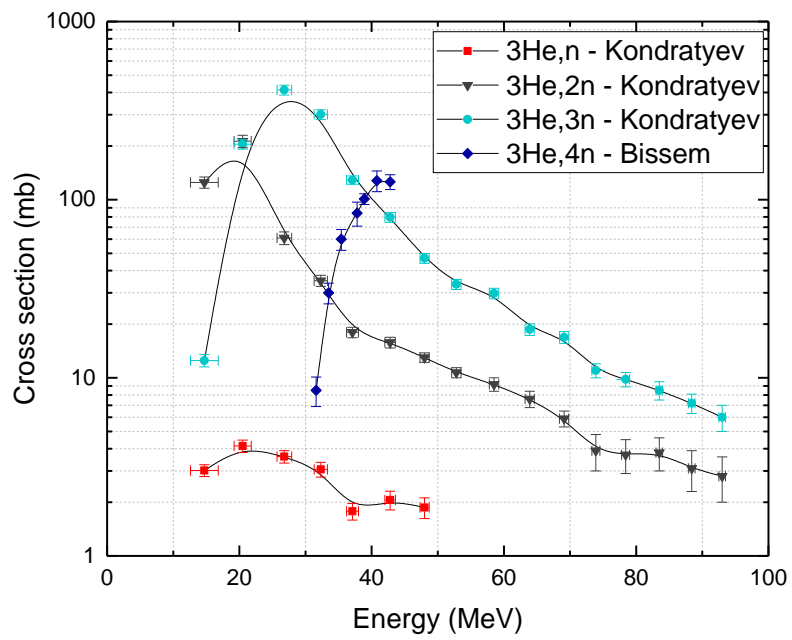


Figure 16: Plot of the measured excitation function for the $^{93}\text{Nb}(^3\text{He}^{2+}, xn)^{92-95}\text{Tc}$ reactions., with data from the works of Bissem, H.H., et al.[43] and Kondratyev, S.N., et al. [44].

3.4 Results and discussion

3.4.1 Produced nuclei from the cyclotron

The amount of activity of each nuclei produced from the cyclotron are presented in Table 3 and 4. Table 3 shows the activity obtained when measuring with aluminum catcher foil taped to the back of the target holder, while Table 4 shows the activity when measuring with the direct-catch system. For the measurements with aluminum catcher foil, the target was irradiated for 600 seconds, had a cooldown of 20 or 30 minutes and was measured for 10 minutes. For measurement with the direct catch the target was irradiated for 10 minutes, had a cooldown of 100 s, 180 s or 200 s and was measured for 200 s or 300 s.

Each nuclei is listed in Table 3 with one or more neutron reaction (n-reaction). This is due to the fact that natural targets were used instead of isotope enriched targets, and for some of the nuclei it is not certain which neutron reaction was dominant. The neutron reactions given in these tables are the reactions that are most likely to have occurred with the available beam, compared to the threshold energy.

Table 3: Activity with uncertainties (unc.) of produced nuclei measured with aluminum catching foil.

<i>Target</i>	Nuclei	T_{1/2} [32]	Type of n-reaction	Activity per beam integral, cps/BI	Activity, cps
<i>Zirconium</i>	^{93m} Mo	6.9h	2,4	1.91 ± 0.06	604 ± 19
	⁹⁰ Mo	5.7 h	3,4,5	6.8 ± 0.4	2169 ± 115
	⁸⁸ Mo	8.2 m	5	9.4 ± 1.3	2986 ± 411
<i>Niobium</i>	⁹⁴ Tc	4.9 h	2	1.01 ± 0.04	318 ± 65
	⁹³ Tc	2.7 h	3	8.9 ± 0.7	2805 ± 226
	⁹² Tc	4.4 m	4	390 ± 12	121503 ± 3746
<i>Ytterbium</i>	¹⁷³ Hf	23.6 h	2,3,4,6	1.53 ± 0.07	643 ± 23
	¹⁷⁰ Hf	16.0 h	4,5,6	3.0 ± 0.2	944 ± 66
	¹⁶⁹ Hf	32.5 m	5	166 ± 20	54433 ± 6497
<i>Lutetium</i>	¹⁷⁴ Ta	1.04 h	4	39.0 ± 0.3	10605 ± 70
	¹⁷³ Ta	3.14 h	5	23.9 ± 0.3	6511 ± 245
	¹⁷² Ta	37 m	6	1.05 ± 0.07	285 ± 18
<i>Hafnium</i>	¹⁷⁷ W	2.25 h	3,4,5,6	27.5 ± 0.4	6787 ± 92
	¹⁷⁵ W	35.2 m	4,5,6	52.8 ± 1.0	13023 ± 243
	¹⁷⁴ W	31 m	5,6	23.4 ± 1.7	5764 ± 418
<i>Tantalum</i>	¹⁷⁹ Re	19.7 m	5	230.2 ± 1.4	75730 ± 446
	¹⁷⁸ Re	13.2 m	6	21.3 ± 1.1	7024 ± 346

Table 3 also shows that some of the nuclei of interest were produced to a larger degree than the rest, in the magnitude of ten to a hundred times higher activity than the other isotopes of the same elements. The nuclei in Table 3 that are made at a relatively high quantity, specifically ^{92}Tc , ^{169}Hf and ^{179}Re , has half-lives between 4.4 and 32.5 minutes. The other nuclei, which is produced at a lower quantity, has half-lives ranging between 13.2 minutes to 23.6 hours. In Table 4, the same trend can be seen, where the most activity comes from the nuclei with half-life ranging from 6.4 minutes to 2.25 hours.

The half-lives of the nuclei to be used in future experiments will decide the amounts of counts available in each measurement. Since the nuclei with short half-lives grows in faster, there will be more counts and better statistics, but the time of the experiment will be shorter. Longer half-lives will give the possibility to measure for longer times, but fewer replicates will be possible to perform during the same amount of time.

From the results obtained in the experiments reported on here, one can deduce that for future experiments, it would be practical to perform multiple replicates and to get higher statistics. Therefore, the nuclei with half-lives around 6 to 30 minutes half-lives would be the best alternative to use in future experiments.

Table 4: Activity with uncertainties (unc.) of produced nuclei measured with gas-jet system and direct catch.

Target	Nuclei	T_{1/2} [32]	Type of n-reaction	Activity per beam integral, cps/BI	Activity, cps
<i>Zirconium</i>	$^{93\text{m}}\text{Mo}$	6.9h	2,4	0.97 ± 0.04	306 ± 73
	^{90}Mo	5.7 h	3,4,5	2.10 ± 0.09	662 ± 29
<i>Ytterbium</i>	^{173}Hf	23.6 h	2,3,4,6	0.51 ± 0.03	175 ± 55
	^{170}Hf	16.0 h	4,5,6	0.94 ± 0.14	314 ± 138
	^{169}Hf	32.5 m	5	55.3 ± 1.5	18772 ± 501
	^{168}Hf	25.95 m	6	0.53 ± 0.03	182 ± 10
<i>Hafnium</i>	$^{179\text{m}}\text{W}$	6.4 m	2,3,4	36 ± 2	13916 ± 959
	^{177}W	2.25 h	3,4,5,6	21.6 ± 0.2	7783 ± 52
	^{175}W	35.2 m	4,5,6	28.5 ± 0.3	10225 ± 122
	^{174}W	31 m	5,6	29.5 ± 0.5	10364 ± 194
	^{172}W	6.7 m	5	37.8 ± 0.9	14308 ± 342

3.4.2 Gas-jet transport yields

When comparing the activities measured for the same nuclei with both aluminum catcher foil and a gas-jet system with direct catch, the transport yields of the direct catch method can be calculated. The calculated transport yields of each nuclei detected with both methods is shown in Table 4 below. These yields shows a variation of 47.8% between the highest and lowest yields when comparing the different elements. This variance could be because of chemical

effects/affinities. However, it is more likely that the conditions of the system varies during the week the experiments lasted. This is a well-known fact from previous operation of the same target chamber in Oslo [7] and is believed to be caused by the relative low gas flow. I.e. a substantial but varying amount of aerosols are lost due to absorption on walls etc. It is known that the yield increases to over 90 % when the gas-flow is increased to 5 L/min. However, such a high gas-flow cannot always be handled by the chemical apparatus.

The yields also varies quite a bit between different isotopes of the same element, with the greatest variance being between tungsten isotopes (24.5 % difference) and the lowest variance being between hafnium isotopes (2 % difference). The variance between the isotopes could be caused by the nuclei being retained on the gas-jet capillary at low helium gas-flow (1.2 L/min). The difference in half-lives would then affect the yield, since the nuclei are being retained on the gas-jet capillary, and the isotopes with shorter half-lives would give a lower yield than the isotopes with longer half-lives [9]. As seen in Table 5, this assumption would only be a correct for the tungsten isotopes. Comparing the yields from the experiments performed with lower helium gas-flow-rates in this part of the thesis, with the experiments performed with a higher helium gas-flow-rates in Chapter 4 of this work (Table 7), the yields are higher when the helium flow-rates are higher.

Table 5: List of the yields from transporting the produced nuclei with the gas-jet system.

Target	Nuclei	T_{1/2} [32]	Yield, %
<i>Zirconium</i>	^{93m} Mo	6.9h	51 ± 2
	⁹⁰ Mo	5.7 h	30 ± 2
<i>Ytterbium</i>	¹⁷³ Hf	23.6 h	33 ± 2
	¹⁷⁰ Hf	16.0 h	31 ± 5
	¹⁶⁹ Hf	32.5 m	33 ± 4
<i>Hafnium</i>	¹⁷⁷ W	2.25 h	78.5 ± 1.2
	¹⁷⁵ W	35.2 m	54.0 ± 1.2

Only half of the targets used for measurements with aluminum catcher foil were measured with the gas-jet system. This was due to the limited time on the cyclotron in Řež. Further experiments would have given more info on the transport yield of the niobium, lutetium and tantalum nuclei.

Both the relatively high amount of produced activity of most of the wanted nuclei, and the gas-jet transport system yields, shows that using the facility that was commissioned in this experiment would be applicable to use in later experiments. These later experiments would be to develop and test chemical systems with homologues of the superheavy elements.

3.4.3 Cross sections

The cross sections calculated for the nuclei listed in Table 3, are presented in Table 6. Here, same as with the produced activity, one or more n-reactions are listed due to the use of natural metal targets. The cross section for those listed with more than one n-reaction is therefore the combined cross section for the different reactions which could give the specific nuclei with a natural metal target.

Table 6: Cross sections of the produced nuclei measured with aluminum catching foil.

<i>Target</i>	<i>Product</i>	<i>Type of n-reaction</i>	<i>Cross section, mb</i>
<i>Zirconium</i>	^{93m} Mo	2,4	65 ± 2
	⁹⁰ Mo	3,4,5	81 ± 4
	⁸⁸ Mo	5	5.9 ± 0.8
<i>Ytterbium</i>	¹⁷³ Hf	2,3,4,6	416 ± 14
	¹⁷⁰ Hf	4,5,6	660 ± 46
	¹⁶⁹ Hf	5	1133 ± 135
<i>Lutetium</i>	¹⁷⁴ Ta	4	370 ± 2
	¹⁷³ Ta	5	606 ± 22
	¹⁷² Ta	6	5.5 ± 0.3
<i>Hafnium</i>	¹⁷⁷ W	3,4,5,6	427 ± 5
	¹⁷⁵ W	4,5,6	430 ± 8
	¹⁷⁴ W	5,6	386 ± 28
<i>Tantalum</i>	¹⁷⁹ Re	5	779 ± 4
	¹⁷⁸ Re	6	53 ± 2

3.4.4 Errors/uncertainty

During 10 minutes of irradiation, the beam would fluctuate, causing different amounts of compound nuclei to be produced at a given time during irradiation. The mean of the beam integral was measured, giving the approximate beam intensity during each irradiation.

The logged files of the beam intensity showed that the background levels of the intensity was not zero, and had to be corrected before the mean beam integral was used. The mean of the background level was calculated and added to the beam integrals. Using the mean beam integrals instead of the more precise method gives a larger uncertainty in the corrected activity values.

For an optimal measurement of the transport yield, the yield should have been measured multiple times a day, every day of the experiments, to notice if any large variations in the yield would occur. The yields presented in Table 5 is therefore an approximation for the transport yield for the specific nuclei at the time the transport measurement was performed. To improve

the yield of the gas-jet transport system, the capillary could be washed between changes of target to remove built up KCl and decrease retention of the nuclei. This is a time-consuming task, and would not be practical or economic to carry out during a beam-time [9].

The target foils used in the experiments in Řež were 25 μm thick, where only the last 0.05-0.43 μm of the target actually was releasing its recoil products into the gas-jet. This caused the first part of the target to slightly lower the energy of the beam more than a thinner target would.

4 Tests of the new liquid-liquid membrane phase separator system connected to the physical preseparator GARIS and on-line SISAK liquid scintillation system.

4.1 Background

Previous full-scale on-line liquid-liquid extraction experiments, with rutherfordium [7], has successfully been performed with the SISAK system and liquid scintillation detectors. As previously mentioned in Chapter 2.1, the operation and service of the custom built SISAK centrifuges is not trivial. As the new liquid-liquid extraction system, using membranes as separators instead of centrifuges, developed by Y. Komori [16] is easier to use, the goal was to test the system in an on-line homologue experiment with rhenium. The membrane separators are less complex than the centrifuges, since they are easier to take apart and change the membrane, compared to taking apart and cleaning the centrifuges which is both complex and time consuming. The use of the membrane separators instead of centrifuges for degassing and phase separation makes the operation of such an on-line liquid-liquid extraction and detection system much less intense and demanding.

This new liquid-liquid extraction system with membrane separators does not have a suitable detection system available. A possibility is to use the SISAK on-line alpha liquid scintillation detection system. However, due to different flow ranges in the two systems (0.5-1 mL/s for SISAK and ~ 1 mL/min for the FSE system), and questions in regards to the backpressure of the detection system (if the membrane separator system will be able to produce enough output pressure to overcome the detector backpressure) it is not obvious that the combination of these two systems will work. Investigations were therefore performed, under realistic conditions, to establish if the two systems could be combined.

Since the liquid scintillation detectors used with SISAK is known have successfully detected super-heavy elements in chemistry experiments [7], to successfully connect the membrane system together with the LSC detectors could mean that the equipment would be possible to use in a super-heavy element experiment.

The work presented in this chapter was performed as a guest at the RIKEN Nishina Center for Accelerator-Based Science in Japan, which is a research center for nuclear physics. Among other accomplishments at the RIKEN Nishina Center, it is the place of the discovery of the super-heavy element 113 nihonium. The research group worked with here was led by H. Haba, with Y. Komori in charge of the rhenium experiments. The combination of the liquid scintillation detection and membrane system was a joined work together with Y. Komori.

4.2 Methods and instrumentation

4.2.1 RIKEN Heavy Ion LINAC (RILAC) and GARIS

The accelerator used in the RIKEN (Rikagaku Kenkyusho - meaning Institute of Physical and Chemical Research) experiments was the Riken Heavy Ion LINAC (RILAC) [33] at RIKEN Nishina Center for Accelerator-Based Science in Japan. The RILAC produces heavy ion beams with a maximum energy of 6 MeV/nucleon. This is enough for most experiments with super-heavy elements. The Figure 17 shows a schematic of the overview of the RILAC facility [45]. The RILAC is supplied with ions from an Electron Cyclotron Resonance (ECR) ion source with a variable-frequency radio frequency quadrupole (RFQ) LINAC.

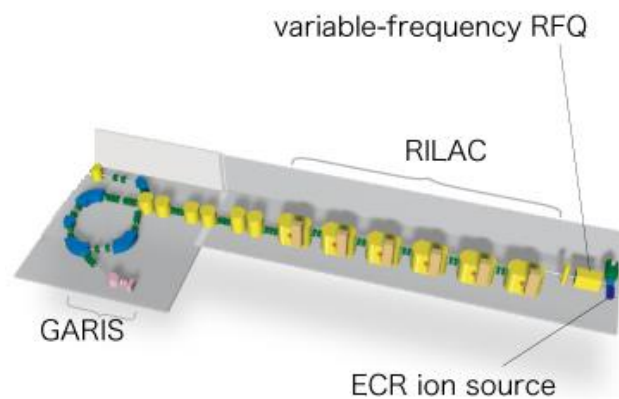


Figure 17: Overview of the RILAC and connected GARIS at the RIKEN Nishina Center for Accelerator-Based Science. The ECR ion source supplies ions that are entered into the RILAC from a variable-frequency RFQ. Figure reprinted from source [46].

The RILAC is, as shown on Figure 17, connected to the RIKEN Gas-filled Recoil Ion Separator (GARIS) [47]. GARIS (Figure 18) has four magnets in a Dipole1 – Quadrupole 1 - Quadrupole 2 - Dipole 2 (D1-Q1-Q2-D2) configuration. The D1 magnet separates the primary beam from the fusion product and D2 reduces background. This makes sure that nearly only the evaporation residues (EVR), which are the products of the nuclear reactions, gets transported to GARIS' focal plane. For physics experiments a large and complex particle detector will be mounted in the focal plane. For chemistry experiment the focal plane detector is replaced with the Recoil Transfer Chamber (RTC), where the EVRs are stopped in the gas-jet and adsorbs to the aerosol particles that are carried with the gas-jet to the chemistry apparatus. The helium-gas (0.1-1.0 Torr) part of GARIS is separated from the vacuum region from the accelerator with a differential pumping system. The beam intensity and the condition of the target were monitored with a PIN photo diode by detecting the elastically scattered particles (Rutherford scattering). This gives a direct measurement of the amount of target material that interacts with the beam, which is a good measure for the number of nuclear reactions that has taken place. If the target is partially broken, it will also be detected by the measurement of the Rutherford scattering, since the rate of the elastically scattered particles will drop if part of the target is lost.

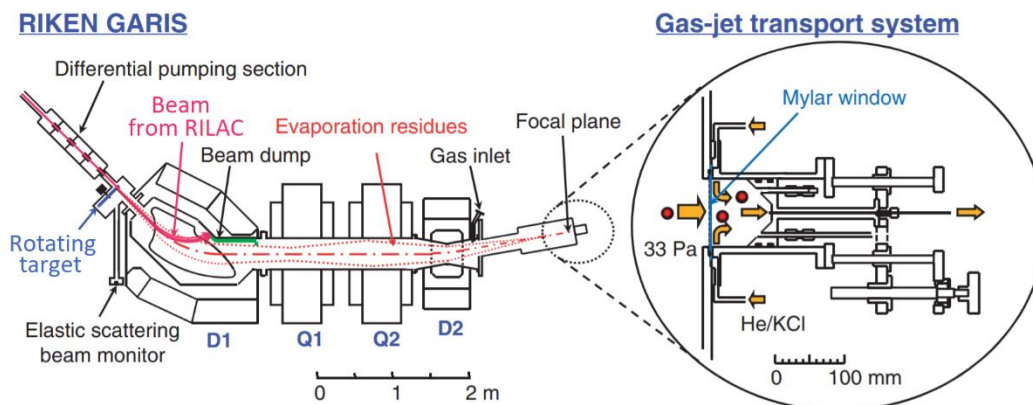


Figure 18: Schematic of GARIS and the connected gas-jet transport system. Figure reprinted from source [48].

4.2.2 Gas-jet system

Transport from GARIS to the experiment station, set up in a nearby laboratory, was performed with a gas-jet system. The Teflon capillary from GARIS to the lab was 10 m long and had an inner diameter of 2.0 mm. Helium gas was sent through a KCl aerosol generator before entering the recoil transfer chamber from six entrances around the front of the chamber. The gas inlets into the RTC is shown on Figure 18 and Figure 77 in Appendix D. The KCl aerosols catches the evaporation residues in the recoil transfer chamber. The gas outlet is at the back of the chamber.

4.2.3 Membrane liquid-liquid extraction system

As described in chapter 2.2.5, the gas-jet provides rapid transport to the chemistry apparatus. The aerosols were mixed with the aqueous phase in a t-connector before entering the Membrane Degasser [16] (MDG) shown in Figure 19. The gas/liquid mixture that entered the MDG passes into a separation chamber, where the gas escapes through a membrane on a mechanical support made of polyethylene, while the liquid passes the membrane and exits the chamber. By adjusting the suction under the membrane, a balance is reached in the separation chamber, causing the gas to be removed from the mixture before the liquid exits. The membrane used was Millipore Fluoropore No. FGLP04700 with pore size 0.2 μm . In the mechanical support for the membrane, there are small holes to let the gas through to the gas outlet. All capillaries connecting inputs and outputs of the MDG had an inner diameter of 0.50 mm. A vacuum pump was used to suck the gas through the filter. If too hard suction is applied, liquid will be forced through the membrane. For this reason, a liquid trap is installed to protect the vacuum pump and to easily discover if liquid exits the wrong way.

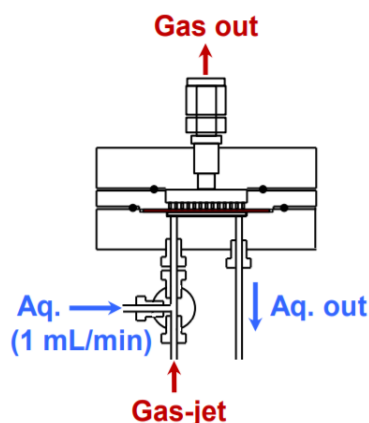


Figure 19: Cut through schematic of the Membrane Degasser. Figure reprinted from source [16].

The aqueous phase from the MDG was mixed with the organic phase in another t-connector, before entering the Teflon extraction capillary/Flow Solvent Extractor (FSE). In the FSE, the two phases were contacted and liquid-liquid extraction took place. Two lengths of Teflon capillaries were used, 50 and 100 mm long, and both had an inner diameter of 0.50 mm. From the FSE, the mixed liquid phases went through the Membrane Phase Separator (MPS) shown in Figure 20, where a PTFE membrane filter separated the two phases. The filter was ADVANTEC No. T300A013A with pore size 3.0 μm .

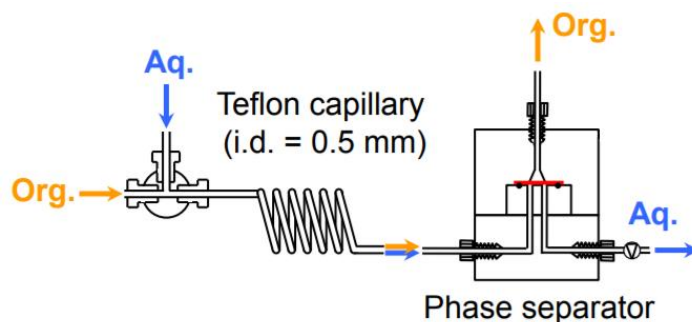


Figure 20: Cut through schematic of the Membrane Phase Separator and the connected Teflon capillary. Figure reprinted from source [16].

4.2.4 Germanium detector

The detector used in the Řež experiments was an ORTEC GEM 25185-P HPGe detector. Efficiency calibration of the spectrometer had been performed with a set of standard sources [1] (^{241}Am , ^{109}Cd , ^{57}Co , ^{139}Ce , ^{113}Sn , ^{88}Y , ^{137}Cs , and ^{60}Co). Transport time measurements was measured directly on top of the HPGe-detector, while all other measurements with the HPGe-detector were performed at 5 cm distance.

4.2.5 Rhenium experiment

Production of rhenium isotopes

To produce the rhenium isotopes, a 140.6 MeV $^{23}\text{Na}^{7+}$ ion beam with 0.75-2.0 μA per particle beam intensity was used. The target was $339 \pm 5 \mu\text{g}/\text{cm}^2$ isotope enriched $^{152}\text{Gd}_2\text{O}_3$ electrodeposited on eight $1.24 \text{ mg}/\text{cm}^2$ Ti backing foils. Picture of the rotating target is shown in Figure 76 in appendix. Thickness of the Mylar window at the focal plane of GARIS was 3.5 μm . The foil was supplied by Goodfellow.

Depth of the recoil transfer chamber was varied between 2 cm to 5 cm, which was done to investigate at what depth the most activity was detected. If the chamber is too shallow, the ERs will hit the back wall of the gas-jet chamber instead of being transferred to the KCl aerosols. The temperature of the KCl aerosol generator was set to 620 °C. The collection of the aerosols were performed on glass-fiber filter in a direct catch setup, with a vacuum pump used to remove the gas. The direct catch had an option for bypass, with another glass-fiber filter in a similar setup. The filters used in the DC was Glass fiber filters (ADVANTEC GB100R).

Helium flow-rate was selected to 5 L/min, which is known to provide very high and stable gas-jet transport yields [4]. The improved stability compared to what was e.g. typically observed with the old setup at the Oslo Cyclotron Laboratory (1.2-1.5 L/min He-flow) is believed to be due to avoiding that particles adhere to walls and surfaces because of the flush-out effect achieved at the higher gas flow (5 L/min).

To obtain the maximum yield from the preseparator, the right magnet setting that matches the magnetic rigidity of the nuclides of interest has to be found. Assuming the gas-jet yield would be stable at the high gas-flow, the magnet field of GARIS was adjusted, and the amount of rhenium isotope of interest was measured by collecting the aerosols on a glass-fiber filter. The setting that yielded the highest count rate was then selected for further experiments. Figure 21 shows the ^{174}Re yield at the different settings of the magnet.

The MDG will not work with a gas-flow of 5 L/min, so after the optimization of the magnet field, the gas-flow was reduced to 1.5 L/min. To determine the amount of radionuclides, the reaction products transported with the gas-jet were collected on a glass-fiber filter in the direct catch (DC) setup. The collection time was 10 s or 60 s, to measure the short-lived ^{170}Re isotope ($t_{1/2} = 9.2 \text{ s}$ [49]) and the slightly longer-lived ^{174}Re isotope ($t_{1/2} = 2.4 \text{ min}$ [50]). The measurements were done by γ -ray spectrometry with the HPGe-detector.

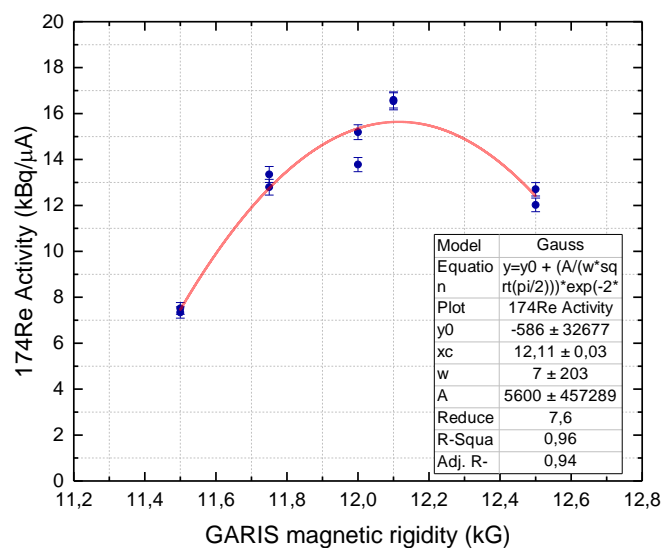


Figure 21: ^{174}Re activity plotted as a function of GARIS' magnetic field.

Transport time of rhenium isotopes

The setup of the Liquid-liquid extraction system was as shown on the schematic of Figure 21. To measure the transport time of the rhenium isotopes, a relatively short beam-pulse was generated. The amount of radioactivity collected at different positions were then measured as a function of time since the start of the pulse. This way, the time-distribution spectra were obtained. The beam pulse was 10 s long and the interval between each pulse was about 120 s. The transport time from the gas-jet chamber to four collection points (CP) (indicated in Figure 22) in the liquid-liquid extraction setup was measured; just after gas-jet transport (DC filter collection), after the Membrane Degasser, the Flow Solvent Extractor and the Membrane Phase Separator.

The pressure of the gas-jet chamber was between 114-154 kPa, and the helium gas-flow-rate was set to 1.5 L/min. The organic phase used was 0.01 M tri-octyl-amine (TOA) in toluene and the aqueous phase was 0.5 M HNO_3 . These conditions were chosen because earlier experiments proved these to give a D-value of about 1, as seen on Figure 23 [51]. The flowrate of both aqueous and organic phase was 1 mL/min.

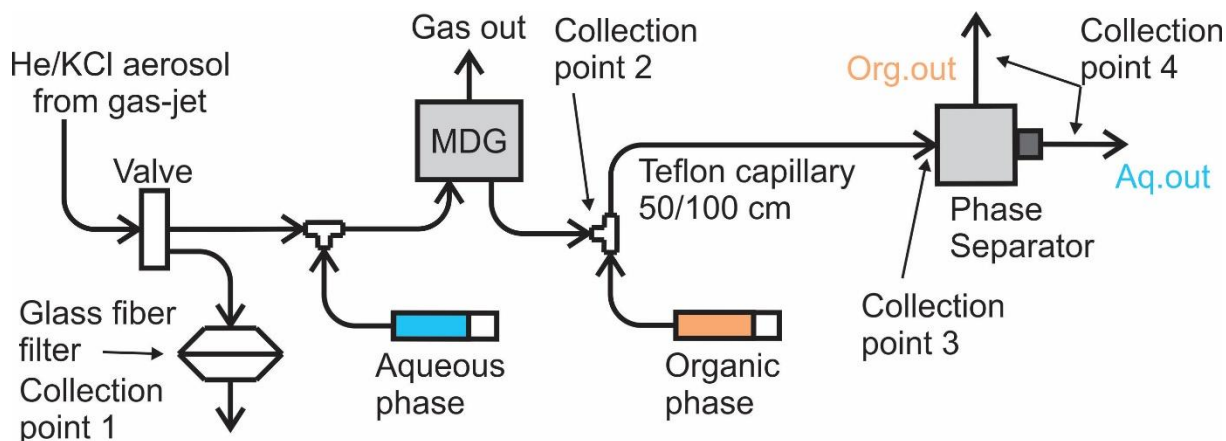


Figure 22: Schematic of the setup for experiments testing the transport time of produced rhenium

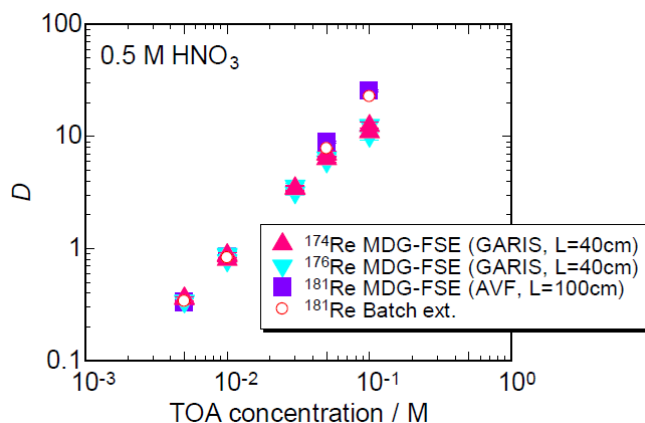


Figure 23: D -values of rhenium isotopes for varying TOA-concentration when extracting from 0.5 M HNO_3 from previous experiments performed by Y. Komori.. Figure reprinted from source [51].

The collection of radionuclides were performed cumulatively by placing the filter or vial collected in on the HPGe-detector, where the cumulative time-distribution spectra were collected. The mass-middle point of the transport curve would give the mean residence time of the radionuclides in the system up until the collection point. For collection point 2, 3 and 4, subtracting the previous collection point from it would give the mean residence time for the part of the system between the two collection points. CP1 would give the mean residence time in the gas-jet transport, CP2-CP1 the mean residence time in the MDG plus capillary, CP3-CP2 the mean residence time in the FSE and CP4-CP3 the mean residence time in the MPS. The list below explains how the measurements for each collection point were performed.

Collection Point 1: Collected on the glass-fiber filter in the DC setup, which was placed on top of the HPGe-detector.

Collection Point 2: Aqueous phase from the outlet capillary from the MDG was collected in a glass vial placed on top of the HPGe-detector.

Collection Point 3: Aqueous and organic solutions from the FSE capillary was collected together in a glass vial placed on top of the HPGe detector.

Collection Point 4: Aqueous and organic solutions from both aqueous and organic outlet capillaries from the Membrane Phase Separator was collected in a glass vial placed on top of the HPGe-detector.

Chemical yield of rhenium isotopes after passing through Membrane Degasser, Flow Solvent Extractor and Membrane Phase Separator

After investigating the total yield of ^{170}Re and ^{174}Re and the transport times of rhenium through the different parts of the membrane system, the chemical yields of the rhenium isotopes after passing through the two membrane separators were investigated.

The setup shown in Figure 21 was used in investigation of the chemical yield of rhenium after liquid-liquid extraction. Flow Solvent Extraction capillary of both 50 and 100 cm was used. Organic phase used was 0.01 M TOA in toluene, the aqueous phase used was 0.5 M HNO_3 . Again, these conditions were chosen to give a D-value close to 1 [51]. The flowrate of both aqueous and organic phase was 1 mL/min.

Aqueous phase from the Membrane Degasser (Collection point 2 in Figure 21) was collected for 10 s in a polypropylene test tube, which was measured on the HPGe. The difference between the total available yield measured at the direct catch and the yield measured after the Membrane Degasser would give the chemical yield of $^{170/174}\text{Re}$ transferred from the gas to the aqueous phase.

Both phases was then collected from the MPS (Collection point 4) for 10 s in a polypropylene tube and measured on the HPGe. The difference between the yields measured after the MDG and after the MPS would give the chemical yield of the liquid-liquid extraction.

4.2.6 Test of connecting the FSE/MPS system to the SISAK liquid scintillation detector system

Extensive tests to determine if the FSE/MPS liquid-liquid extraction system could use the SISAK liquid scintillation (LS) detectors for alpha detection were performed. Four different configurations were tested, three of which had the possibility to add radioactive radon gas to one of the liquid phases for energy calibration purposes.

To produce radon gas for detector calibration purposes a ^{227}Ac source was used. The third daughter of ^{227}Ac is ^{219}Rn , which will emanate out of the source. The helium gas is lead through a small chamber containing the ^{227}Ac source, and will carry the radon gas with it. The half-life of ^{219}Rn is 3.96 s, and its daughter ^{215}Po has a 1.781 ms half-life [32]. Both of these nuclei decay by α -emission, predominantly with energies of 6.819 MeV and 7.386 respectively. Due to the short half-lives, the detector cell would not be contaminated, and the α -energies are also lower than the α -energies from Super-heavy element nuclei. If the LS cocktail is run in a loop, one needs to beware of α -emission from the decay product ^{211}Pb ($t_{1/2} = 36$ min [32]), which decays into ^{211}Bi that emits α -particles with 6.623 MeV. The α -emission from ^{211}Bi could also be used for energy calibration. As shown in Figure 24, the ^{227}Ac -source is connected in such a way that the source can be bypassed by switching the two three-way valves into the bypass position. The added advantage of this is that the source is sealed when in bypass. A mass-flow meter/controller was used to select and monitor the helium gas-flow.

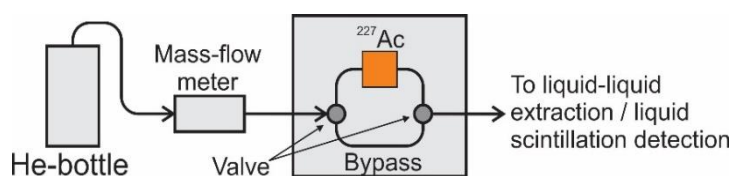


Figure 24: Schematic of the supply of helium and ^{227}Ac source, providing $^{219}\text{Rn}/^{215}\text{Po}$ for the connection experiments.

A scintillation detector from the SISAK system [7] was used without modification. The cell has a meander-shaped track with a volume of 5.5 mL. It is carved out of Teflon block (Figure 25) with a 1 mm of Kel-F disc fitted on top to protect the Plexiglas light-guide from the LS cocktail. The Kel-F disc also serve to scatter the scintillation light more evenly onto the photocathode of the photomultiplier tube, which will enhance the energy resolution (page 48 in [18]).

Organic and aqueous phase used in the membrane system was 0.1000 M TOA/Toluene and 0.05 M HCl respectively. These conditions were chosen because it would give a D-value of around 1. The flow-rate of each of the phases was 1 mL/min.



Figure 25: Teflon block meander detector cell for the liquid scintillation detector.

Detector electronics

In the work presented in this thesis, there has not been time to investigate and possibly improve the electronic setup to acquire and process the pulses from the PMT. The setup used here is equal to what has been used for a range of SISAK experiments on super-heavy elements, and is described in detail in [7, 52]. The following is a brief description of how the signal from the PMT is processed.

From the PMT the signal is sent to a charge-sensitive pre-amplifier to amplify the pulse, before being sent to a delay-line amplifier (ORTEC, M460). From the delay-line amplifier (DLA) two signals are sent out; a unipolar signal to the delay amplifier (ORTEC, M427A), which contains the pulse-height, to the delay amplifier and a bipolar signal to the Pulse Shape Discriminator (ORTEC, M552). The Pulse Shape Discriminator (PSD) uses the difference in the pulse shapes [21] from different types of particles, caused by the difference in ionization trail length and therefore ionization densities, to discriminate between γ/β and α events. Two signals are sent from the PSD to the Time to Amplitude Converter (TAC)/Single Channel Analyzer (ORTEC, M567), one for starting the TAC clock, and the other for stopping it. The PSD unit generates the start signal when the falling edge of the pulse goes through 50 % of the maximum amplitude. The stop signal can be selected to trigger at certain fractions of the maximum amplitude, e.g. 10 %. Both signals are generated by constant fraction techniques [53]. In addition, the stop signal can be generated at the zero-crossing point of a bipolar signal. The bipolar signal is generated by first integrating the PMT pulse, and then doing a double differentiation, turning it into a bipolar pulse. The zero-crossing of this pulse is dependent of the rise and decay time of the integrated pulse [21] and will therefore also be a function of the pulse shape. Experience has established that the zero-crossing stop signal gives the best α/β discrimination, and as therefore used in this work.

The window of the Single Channel Analyzer (SCA) output of the TAC was used to select the α -particles from the PSD time spectrum. The gate signal from the SCA was then used to gate the ADC measuring the pulse height. In this way, the unwanted β -part would not be measured. The other ADC received the signal from the TAC output.

The acquisition system stores the data as “list-mode”, i.e. every single pulse is recorded and time-tagged. In this way, different gates on the time and energy spectrum can be set after the experiment has been conducted. This feature was not used in the work presented here. A schematic showing the setup of the electrical pulse shape discrimination is shown in Figure 26.

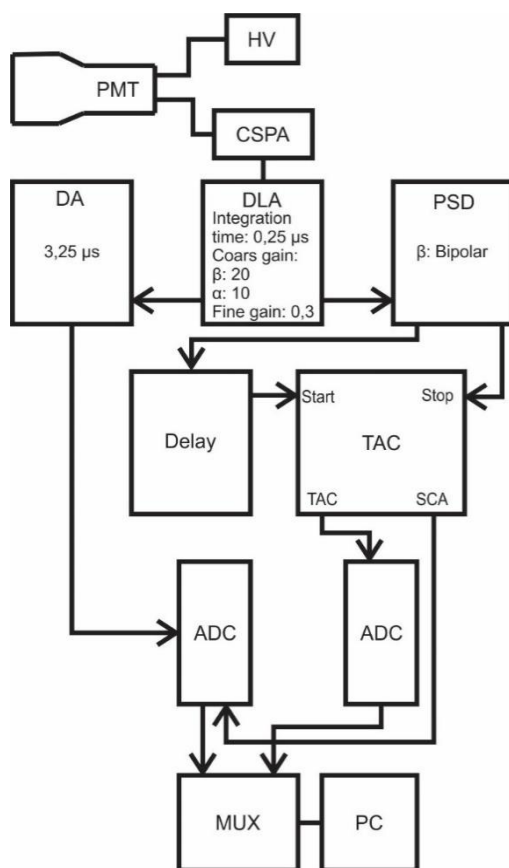


Figure 26: Schematic of the electronics for scintillation detection and pulse shape discrimination. Explanation for the abbreviations: HV – High Voltage, PMT – Photo Multiplier Tube, CSPA – Charge Sensitive Pre-Amplifier, DLA – Delay Line Amplifier, DA – Delay Amplifier, PSD – Pulse Shape Discriminator, TAC – Time to Amplitude Converter, ADC – Analog to Digital Converter, MUX – Multiplexer.

Different configurations of the system setup

To determine if the membrane liquid-liquid extraction system could use the SISAK liquid scintillation detectors, the four setups listed below were tested. The setups were tested to see if the output from the MPS could overcome the backpressure from the detector-cell. Detection of α -particles were also tested for setup II, III and IV.

- I. To first see if it was at all possible to connect the two systems, only the FSE, MPS, detector and a pump were connected. This setup is as shown in Figure 27. Pure toluene was added to the detector system from a measuring beaker. The output from the detector was fed to the same beaker, thus recycling the toluene. The pump driving the toluene through the detector system was placed before the T-connector where the Flow Solvent Extractor and Membrane Phase Separator are connected. This implies that the MPS output must overcome the backpressure created by the pump forcing the toluene into the detector-cell. The flow in the detector system (0.2 – 0.8 mL/s) was measured with a flow-meter. A phase-purity meter (PPM) was used to monitor the phase separation performance of the MPS. The phase-purity meter, which is mounted around the capillary for the organic outlet of the MPS, creates a voltage-signal that is proportional to the transmission of light through the liquid inside the capillary. To control the purity of the

organic and aqueous phases, the “strangler” on the aqueous output from the MPS was adjusted. I.e., the “strangler” adjusted the backpressure that the aqueous phase has to overcome, thus controlling the pressure equilibrium in the MPS, ensuring that only the organic phase penetrates the membrane.

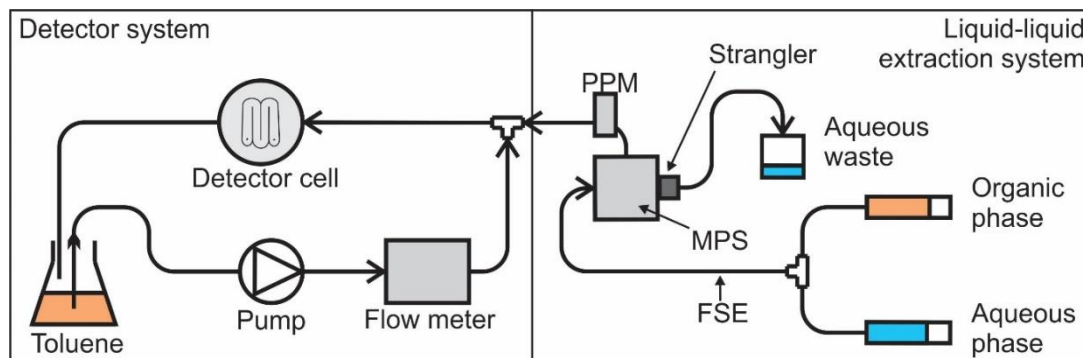


Figure 27: Setup I for testing the compatibility of the membrane and detector systems.

- II. When mixing in the He-gas, and thereby the ^{219}Rn gas, a degasser was added to the system as shown in Figure 28. The centrifuge degasser connected here was a standard SISAK degasser without modifications, equal to those used in previous SISAK experiments [7]. The degasser was connected after the flowmeter and before the T-connector where scintillator is mixed with the organic output from the MPS. The degasser was set up with a mechanical mixer of the “zigzag” type (Figure 78 in Appendix E) to enhance the transfer of activity from the gas into the liquid, and more efficient removal of dissolved O_2 ¹. In this setup, the normal bypass valves, used to bypass the detector-cell (e.g. when the solution is unclear, or the cell is waiting for “daughter events”), were added to the setup. These valves were not added to setup I described above (Figure 27), since this was primarily intended only as an initial test to see if the MPS would at all be able to overcome the backpressure from the detector-cell. The bypass valves was controlled from the computer, and normally they would be triggered if the phase-purity meter detected aqueous phase in the MPS organic output. This type of trigger was not engaged for the experiments described here. With this setup, tests with α -measurements were performed in addition to testing if the detector-cell backpressure could be overcome. Because of this, a high quality liquid scintillator was used instead of only pure toluene as in setup I. The scintillator was made from preparing a 1 L cocktail containing 4 g/L PBBO and 255 g/L 1-Methylnaphtalene was used.

¹ It can be noted that the absolutely necessary flushing of O_2 from the organic phase in the SISAK experiments, with flow-rates in the 0.5 mL/s range, is probably not needed with the configurations tested in this work. The low flow-rate of the organic phase from the MPS, compared to the LS flow-rate, makes it likely that the organic phase’s O_2 contribution to the mixture entering the detector-cells will not influence the system’s PSD performance. For this same reason, it should be possible to recycle the LS-cocktail for long periods of time. This would solve one of the major problems of the SISAK setup, which is the large consumption of (expensive) LS chemicals, in addition to the generation of large amounts of organic waste.

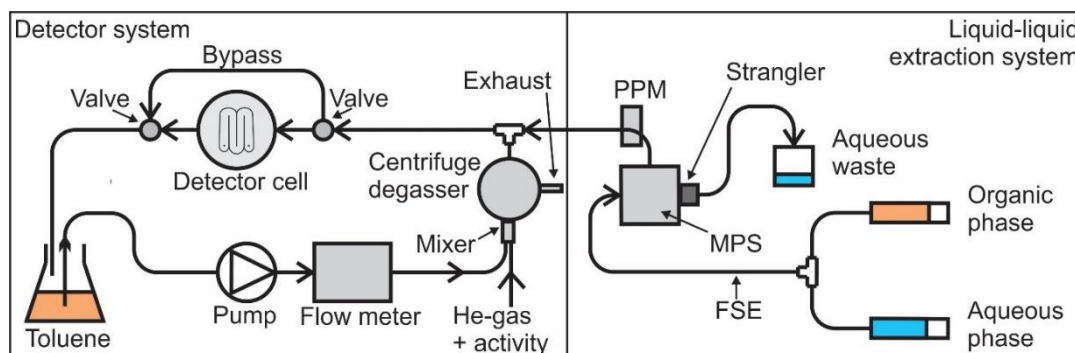


Figure 28: Setup II for testing the compatibility of the membrane and detector systems.

- III. As the radioactivity need to be added to the aqueous phase in a stage before the liquid-liquid extraction, the centrifuge degasser was switched out with the MDG. The MDG was therefore placed before the MPS and FSE, outside the detector system as shown in Figure 29. This was also done to investigate if it would be easier to overcome the backpressure of the detector-cell if the centrifuge degasser was switched to the MDG. The gas was pumped to the exhaust by the vacuum pump, and a liquid trap was added to ensure no liquid escaped the system. The pressure was measured with a pressure-meter.

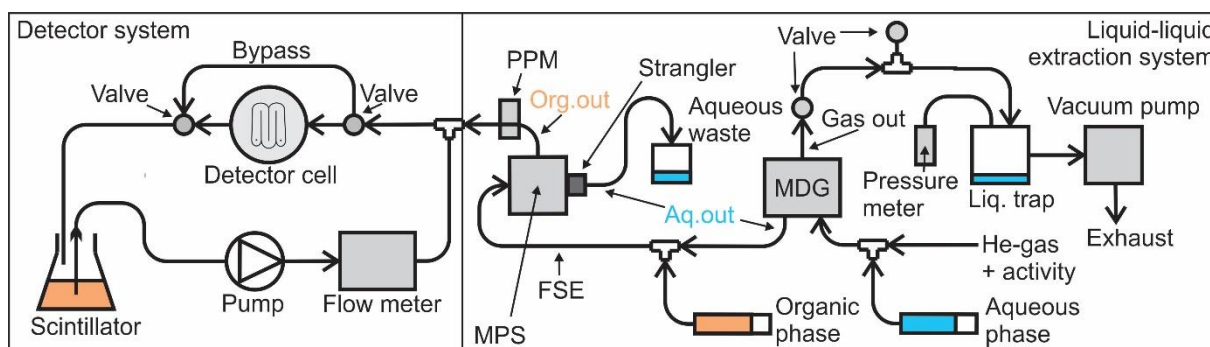


Figure 29: Setup III for testing the compatibility of the membrane and detector systems.

- IV. The same setup as in III, but the pump was moved from being before the detector cell to being after the detector cell. This was done to investigate if the backpressure from the detector-cell would be easier to overcome if the pump pulled the cocktail through the detector-cell, instead of pushing it through. This setup is shown in Figure 30.

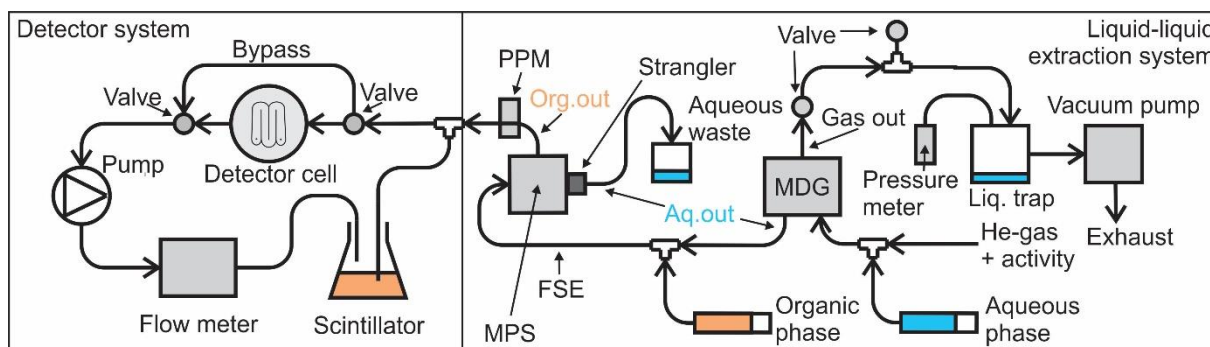


Figure 30: Setup IV for testing the compatibility of the membrane and detector systems.

4.3 Data acquisition and analysis methods

4.3.1 Gamma spectra

The count rates from these γ -lines were extracted from the measured γ -spectra. The time of collection in each spectrum was low, so when analyzing the γ -spectra, spectrum peaks that contained more than 10 counts were considered a peak and marked as a region of interest (ROI). Using customized versions of Maestro's library files containing the nuclei of interest for each specific target, the peaks were identified with respect to emitting nucleus, and saved to a Maestro report-file (text file with the lists of the fitted ROIs). Count rate for each γ -line were extracted from the ROI files. The count rates were then corrected for the beam intensity, the γ -intensity, the detector efficiency and half-life of the nuclide. The correction of these are shown in the calculations in Appendix D

4.3.2 Transport time measurements

The data from the transport time measurements was collected in "list-mode", i.e. each single event were written to a file, instead of being hardware-sorted into a spectrum. Each event in the list-mode file was timestamped. This way, different parts of the energy spectrum could be selected ("gated"), and the time spectra of the corresponding events was projected into an energy spectrum. This was achieved by using a LabVIEW program, "riken-re-ttime.exe" [9], written by Jon Petter Omtvedt. The user interface is shown in Figure 31.

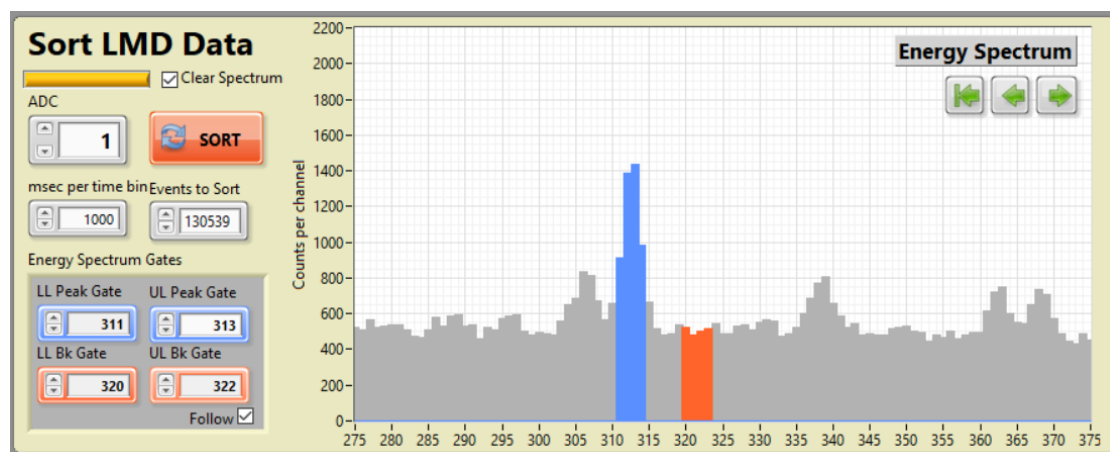


Figure 31: Screenshot from "riken-re-ttime.exe" showing a time-spectrum of a single sorted energy peak from a single list-mode file from transport only through the gas-jet. The gray graph shows the beam, the blue graph shows the total counts in the blue marked peak, the orange shows the counts in the marked background and the green graph shows the blue graph minus the background.

As can be seen from the figure, a given peak of interest could be chosen, along with a representative background. The background gate is important, as the gate for the peak of interest sits on top of the general background, which contains mainly Compton event from a long range of nuclei. The background will most likely have a different time-distribution than the nucleus the gated γ -ray peak belongs to. The time spectra from both the peak and the background gates are projected, where the background spectrum then is subtracted, and the results will then represent the nucleus being investigated. As seen in Figure 31, the width of the time bins in the projected time spectrum can be selected. This decides how wide the time range each column (“bin”) should be. For the analysis performed here, a bin with of 1 second was found to be a reasonable compromise between time resolution and the amount of counts in each bin. An example of a projected time-spectrum is provided in Figure 32. In this time-spectrum, the counts from the 156 keV γ -ray from ^{170}Re from a single replicate of the transport time measurement of the gas-jet is projected.

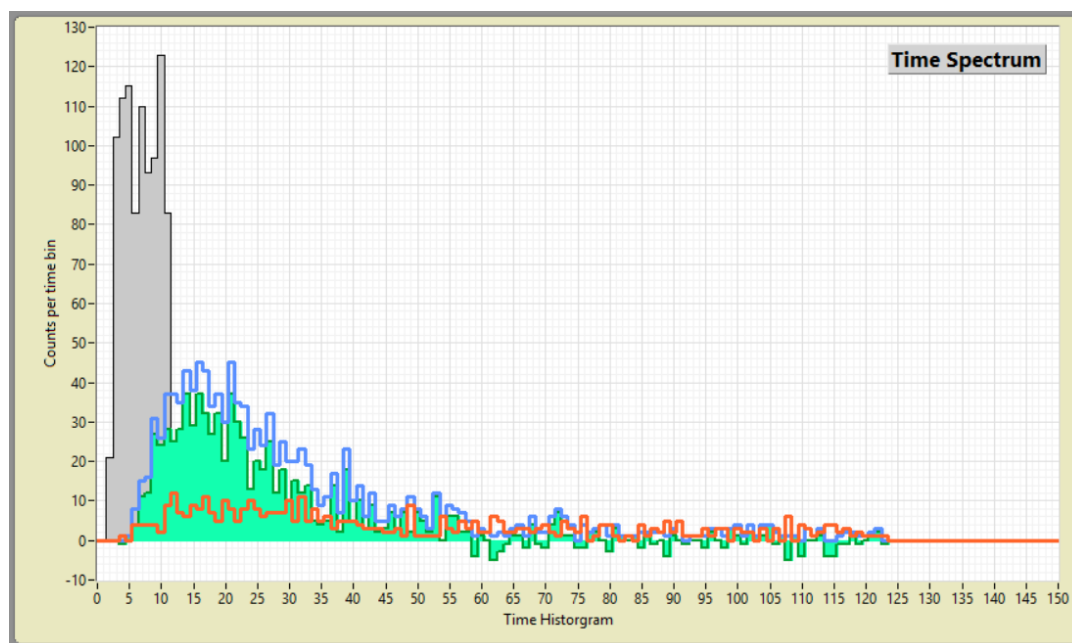


Figure 32: Screenshot showing the energy spectrum in "riken-re-ttime.exe" written by Jon Petter Omtvedt. Here the blue marked peak is the peak for the 156 keV γ -ray from ^{170}Re , while the orange marked area is the background above the peak. The x-axis in the energy spectrum are channels with channels corresponding to the energy half the channel number.

For the replicates performed under the same conditions, and at the same collection point, the time-spectra from the three γ -lines from ^{170}Re were added together to give better statistics, and were imported to Origin. The added time spectra for ^{170}Re through the gas-jet is shown in Figure 33. This time spectra was then corrected for radioactive decay, giving the graph shown in Figure 34. This graph was then fitted with the Origin function “SGompertz”, which is a sigmoidal function that is used in mathematical models where the growth is low at the start, increasing to a steep slope, before it slows down again at the end [54]. The curve from fitting with the SGompertz function was then differentiated. This differentiated curve shows the true shape of the transport curve of the ^{170}Re nuclides [55]. The transport curve, shown in Figure 35, was

fitted with a “LogNormal” [56] curve, which gave the mass middle point for the integral of the curve. By subtracting the time at the middle of the 10 s beam pulse from the mass middle point, the mean residence time is calculated. The analysis showed here was for the transport time measurement of the gas-jet transport. The graphs from the same analysis of the rest of the system setup shown in Figure 20 is shown in Figure 60 to 74 in Appendix D.

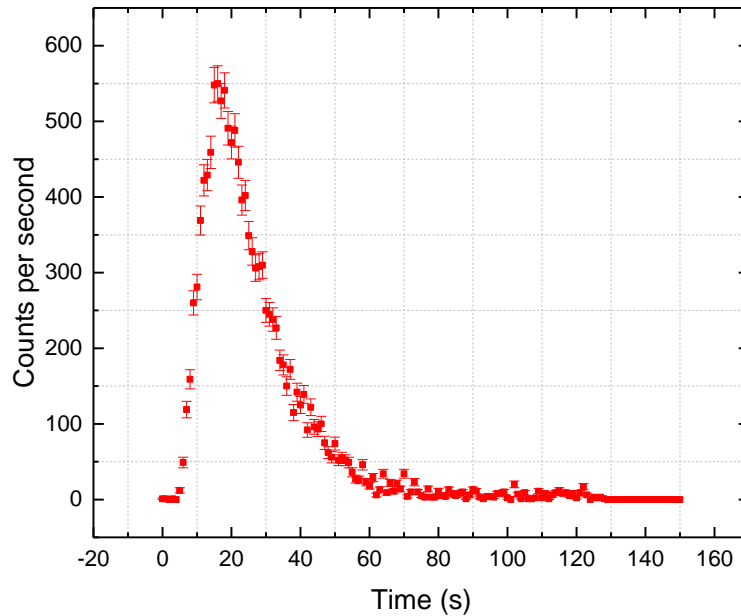


Figure 33: Plot of the added time spectrum of counted ^{170}Re through the gas-jet.

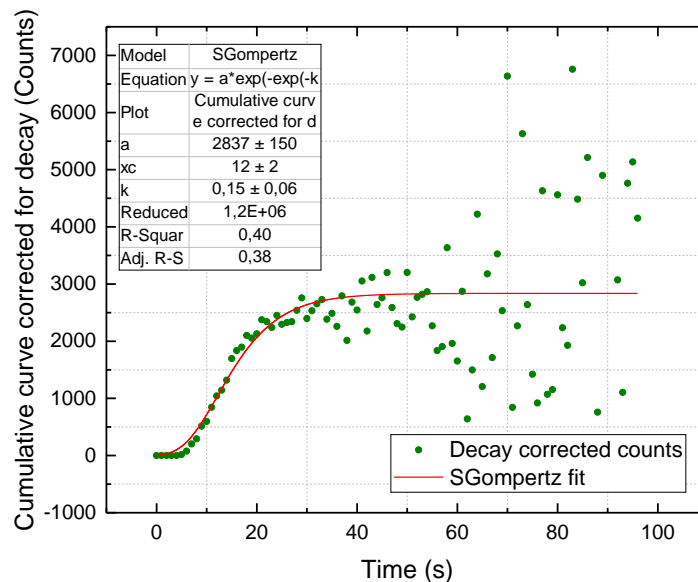


Figure 34: The plot in Figure 33 corrected for radioactive decay. The fitting with SGompertz function (line) gives the growth curve of the ^{170}Re nuclei collected on the glass-fiber filter on top of the HPGe-detector.

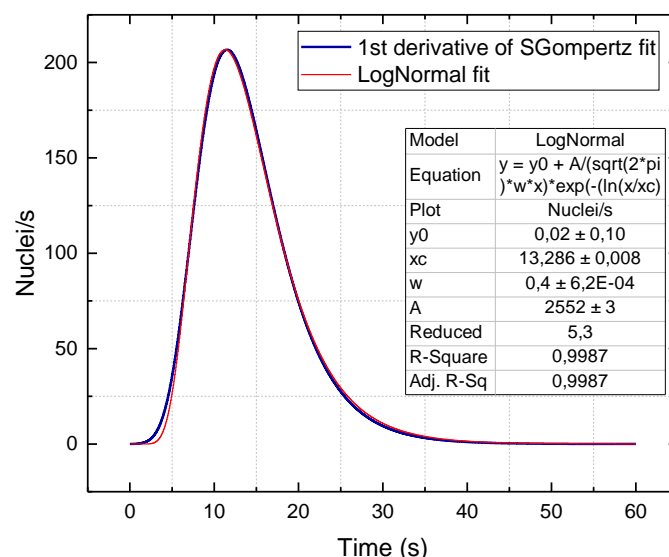


Figure 35: Graph of the true transport function, fitted with the lognormal function. Middle point of the integral of the graph is given as "xc" in the lognormal fit response table in the graph.

Connecting of the membrane system and SISAK detector system

When the investigation of the connection of the on-line liquid-liquid extraction system, consisting of the MDG, FSE and MPS with the SISAK liquid scintillation detector system, was investigated, α -spectra were generated. The α -spectra were measured in the different setups to investigate whenever the organic phase from the MPS could overcome the backpressure from the detection-cell. The backpressure must be overcome without loss of yield, from phases ending up in the wrong phase, and without the pressure of the gas-jet being affected, so there would be no danger of the RTC's vacuum window breaking. The transport time of the two connected systems has to be as low as possible to be able to measure super-heavy elements. This is especially problematic with low liquid flow in the detector system, as the capillary could be rather long, causing a longer transport time. By measuring on short-lived nuclides, the connected system's ability to measure nuclides with half-lives similar to super-heavy element nuclei used for chemical studies, e.g. 14.4 s ^{265}Sg [57] and 17 s ^{267}Bh [58].

The alpha events from the PMT is collected in list-mode with the acquisition program Loke [59], which is LabVIEW program developed for the SISAK alpha detector system and has been used since 1998 [7, 9]. For the test experiments with the setups described previously, Loke's list-mode data was not used. Instead, the total energy and PSD spectra that is projected during the acquisition were saved directly from Loke. Loke also has the ability to set a gate on e.g. the alpha region of the PSD spectrum and project this into a third spectrum, which is referred to as the PSD-gated energy spectrum. The measured peaks was analyzed with Volund version 5.0 [60], a program written by Jon Petter Omtvedt, to determine the size and position of the measured α -peaks and to get the energy calibration. An example of an α -spectrum measured with setup II for 5 minutes is shown in Figure 36. The spectrum shows the peaks from ^{219}Rn (6.819 MeV and 6.553 MeV) and ^{215}Po (7.386 MeV). In the investigation of the different setups, the FWHM was not necessary to measure with great preciseness, since main goal was to test if

short-lived activity could be measured with the different setups at a lower flow-rate than has previously been used with the SISAK system.

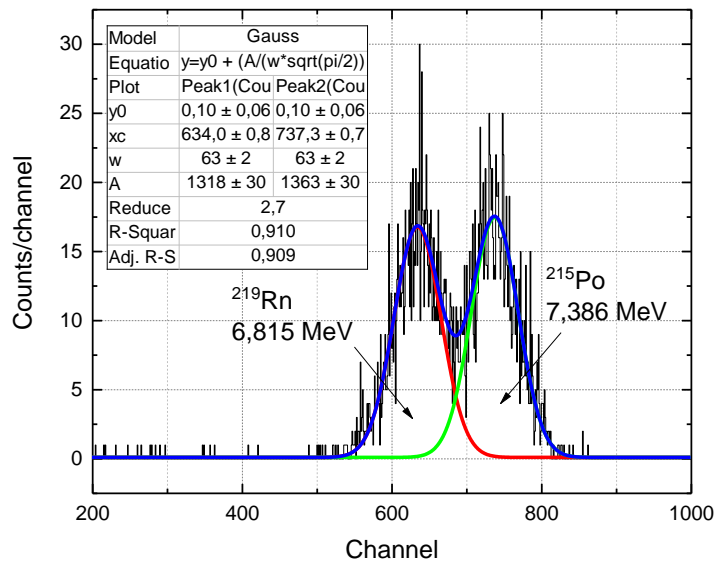


Figure 36: Plot of an α -spectrum of ^{219}Rn and ^{215}Po measured with setup II for 5 minutes

When the different setups listed in Chapter 4.2.6 was investigated, the amount of quenching was monitored, as the quenching in the connected system needs to be kept to a minimum. For the investigation to determine the degree of quenching, the Compton-electron spectra measured with the ^{137}Cs source outside of the LS-cell. The Position of the Compton edge will move towards lower channel numbers when the amount of quenching increases. To determine the Compton edge position, the spectra measured of the ^{137}Cs source were imported to Origin, where the program's combined smoothing and second derivative fitting function was applied. The smoothing was performed as a walking average over 31 channels. An example of this type of fit is shown in Figure 37. The inflection point was then graphically determined by the point where the second derivative passer through zero. This point is used as a measure of the quenching [61].

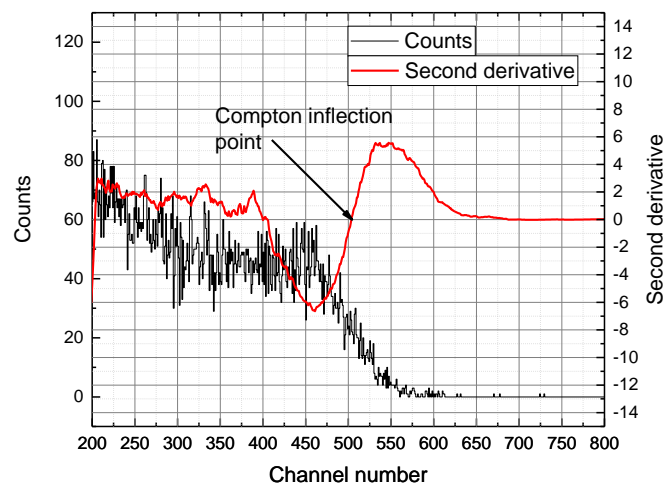


Figure 37: Measured Compton spectrum (black line) with plot of the second derivative of the spectrum. Where the second derivative curve crosses zero on the uphill part of the graph is the Compton inflection point.

For the connection of the liquid-liquid extraction system and SISAK system to be successful, the phase purity of both organic and aqueous phase has to be stable and clean. The backpressure from the detection-cell will affect the pressure equilibrium in the MPS, affecting the purity of the phases exiting the MPS. When monitoring the purity of the organic and aqueous phase, phase-purity meters were used. The voltage pulse from the phase-purity meters were monitored and plotted in the LabVIEW program “RIKEN UiO_control_system v03 21Oct2016” [62]. Whenever one of the phases was unclean, the voltage created by the PPM would drop. Graphs A and B in Figure 38 shows, respectively, the output of clean phases and the response when one phase leaked into the other phase for a short time, causing the created voltage signal to drop.

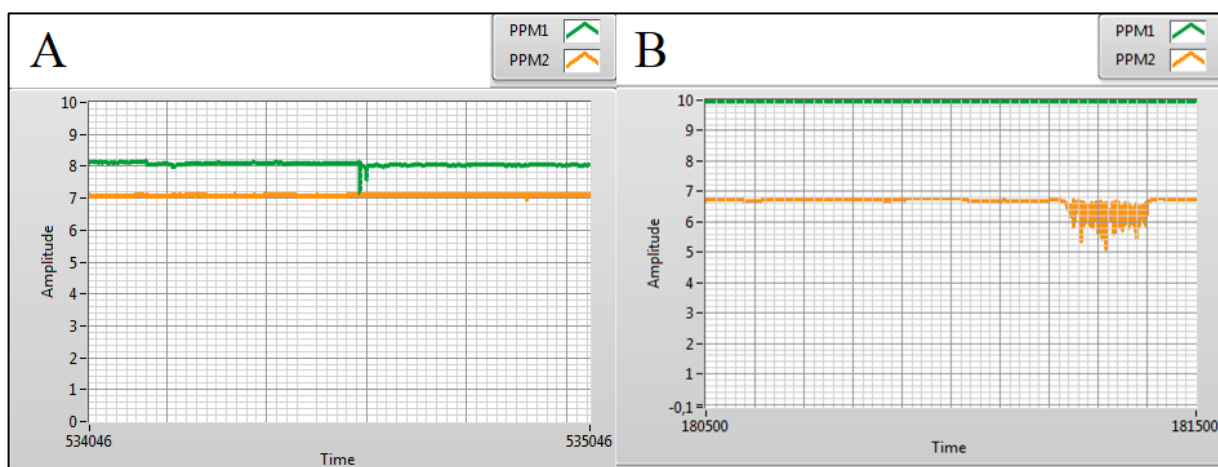


Figure 38: Graphs from the phase purity meters monitoring the phases coming out of the MPS. Graph A shows pure phases, while graph B shows organic phase (green) leaking into the aqueous phase (orange).

4.4 Experiments and results

4.4.1 Rhenium experiments

Production of rhenium isotopes

From the aerosols collected on the glass-fiber filters, the count rates of produced ^{170}Re and ^{174}Re . For ^{170}Re , the three strongest γ -lines (156.67 keV, 305.7 keV and 413.1 keV) were used in the spectrum analysis. For ^{174}Re , the two strongest γ -lines (112.4 keV and 243.7 keV) were used in the spectrum analysis. The analysis method is described in chapter 4.4. The measurements described in this chapter was performed together with Y. Komori et al.

Spectra that had too short collection time, giving a low count rate, was added together to get spectra that would be easier to analyze, because of the higher count rate compared to the single spectrum in the same amount of time. An example of an analyzed spectrum from the rhenium production and gas-jet transport is shown in Figure 39 and a larger version of the spectrum is shown in Figure 75 Appendix D.

The spectrum in Figure 39 shows a typical analyzed γ -ray spectrum, where the target was irradiated for 10 seconds and collected on a glass-fiber filter in the DC. The most important features to note are the ^{170}Re and ^{174}Re isotopes with half-lives of 9.2 ± 0.2 seconds [49] and 2.40 ± 0.04 minutes [50], respectively.

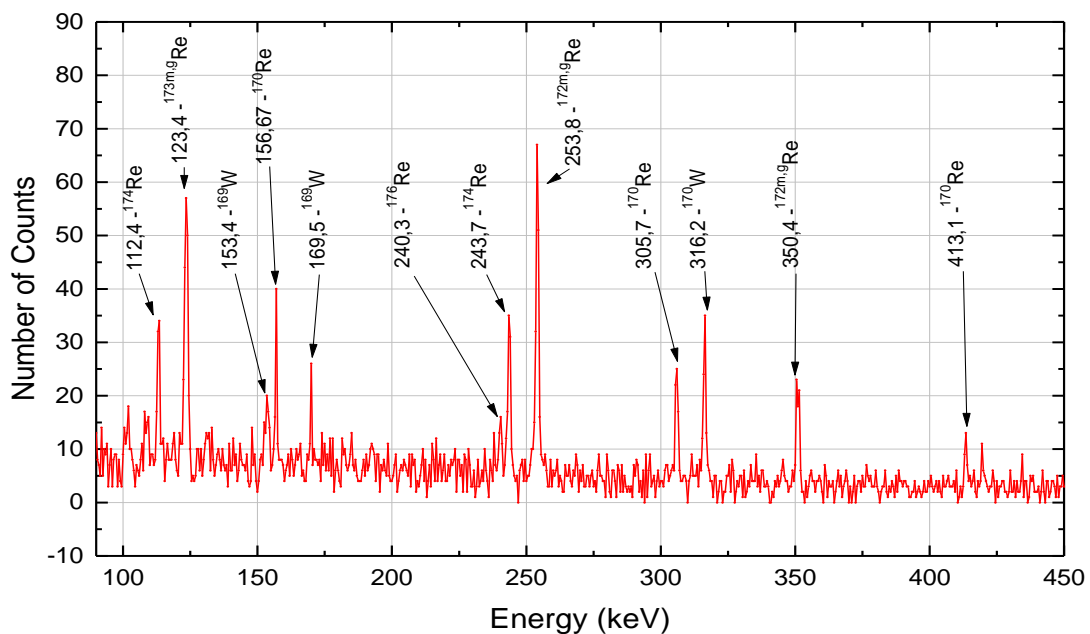


Figure 39: An example of a typical γ -ray spectrum after 10 seconds of aerosol collection on glass fiber filter.

Yield from GARIS

The γ -spectra used to determine the magnetic field of GARIS that gave the highest yield of ^{174}Re were measured by collection aerosols on the DC setup during 60 s where the target was irradiated. The depth of the recoil transfer chamber (RTC) was here set to 5 cm, as to ensure that none of the produced nuclei hit the back wall of the RTC. The magnetic fields where aerosol collection was performed was at 11.5 kG, 11.75 kG, 12.0 kG, 12.1 kG and 12.5 kG. Two replicates were performed for each setting of the magnetic field, giving a total of 10 aerosol collections. The glass-fiber filters were removed from the DC setup, placed in zip-lock bags, and after 60 s delay they were measured on the HPGe-detector for 60 s.

Figure 21 in Chapter 4.2.5 showed the yield of ^{174}Re plotted against the settings of the magnet in GARIS. The data points were fitted with a Gaussian curve, showing that the optimal magnetic field for ^{174}Re is at the curve maximum of 12.1 ± 0.03 kG.

Gas-jet transport yields

Measurements of the yields of $^{170/174}\text{Re}$ were performed when the depth of the RTC was changed to 2 cm. Here, a total of 5 replicates were performed where the irradiation/DC collection time, cooldown time and measurement times were all 60 s each. The glass-fiber filters were removed from the DC setup, placed in zip-lock bags and then measured with the HPGe-detector. Two replicates were performed where the irradiation/DC collection time was 10 s, the cooling time was 22 s and the measurement time were 30 s.

After reducing the gas flow from 5 L/min to 1.5 L/min, another two replicates measuring the yield of ^{174}Re were performed. The glass-fiber filters were removed from the DC setup, placed in zip-lock bags and then measured with the HPGe-detector. The irradiation/DC collection time, cooldown time and measurement times were all 60 s each for both measurements.

The yields from the last two measurements used to maximize the yield from GARIS, the yields from shortening the RTC and reduction of the gas-flow-rate are listed in Table 7. Figure 40 shows that a gas-jet chamber depth of 5 cm, helium flow-rate of 5 L/min and a pressure of 77 kPa gives a gas-jet transport yield of 86 ± 3 %. By decreasing the chamber depth to 2 cm, the gas-jet transport yield falls to 33 ± 1 %, which clearly indicating that a significant fraction of the EVRs are shot into the back wall of the RTC.

Increasing the pressure of the chamber at 2 cm depth shows that the transport yield increases with increasing pressure. At over 123 kPa, the transport yield reaches over 80 %, and a pressure of 151 kPa gives a transport yield of 84 ± 3 %. The explanation for this is that as the pressure of the gas increases, the stopping power in the gas is at some point large enough to ensure that no EVRs reach the back wall of the RTC, causing them to be lost. 123 kPa is above this point. The Membrane Degasser can't cope with 5 L/min gas-flow. Changing the helium flow-rate from 5 L/min to 1.5 L/min, but keeping the pressure above 123 kPa, did not notably change the gas-jet transport yield.

Table 7: Transport yields with uncertainty (unc.) of ^{174}Re in the gas jet system with varying pressure in the gas-jet chamber, 2 or 5 cm gas-jet chamber depth and a helium gas-flow-rate of 1.5 or 5 L/min.

RTC pressure, kPa	RTC depth, cm	Gas flow, L/min	Yield, %
77	5	5	86 ± 3
77	5	5	86 ± 3
77	2	5	32 ± 1
77	2	5	34 ± 2
123	2	5	81 ± 3
151	2	5	84 ± 3
103	2	5	71 ± 3
150	2	1,5	88 ± 3
150	2	1,5	81 ± 3

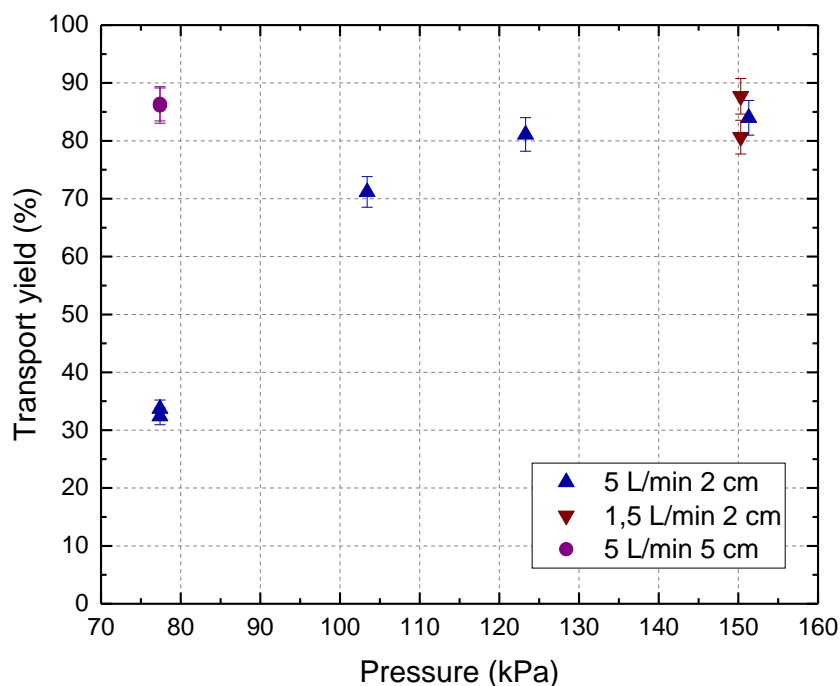


Figure 40: Graph showing the efficiency of the gas-jet transport of ^{174}Re as a function of the gas-jet chamber pressure for different gas flows and RTC depths.

Rhenium available at chemistry laboratory

To measure the yields of $^{170/174}\text{Re}$ available at the chemistry laboratory, five measurements were performed where the irradiation time was between 10 and 12 seconds, with as short as possible cooling time and a 30 or 20 second measurements. For three of the measurements the irradiation/DC collection time was 10 seconds, with 44 s, 15 s and 14 s cooling times and 30 s, 20 s and 20 s measurement times respectively. One measurement had an irradiation time of 12

s, cooling time of 34 s and measurement time of 20 s. Another replicate had an irradiation time of 11 s, cooling time of 15 s and measurement time of 20 s.

The total amounts of ^{170}Re and ^{174}Re activity from aerosol collection on glass fiber filters for 10 seconds are given in Table 8. This activity represent the amount that will be fed into the chemistry apparatus. Due to the short half-life of ^{170}Re , the irradiation and measurements performed to detect this nuclei were short. The short irradiation and measurement times caused the counting statistics to be rather low.

Table 8: Total available amounts of ^{170}Re and ^{174}Re at chemistry laboratory in RIKEN after aerosol collection for 10 seconds.

Nuclei	Activity, kBq/ μA
^{170}Re	8.2 ± 0.7
^{174}Re	2.5 ± 0.5

Investigation of the total available amount of ^{174}Re were performed by using a 20 μm aluminum catcher foil behind the target. The target was irradiated for 60 s, and was subjected to γ -spectrometry for 60 minutes after a cooling time of 260 s. Because of the short half-life of ^{170}Re , the aluminum foil was not used to measure the total available amount of ^{170}Re . A measurement of the yield of $^{170/174}\text{Re}$ from the gas-jet was therefore performed with DC, where the irradiation time was 10 s, the cooling time was 26 s and the glass-fiber filter was subjected to γ -spectrometry for 10 min.

Figure 41 shows the decay curve for the 305.7 keV γ -line for ^{170}Re measured on glass-fiber filter with the DC setup as described in the last part of the previous paragraph. Even with low counting statistics, the half-life was measured to be 8.0 ± 1.8 s, which is close to the literature value.

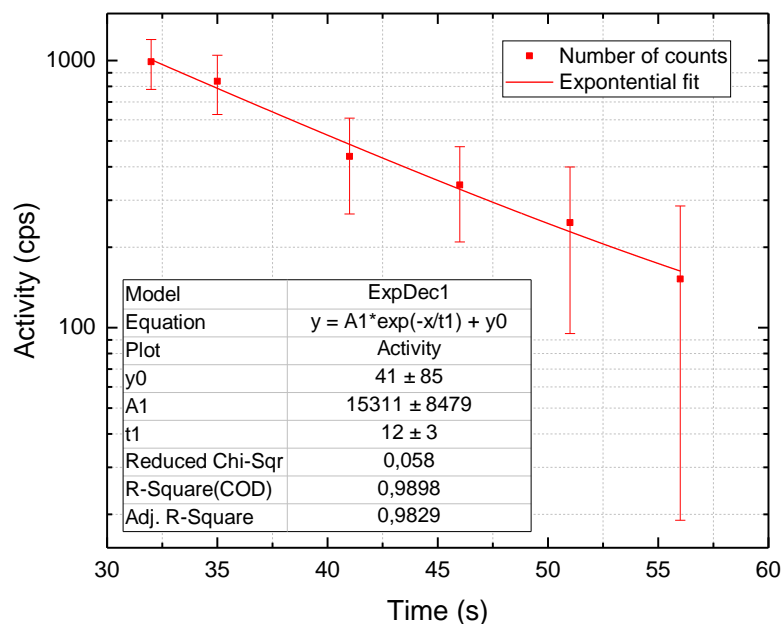


Figure 41: Logarithmic plot of the radioactive decay of the 305.7 keV γ -line from ^{170}Re , fitted exponentially to find the measured half-life of ^{170}Re .

Transport time measurements

To measure the time it takes for the produced to pass through the different parts of the liquid-liquid extraction system, the mean residence time of ^{170}Re was measured through the system to the collection points described in Chapter 4.2.5. The measurements were performed by cumulatively collecting the radioactivity of ^{170}Re on top of the HPGe-detector. For all the transport time measurements, the counts from the three strongest γ -lines of ^{170}Re (156.67 keV, 305.7 keV and 413.1 keV) was used. All the measurements of transport time were performed by irradiating the target for 10 seconds, and the measurement time on the HPGe-detector was between 2 and 3 minutes.

For the measurements of the transport time through the gas-jet, the ^{170}Re nuclides were collected on a glass-fiber filter in the DC setup, which was placed on the HPGe-detector. 16 replicates of measuring the transport time through the gas-jet were performed. In the first nine measurements, the timing of the registered counts where not registered, so seven additional replicates were performed.

For the measurements of the transport times through the MDG, the FSE and the MPS, the ^{170}Re nuclides were collected in glass vials which were placed on the HPGe-detector. The transport time through the gas-jet, 5 cm capillary, the MDG and 20 cm capillary (CP2) was measured in four replicates. The transport time through the gas-jet, 5 cm capillary, the MDG and 50 cm FSE (CP3) was measured in five replicates, while with 100 cm FSE the transport time was obtained with four replicates. For the transport times through the gas-jet, 5cm capillary, the MDG, 50 cm FSE, the MPS and 20 cm capillary (CP4), four replicates were measured, and four replicates were measured with the 100 cm FSE.

The measured mean residence times are given in Table 9. The table shows that the time needed to pass through the MDG and 25 cm capillary of 0,50 mm inner diameter is 13.7 s (18.9 s - 5.3 s = 13.7 s). With the flow-rate 1 mL/min, the time through the 20 cm length capillary is estimated to 2.4 s, the estimated time it takes for the ^{170}Re atoms to dissolve in the aqueous solution and move through the MDG and 5 cm capillary is 11.3 s.

The time to pass through the FSE is calculated to be 5.9 s (22.5 s - 11.3 s - 5.3 s = 5.9 s) for the 50 cm capillary and 6.7 s (23.2 s - 11.3 s - 5.3 s = 6.7 s). With a flow-rate of 2 mL/min, the estimated time through the 50 and 100 cm capillary is 2.9 s and 5.9 s respectively. There is some delay observed in the measured values, 3.0 s for the 50 cm capillary and 0.8 s for the 100 cm capillary.

The time to pass through the MPS is calculated to be 3.8 s (28.7 s - 22.5 s - 2.4 s = 3.8 s) for measurement with the 50 cm capillary and 3.9 s (29.5 s - 23.2 s - 2.4 s = 3.9 s) for the 100 cm capillary.

Table 9: Mean residence times with uncertainties (unc.) measured through the different parts of the membrane system.

Collection Point	Total system measured	Mean residence time, s
1	Gas-jet Direct Catch	5.3 ± 0.4
2	MDG + 5 cm and 20 cm capillary	18.9 ± 0.4
3	MDG + 5 cm capillary + FSE (50 cm)	22.5 ± 0.4
3	MDG + 5 cm capillary + FSE (100 cm)	23.2 ± 0.4
4	MDG + 5 cm capillary + FSE (50 cm) + MPS + 20 cm capillary	28.7 ± 0.4
4	MDG + 5 cm capillary + FSE (100 cm) + MPS + 20 cm capillary	29.5 ± 0.4

Chemical yield of rhenium isotopes after passing through MDG, FSE and MPS

To measure the chemical yields of $^{170/174}\text{Re}$ through the MDG, the aqueous phase from the MDG was collected for 10 s in a polypropylene vial, and then measured with the HPGe-detector. Four replicates were performed to measure the chemical yield of rhenium isotopes through the MDG. The chemical yields of $^{170/174}\text{Re}$ through both the MDG, 50 cm/100 cm FSE and the MPS was measured by collecting both phases from the MPS in a polypropylene vial. Three replicates were performed with the 50 cm FSE and five replicates were performed with the 100 cm FSE. The chemical yields of rhenium isotopes, after going through the MDG and after liquid-liquid extraction and phase separation, are presented in Table 10. Analysis and calculations for these results were performed by Y. Komori [51].

Table 10: Chemical yields of ^{170}Re and ^{174}Re through the MDG, FSE (50 or 100 cm) and MPS, with averages and uncertainties (unc.). Run number 3-1 is not included in the average. Reprinted from source [2].

Run no.	Setup	Pressure in the gas-jet chamber, kPa	Chemical yield, %	
			^{174}Re	^{170}Re
1-1	MDG	112.4	23 ± 4	13 ± 3
1-2	MDG	112.5	19 ± 3	7 ± 2
1-3	MDG	112.5	32 ± 5	14 ± 3
1-4	MDG	112.4	13 ± 3	9 ± 3
Ave.	MDG	112.5	22 ± 8	11 ± 3
2-1	MDG + 50 cm FSE+ MPS	139.5	13 ± 2	5 ± 2
2-2	MDG + 50 cm FSE+ MPS	139.2	14 ± 3	7 ± 2
2-3	MDG + 50 cm FSE+ MPS	139.4	10 ± 2	6 ± 2
Ave.	MDG + 50 cm FSE+ MPS	139.4	12 ± 2	6 ± 1
3-1	MDG + 100 cm FSE+ MPS	154.6	126 ± 12	19 ± 5
3-2	MDG + 100 cm FSE+ MPS	154.4	30 ± 4	7 ± 2
3-3	MDG + 100 cm FSE+ MPS	154.2	49 ± 6	19 ± 4
3-4	MDG + 100 cm FSE+ MPS	154.2	16 ± 3	6 ± 3
3-5	MDG + 100 cm FSE+ MPS	154.4	46 ± 5	12 ± 4
Ave.	MDG + 100 cm FSE+ MPS	154.4	35 ± 15	13 ± 6

4.4.2 Connecting of the membrane system and SISAK detector system

To investigate if the on-line liquid-liquid extraction system consisting of the MDG, FSE and MPS with the SISAK liquid scintillation detector system, alpha spectra generated with the radon, from the earlier described ^{227}Ac source, was measured. The amount of quenching was measured for each of the four different configurations. For these measurements, a ^{137}Cs source was placed on the outside of the LS-cell.

The phases from the MPS had to be kept clean while the system was operating for the MPS to work properly. The strangler was tightened if organic phase leaked into the aqueous phase, and loosened if aqueous phase leaked into the organic phase.

By testing the different connection setups described in chapter 4.2.6, limitations and possibilities about connecting the MDG, FSE and MPS system with the SISAK detector system was discovered. A description of how the different setups performed during multiple tests from 3 to 30 minutes is listed below.

Setup I was a test to see if it was at all possible to connect the liquid-liquid extraction system with MDG, FSE and MPS with the SISAK liquid scintillation detection system. Since no radioactivity was added to this setup, only pure toluene was used in the detector system. In addition, no gas was added to either systems, as only the compatibility of the liquid flows were tested in this setup. The setup worked, and the phases were pure, after adjusting the “strangler”, at a liquid flow of 1 mL/s in the detector system.

First, considering setup II, where the centrifuge degasser was added to the detector system to add ^{219}Rn and ^{215}Po activity with the helium gas. Measurements of the radioactivity mixed into the cocktail by using the centrifuge degasser was performed to test the detector electronics and to get the energy calibration. When the organic phase from the MPS were connected to the T-connector of this system, the backpressure created by the centrifuge degasser and the pump made the phase separation in the MPS unstable. This was the case even if the strangler on the MPS was adjusted often, and at low flow-rates (0.2 – 0.5 mL/s) in the detector system. The combination of the MPS and a centrifuge degasser in the detector system was therefore not an optimal configuration.

By switching to setup III, the increased backpressure caused by the centrifuge degasser was removed, but the phase separation was still unstable. At the gas-flow-rate that was used with the MDG in the rhenium experiment (1.5 L/min), all the gas did not exit at the MDG, but some followed the aqueous phase to the rest of the setup. This setup proved to be problematic to function stably.

To further remove the problem of backpressure, the pump was moved to after the detector as described in setup IV. By placing the pump after the detector and the T-connector to the MDG, FSE and MPS, the pump was pulling the liquid through the detector-cell instead of pushing the liquid through it. This significantly lowered the backpressure, and the phase separation was

now stable for about 30 before ending the test. The system was stable with 1.5 L/min gas flow and up to 1.2 mL/s liquid-flow in the detector system.

Figure 42 shows an α -spectrum measured with setup IV for ~30 minutes, where the scintillator solution flowed in a loop. The second daughter of ^{215}Po is ^{211}Bi , which decays with 6.622 MeV α -emission, has a half-life of 2.14 minutes had then grown in and added to the ^{219}Rn peak.

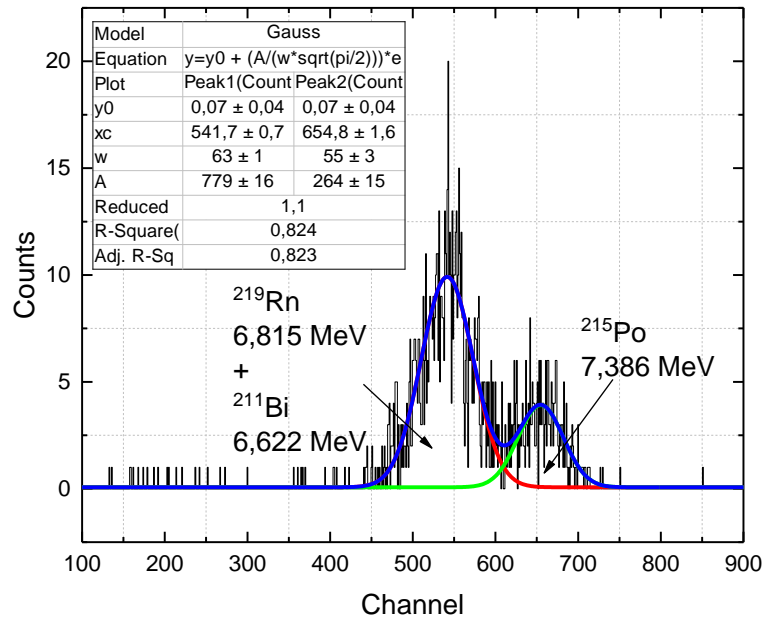


Figure 42: α -spectrum of ^{219}Rn , ^{211}Bi and ^{215}Po , measured with setup IV.

4.5 Discussion

4.5.1 Rhenium

The short half-life of ^{170}Re is comparable to typical super-heavy element nuclei used for chemical studies, e.g. 14.4 s ^{265}Sg [57] and 17 s ^{267}Bh [58]. This makes ^{170}Re ideal to test chemical systems that is later to be used in experiments with superheavy elements.

The measured transport times presented in 4.4.1 shows that there are some residence time when going through both MDG, FSE and MPS. Most notably is the ^{170}Re residence time in the MDG at 11.3 seconds. It would be optimal to lower the residence times before the system can be used for experiments with transactinides seaborgium or bohrium, since these are produced one-atom-at-a-time, unlike ^{170}Re , which is available at 8.2 ± 0.7 kBq/ μA per particle at the chemical apparatus.

Table 10 shows that the chemical yields of ^{174}Re were relatively low and not stable when compared to a previous experiment performed by Y. Komori [1, 2] where the yields were 76 ± 13 % for the 50 cm capillary and 86 ± 5 % for the 100 cm capillary. Run number 3-1 has a chemical yield of 126 % for ^{174}Re , which could be because accumulated ^{174}Re in the MDG was flushed out after changing the to the 100 cm capillary. The chemical yields of ^{170}Re are even lower than the ^{174}Re yields. This can be due to the short half-life of ^{170}Re (9.2 s [49]), since the transport time through the MDG is 11.3 s. Improving the dissolution of the nuclides of interest from the gas into the aqueous phase in the MDG could improve the ^{170}Re chemical yield.

4.5.2 Connecting of the membrane system and SISAK detector system

As presented in Chapter 4.4.2, the only setup where the backpressure was overcome by the organic phase from the MPS was setup IV. This was due to that placing the pump behind the detector-cell, causing the pump to pull the cocktail through the cell instead of pushing it, drastically lowered the backpressure. The reason for this would be that when pulling the liquid through the cell instead of pushing it, the cocktail in the detection system was not pushed past the outlet from the MPS. In addition, the pump would pull on the organic phase from the MPS, thus helping with the phase separation. In this setup, the purity of both the aqueous and organic phase were clean for a period of 30 minutes, compared to the other setups which lasted for a few minutes before the phases were unclean or there were a leak of gas through the MDG.

During the investigation, the amount of quenching varied. However, when the scintillator was bubbled with helium gas before the start of a test, the quenching kept at a low amount for a long time. This could be due to that the O_2 from the organic phase mixing with the cocktail in the detection system is not affecting the systems PSD performance. With a helium-bubbled scintillator cocktail and a low contribution of O_2 from the MPS, the quenching could be kept at a low level.

In conclusion, the configuration in setup IV is a configuration that could be considered for further development towards a chemistry experiment with transactinides. In this investigation, only one detector was included in the setup. In transactinide experiments, up to four detector cells have previously been used [7]. Adding more detector cells will change the setup, but as long as the pump is placed after the feed from the MPS, the problem with backpressure should not be significant. Further testing with this setup could possibly confirm this.

5 Investigation of the maximum cross section of the $^{248}\text{Cm}(^{23}\text{Na},xn)^{271-x}\text{Bh}$ reaction

5.1 Background

In previous bohrium experiments performed by the RIKEN research group, the half-life of ^{267}Bh and ^{266}Bh were investigated, in addition to the cross sections of the $^{248}\text{Cm}(^{23}\text{Na},\text{xn})^{271-\text{x}}\text{Bh}$ reactions [63]. The goal of these investigations has been to optimize for the production of bohrium for use in liquid chemical studies using a gas-jet transport system connected to a recoil separator [64].

To assign detected α -events to a super-heavy element, the daughter nuclei has to be detected in correlation of the α -event. For ^{266}Bh , this means that the daughter nuclei ^{262}Db , which decays with a ratio of 48 % α -emission and 52 % spontaneous fission (SF) [3, 65], would be detected in correlation with the ^{266}Bh event. This would give an α - α or α -sf correlation. If the ^{262}Db decay is by α -emission, the daughter ^{258}Lr decays by α -emission and is detected, it would give an α - α - α correlation. ^{258}Lr decays with a distribution of 97.4 % α and 2.6 % electron capture. The decay pattern of $^{266/267}\text{Bh}$ [3, 65] is shown in Figure 43.

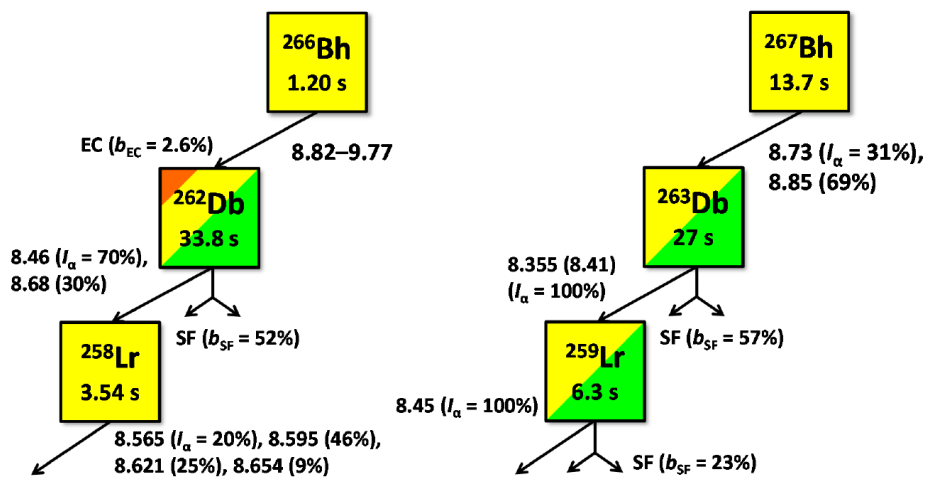


Figure 43: Patterns of decay for $^{266/267}\text{Bh}$ from previous experiments with $^{266/267}\text{Bh}$ at RIKEN and [3, 58, 66-68]. Reprinted from source [3].

In previous experiments on ^{266}Bh at RIKEN, there has been assigned 21 α -correlated events to ^{266}Bh . These correlations has been used to calculate the cross section of $^{248}\text{Cm}(^{23}\text{Na},\text{xn})^{271-\text{x}}\text{Bh}$ at 121.2 125.9 and 130.7 MeV, as shown in Figure 44. If the measured cross sections are fitted with data obtained from the HIVAP code [69, 70], which are also shown in Figure 44. The HIVAP code is a computer code which, by using standard theory for evaporation, takes the competition between proton, neutron, γ - and α -decay into account, in addition to fission. Further description of the HIVAP code is outside of the scope of this thesis, and is described in detail in [70, 71]. Figure 44 makes it clear that the excitation maximum is not accurately determined, since the previous measurements may potentially all lie on the low-energy side.

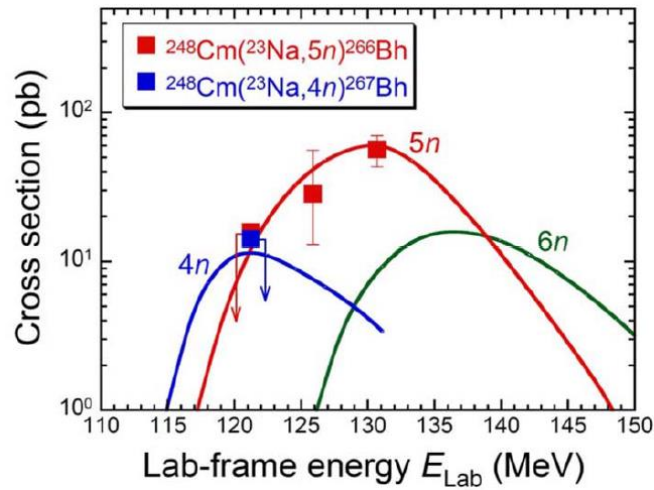


Figure 44: Excitation function of $^{248}\text{Cm}(^{23}\text{Na}, xn)^{271-x}\text{Bh}$. The Curves are calculated by HIVAP code, while the points are the experimentally investigated values. Figure reprinted from source [3].

Therefore, in this work, investigations were done to determine the excitation function maximum of the $^{248}\text{Cm}(^{23}\text{Na}, 5n)^{266}\text{Bh}$ by measuring the cross section at 135.6 MeV beam energy.

The investigations were performed as guest during the beam time of the RIKEN research group, led by H. Haba. All analysis and calculations of the excitation and cross-section were performed by H. Haba [3].

5.2 Methods and instrumentation

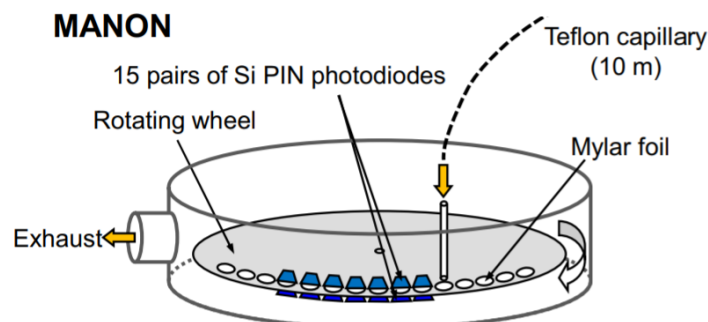
5.2.1 RIKEN Heavy Ion LINAC (RILAC), GARIS and gas-jet transport system

The experiment described here used the same accelerator and preseparator as described in Chapter 4, the RIKEN Heavy Ion LINAC (RILAC) and the preseparator GARIS (Gas-filled Recoil Ion Separator) [48]. The target consisted of $256 \mu\text{g}/\text{cm}^2$ $^{248}\text{Cm}_2\text{O}_3$ on $1.087 \text{ mg}/\text{cm}^2$ Ti backing in eight segments mounted on a rotating wheel with 100 mm diameter. The rotation speed during irradiation was 1000 RPM. The beam from the RILAC was $140.99 \text{ MeV } ^{23}\text{Na}^{7+}$, and the beam energy in the middle of the target was calculated to be 135.29 MeV [3, 4]. Beam intensity was approximately $3 \mu\text{A}$. The magnetic field of GARIS was 14.7 kG , and the helium pressure was 33 Pa . These conditions were calculated [3, 4] to be optimum for separation of the interesting isotopes of bohrium from unwanted reaction products.

The gas-jet system used was as described in Chapter 4. In this part, the Mylar window was $0.7 \mu\text{m}$ thick (procured from Goodfellow) and was resting on a honeycomb support-grid with 78 % transparency. The gas-jet chamber had a diameter of 100 mm and was 20 mm deep. The depth was chosen based on a calculated range equal to $10.0\text{--}14.3 \text{ mm}$ for ^{266}Bh ions in 81.7 kPa helium pressure. The Teflon capillary from the gas-jet chamber to the detector was 10 m long with inner diameter of 2.0 mm . Helium flow-rate was set to $5 \text{ L}/\text{min}$ and the KCl aerosol generator temperature was set to $620 \text{ }^\circ\text{C}$.

5.2.2 Detector system MANON II

For α -spectrometry and fission of the produced bohrium isotopes, a purpose-built detector system for such measurements was used. The system is named “Masurement system for Alpha-particle and spontaneous fission ON line”, abbreviated MANON for short [26]. The Roman numeral II is added to indicate that this is the second such system in use in the research group at RIKEN. A schematic of MANON II is shown in Figure 45. MANON II consists of a large wheel that is rotated stepwise. In the rotating wheel system MANON II,



aerosol particles transported with the gas-jet transport system were deposited on gold coated (50 \AA) Mylar foil of $0.5 \mu\text{m}$ thickness. Four plates with 10 of these foils were placed on the rotating wheel in MANON II (see Figure 80 and 81 in appendix).

Figure 45: Schematic of the MANON II rotating wheel detector system. Figure reprinted from source [26].

15 pairs of “up” and “down” detectors were positioned under and above the rotating plates with Mylar foils. In addition, a single detector were placed under the sampling position. For the experiment resented here, the MANON step-interval was selected to 8.5 s. The system used 0.3 s to move from one position to the next, and during this time the detectors were switched off. Thus, the dead-time of the MANON system was 3.5 %. The detectors were 18 mm * 18 mm Si PIN-photodiodes from Hamamatsu (product number S3204-09). In the mounted position, each had a counting efficiency of 38 % [3, 26], e.g. 76 % for a detector pair. The up detectors had an energy resolution of ~50 keV and the down detectors had a resolution of ~100 keV.

5.3 Analysis, experiment and results

As already mentioned, all analysis and calculations in this part (Chapter 5) of the thesis were performed by H. Haba [3]. The results are included here because it shows the result of the experimental work that was part of this thesis. Furthermore, it illustrates typical super-heavy element data, which a future chemistry system will have to collect and detect, thus setting benchmarks for the system that the current work has participated in preparing.

The products from the RTC were transported to the adjacent laboratory and deposited on the gold-coated Mylar foils on the rotating plates in MANON II. The rotating plates rotated one step each 8.5 s. Each measurement was performed continuously for approximately 12 hours, and between each of the measurements the Mylar foils were changed. In total, there were performed 17 measurements during the beam time.

In Figure 46, the sum of the α -particle spectra measured with the 15 Si up-detectors in MANON II for the entire experiment is shown.

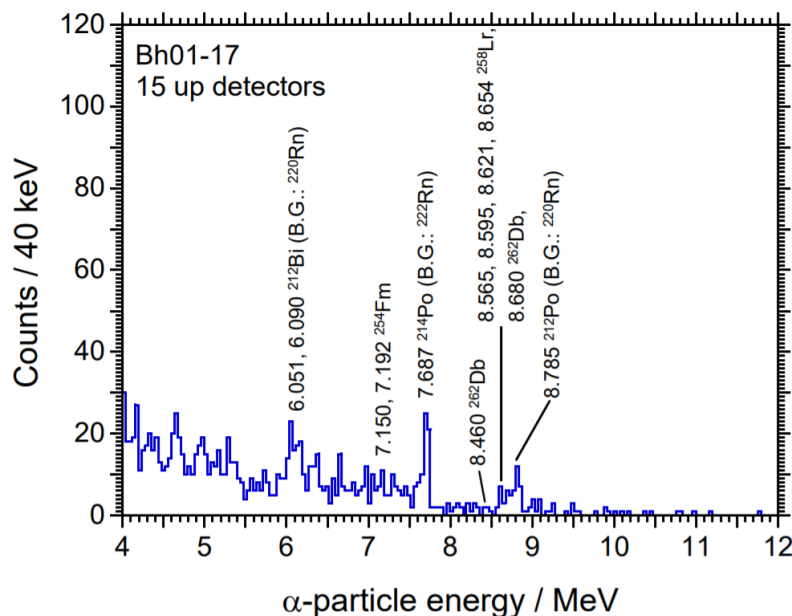


Figure 46: α -particle spectrum measured with the 15 Si up detectors in MANON II. Figure reprinted from source [3].

5.3.1 Measured α -correlations

As mentioned in Chapter 5.1, α -correlations from ^{266}Bh and its daughter(s) must be measured to assign a measured event to it. In Table 11, the α - α - α and α - α correlations observed in this work (161015BT) are shown together with the correlations observed in the previous experiments [3]. Three α - α correlations and two α - α - α correlations were observed during this beam time. Only in the two α - α - α correlations the first event in each correlation had an α -energy between 8.82 – 9.77 MeV and could be assigned to ^{266}Bh . This gives a total of 23 correlations assigned to ^{266}Bh , when including those from previously performed experiments [3, 63].

The number of ^{266}Bh events where ^{262}Db decayed by α -emission was 11, while the number where ^{262}Db decayed by SF was 12. This is relatively consistent with the ratio of the decay pattern of ^{262}Db (α : 48 %/SF: 52%) [3]

Table 11: Observed correlations and random correlations in previous experiments at RIKEN and this work [3], which is marked in yellow.

Beam Time	Energy, MeV	RUN	α - α		α -SF		α - α - α		α - α -SF	
			obs.	RDM	obs.	RDM	obs.	RDM	obs.	RDM
140622BT	130.6	Bh01-10	0	0.16	4	0.02	0	0.00	0	0.00
140622BT	130.6	Bh11-16	2	0.23	1	0.01	1	0.00	0	0.00
150515BT	130.7	Bh01-06	2	0.05	1	0.01	2	0.00	0	0.00
150515BT	130.7	Bh07-11	1	0.06	1	0.01	0	0.00	0	0.00
150515BT	130.7	Bh12-15	1	0.32	0	0.01	1	0.00	0	0.00
151101BT	121.2	Bh01-16	0	0.15	0	0.02	0	0.00	0	0.00
160105BT	130.6	Bh01-14	3	0.28	3	0.06	1	0.00	0	0.00
160616BT	125.9	Bh01-16	1	0.16	3	0.03	0	0.00	0	0.00
161015BT	135.3	Bh01-17	3	0.15	0	0.02	2	0.00	0	0.00

Proper identification of a bohrium-decay event is ensured by identifying the appropriate α -chains following a decay from ^{266}Bh . Thus, an event is identified with the correct energy of *three* alpha particles and a reasonable time delay between them. The statistical probability to accidentally detect such a correlated event, is orders of magnitude lower than simply observing the "correct" energy of an α -particle.

By plotting the observed correlation times, along a logarithmic time line, events belonging to a nucleus with a given half-life will "pile up" and create a time peak centered at the mean decay time. This is a good way to visualise the data and confirm if the correlation times are consistent with the given decay. Using this method, the correlations observed in this work was confirmed to belong to the decay chain $^{266}\text{Bh} \rightarrow ^{262}\text{Db} \rightarrow ^{258}\text{Lr} \rightarrow$. The logarithmic time plots are shown in Figure 47. Here, also previous data are plotted for comparison [3]. The data obtained for the decay of ^{258}Lr , can be compared to data measured when ^{262}Db is produced directly: The time between the alphas from ^{262}Db and ^{258}Lr should be equal to the times observed when ^{266}Bh decays and produces ^{262}Db , unless different metastable states are populated.. The comparison of the time intervals are shown in Figure 47. The α -particle energies of ^{262}Db and ^{258}Lr were also compared to the energies measured in the previous experiment.

The energies of the first α -event in a correlation were set to 8.00 – 10.00 MeV, while those of the second and third α -events were set to 8.00 – 8.77 MeV, since all the α -energies of ^{262}Db and ^{258}Lr measured in the $^{248}\text{Cm}(^{19}\text{F},5n)$ experiment were below 8.77 MeV [65].

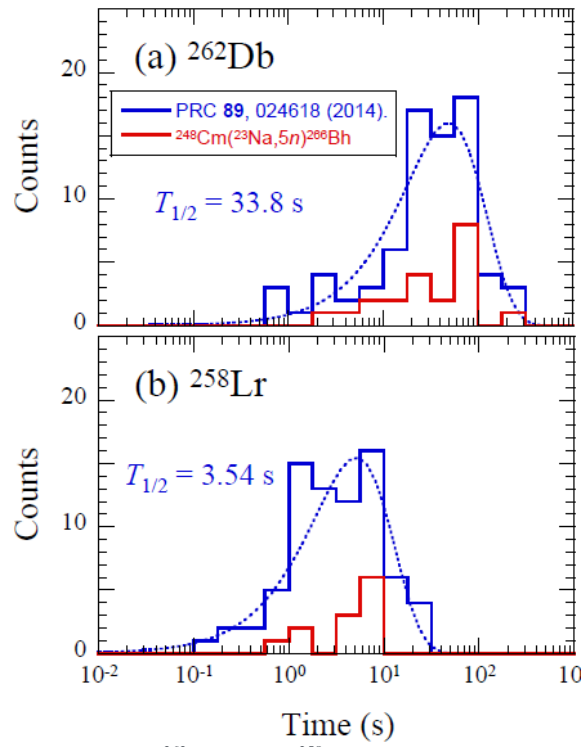


Figure 47: Time interval comparison of (a) ^{262}Db and (b) ^{258}Lr in this work and previous investigations by H. Haba ($^{248}\text{Cm}(^{23}\text{Na},5n)$), shown as the red curve, to a previous experiment with $^{248}\text{Cm}(^{19}\text{F},5n)$, shown as the blue curve [65]. Figure printed from source [3].

5.3.2 Decay properties of ^{266}Bh

From the previous investigations of ^{266}Bh and the investigation in this work, α -particle energies from assigned ^{266}Bh events is spread in the range of 8.62 – 9.40 MeV. The decay times and energies of these events are shown in Figure 48.

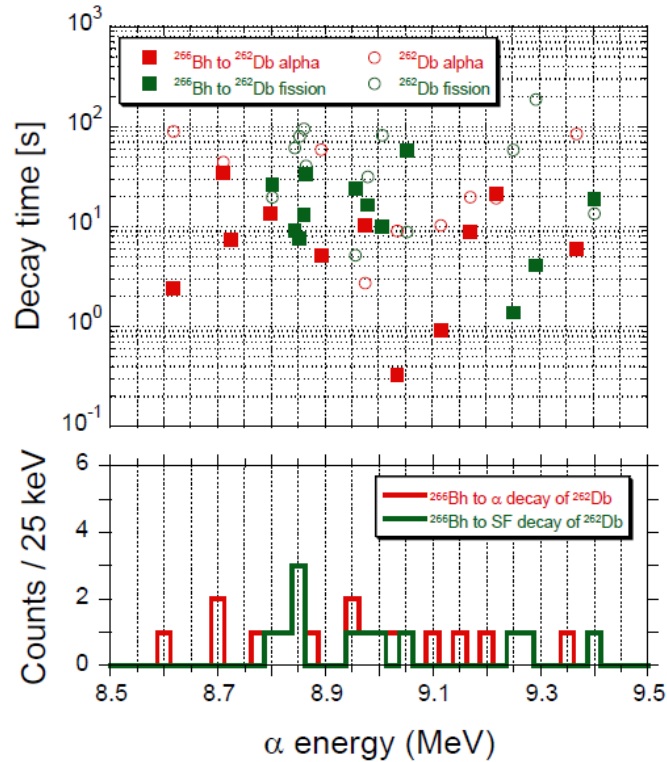


Figure 48: Plot of the decay times and the α -energy spectrum of the ^{266}Bh events measured in this work and previous investigations of ^{266}Bh . Figure reprinted from source [3]

When combining the data from the two assigned triple- α correlations in this work with the 21 assigned previously by the RIKEN research group [3], the spectrum for the time intervals of the 23 assigned ^{266}Bh events is as shown in Figure 49. The half-life of ^{266}Bh when the two new events are included, is $10.0^{+2.6}_{-1.7}$ s. This half-life is one order of magnitude above what has been published by other groups [67, 72].

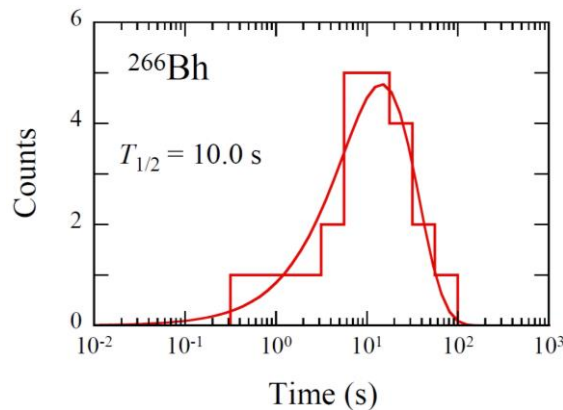


Figure 49: Plot of the time intervals of ^{266}Bh measured during the RIKEN beam times for bohrium production. Figure reprinted from source [3].

5.3.3 Cross section of ^{266}Bh

When the cross section of ^{266}Bh was calculated, these assumptions were made [3]: The half-life of ^{266}Bh is the measured 10.0 s as measured in this experiment, and that ^{266}Bh decays with no branching of spontaneous fission. The transmission of GARIS was assumed to be 15 %, the gas-jet transport efficiency 50 % and the mean transport time of the gas-jet was 2.7 s.

The cross section for ^{266}Bh was, based on these assumptions, calculated to be $15.8^{+20.8}_{-10.2}$ pb at 135.3 MeV beam energy. This result agrees well with the values calculated with HIVAP, which is shown in Figure 50.

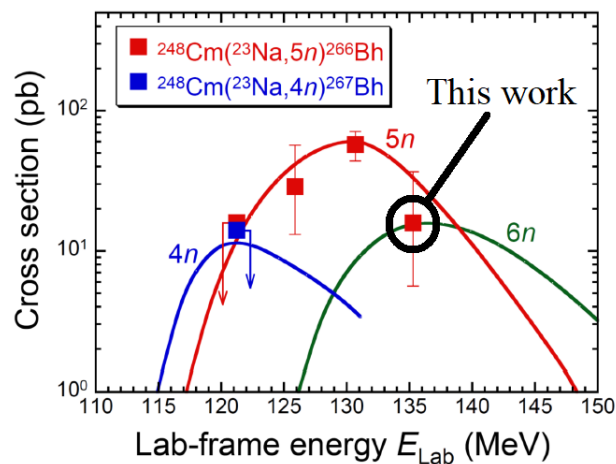


Figure 50: Plot of the excitation function of the $^{248}\text{Cm}(^{23}\text{Na}, xn)^{271-x}\text{Bh}$ reactions compared to the curves showing the HIVAP calculations. The contribution from the investigation performed in this work is marked with a black circle. Figure reprinted from source [3].

5.4 Discussion

The previously observed decay properties of ^{266}Bh and ^{267}Bh and the respective daughters ^{258}Lr and ^{159}Lr shows similar decay properties [58, 65, 66, 72], which makes it difficult to distinguish between the observed correlations. When comparing the measured half-lives with the $^{262/263}\text{Db}$ and $^{258/259}\text{Lr}$ half-lives as seen in Figure 47, the measured events agrees well with the half-lives measured for the daughters of ^{266}Bh [65]. When comparing the α -energies of the daughters, they also agree well with the energies observed in the $^{248}\text{Cm}(^{19}\text{F},5n)$ experiment [65]. In addition, the cross section for the production of ^{267}Bh in the $4n$ reaction is expected to be one order of magnitude smaller than the $5n$ reaction, which makes the presence of ^{266}Bh and its daughter more probable. Therefore, the two correlations measured during the investigation in this work were assigned to ^{266}Bh , in addition to the 21 previously measured by the research group lead by H. Haba.

When comparing the time intervals of the assigned ^{266}Bh events shown in Table 11, to the assignment of ^{266}Bh events in other works [58, 66-68] (Figure 52), the half-life measured in this work is a bit lower. The measured time intervals from K. Morita (2012) and Z. Qin (2006) are shorter than the others, and the data from K. Morita (2012) were from experiments with direct production. This might be making the half-life from the fit of the total of 42 assigned ^{266}Bh events shorter.

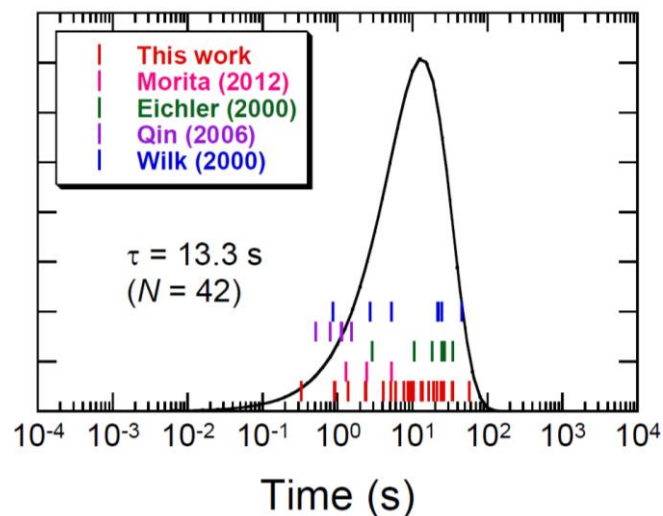


Figure 51: Plot of the time intervals of events assigned to ^{266}Bh from the different works noted in the legend. Figure reprinted from source [3].

When comparing the energy and decay times of the α -events assigned in the investigations lead by H. Haba (including this work), with all the events previously assigned to ^{266}Bh in other works [58, 66-68, 72], there could be a slight trend where the α -events with energy above ~ 9.1 MeV is shorter than the events with energies below 9.1 MeV. This could be indicating that there are more than one isomeric state of ^{266}Bh , or that there are events from ^{267}Bh ($t_{1/2} = 17$ s [58]) included in the measurements. The α -energies and decay times are shown in Figure 53. The half-lives of the ^{266}Bh events measured in H. Haba's investigations are $11.8^{+3.9}_{-2.3}$ s for the α -energies below 9.1 MeV, and $6.1^{+3.6}_{-1.6}$ s for the energies above 9.1 MeV. These half-lives agree with each other, as the lower uncertainty of 11.8 s and upper uncertainty of 6.1 s overlap.

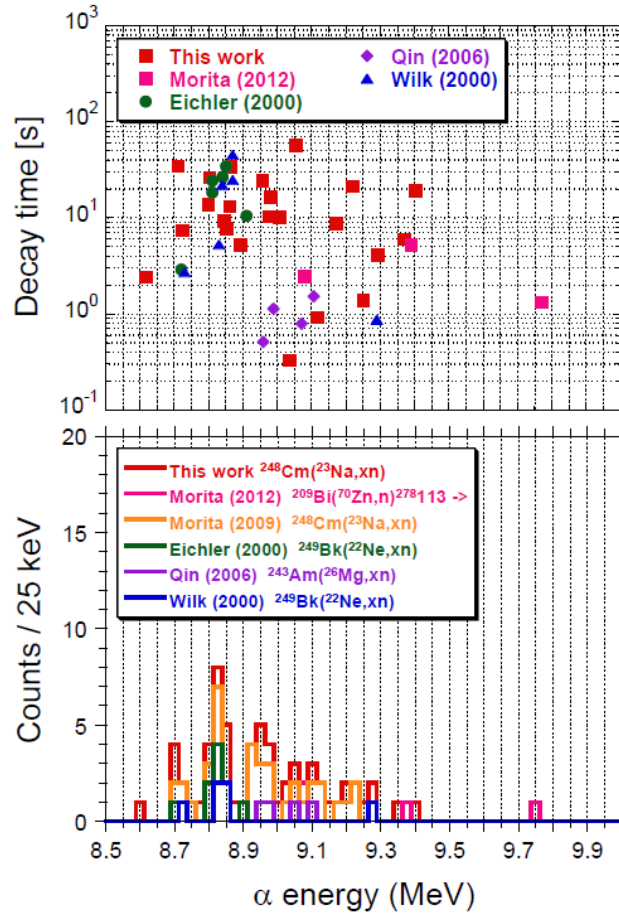


Figure 52: Plot of the decay times and the α -energy spectrum of all assigned ^{266}Bh events [58, 66-68, 72]. Figure reprinted from source [3]

The maximum cross section of the $^{248}\text{Cm}(^{23}\text{Na},5\text{n})^{266}\text{Bh}$ reaction was then compared other works where a ^{248}Cm target has been irradiated with different projectiles. Figure 51 shows that this result agree well with the systematic trend from previously measured $^{248}\text{Cm}(\text{X},5\text{n})$ reactions [3, 57, 65, 73-76].

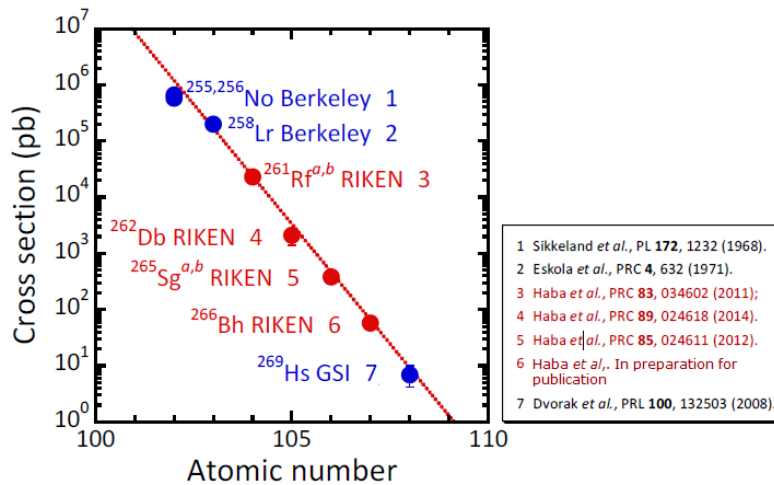


Figure 53: Plot of the maximal cross sections for the $^{248}\text{Cm}(\text{X},5\text{n})$ reactions, with different projectiles as a function of the atomic number of the compound nucleus. The dotted line is an exponential fit. Figure reprinted from source [3].

6 Conclusion and future perspectives

During the work of this thesis, commissioning experiments were successfully performed at the experiment-facility in Řež in the Czech Republic. During these experiments, the production of isotopes of some of the homologues of the super-heavy elements, Tc, Re, W, Mo, Ta and Hf, were performed. The cross sections of the molybdenum isotopes (^{95m}Mo , ^{90}Mo and ^{88}Mo), hafnium isotopes (^{173}Hf , ^{170}Hf and ^{169}Hf), tantalum isotopes (^{174}Ta , ^{173}Ta and ^{172}Ta), tungsten isotopes (^{177}W , ^{175}W and ^{174}W) and rhenium isotopes (^{179}Re and ^{178}Re) produced from natural zirconium-, ytterbium-, lutetium-, hafnium-, and tantalum foils were successfully investigated.

The experiment-facility, which was successfully commissioned, would then be possible to use in future experiments with the homologues of the superheavy elements. A new beam-time at the isochronous cyclotron U-120M, with this experiment-facility, is already planned to be carried out in the beginning of October 2017.

For the experiments performed at RIKEN, the transport time of ^{170}Re through the different parts of the system was successfully investigated. The transport time through the MDG was measured to be a bit too slow to use in experiments with half-lives as short as those of the super-heavy elements ^{265}Sg and ^{266}Bh . The chemical yield of rhenium after going through the Membrane Degasser, Flow Solvent Extraction and Membrane Phase Separator was investigated. The yields were low and unstable, compared to a previous experiment with the same equipment [1, 2]. The MDG must be modified to shorten the transport time and improve the dissolution efficiency, so the chemical yields can be increased.

The combining the Membrane Degasser and Flow Solvent Extraction system with the liquid scintillation detectors previously used in SISAK experiments successfully performed with setup IV. The systems worked well together, as long as backpressure from the detector-cell were kept low. The SISAK liquid scintillation detectors would be possible to use as a detector system for the membrane-based liquid-liquid extraction system. This means that the combination of these two systems could be considered for use in experiments with super-heavy elements if the membrane system is improved, as mentioned in the previous section.

In the “full scale” super-heavy element experiment with bohrium, two triple- α -correlations were observed. The successful investigation of the cross section of the $^{248}\text{Cm}(^{23}\text{Na},x\text{n})^{271-x}\text{Bh}$ reaction, at 135,3 MeV incident beam energy, confirmed the maximum of the excitation function of the $^{248}\text{Cm}(X,5\text{n})$ reaction to be at 130.7 incident beam energy. The maximum of the excitation function can be used to get the highest production yield of ^{266}Bh in future chemical studies of bohrium.

References

1. Komori, Y., *Personal communication Yukiko Komori*, S. Wulff, Editor. 2016-2017.
2. Komori, Y., *161016BT report*. 2017, RIKEN.
3. Haba, H., *Report on 161015BT* 2017.
4. Haba, H., *Personal Communication*, S. Wulff, Editor. 2016-2017.
5. Mendelejev, D.I., *Ueber Die Beziehungen Der Eigenschaften Zu Den Atomgewichten Der Elemente. (Die Beziehungen Zwischen Den Eigenschaften Der Elemente und Ihren Atomgewichten. Die Periodische Gesetzmässigkeit Der Chemischen Elemente.)*. 1895.
6. Offnfopt, U. *Periodic table of elements*. 2017; Own work, Public Domain,]. Available from: <https://commons.wikimedia.org/w/index.php?curid=62296883>.
7. Stavsetra, L., *Achievements using the continuous SISAK α -liquid scintillation technique, and its application in detection of ^{257}Rf atoms*, in *Faculty of Mathematics and Natural Sciences*. 2005, University of Oslo: Oslo. p. 85.
8. Omtvedt, J.P. *Chemical investigation of Super-Heavy Elements (SHEs)*. 2016 13.10.16 [cited 2017 13.09.17]; Available from: <http://www.mn.uio.no/kjemi/english/research/projects/sisak/>.
9. Omtvedt, J.P., *Personal communication with supervisor Jon Petter Omtvedt*, S. Wulff, Editor. 2015-2017.
10. Lerum, H.V., *Preparations for a Reduction and Liquid-Liquid Separation Experiment for Element 106, Seaborgium*. 2014.
11. Ooe, K., et al., *Development of a new continuous dissolution apparatus with a hydrophobic membrane for superheavy element chemistry*. An International Journal Dealing with All Aspects and Applications of Nuclear Chemistry, 2015. **303**(2): p. 1317-1320.
12. Toyoshima, A., et al., *Chemical studies of Mo and W in preparation of a seaborgium (Sg) reduction experiment using MDG, FEC, and SISAK*. Journal of Radioanalytical and Nuclear Chemistry, 2015. **303**(2): p. 1169-1172.
13. Hild, D., et al., *MicroSISAK: continuous liquid-liquid extractions of radionuclides at 0.2 mL/min*. Radiochimica Acta, 2013. **101**(11): p. 681-689.
14. Hild, D., K. Eberhardt, and J.V. Kratz. *MicroSISAK - Improvements of a device for continous liquid-liquid-extraction on a microliter scale*. 2009 13.09.17]; Available from: http://www.kernchemie.uni-mainz.de/downloads/che_7/presentations/hild.pdf.
15. Nilssen, J., *Investigations into new degasser technology for SISAK*. 2009.
16. collaboration, Y.K.f.a.R.-N.U.-J.-U.T.-T.U.-U.O., *Development of a rapid solvent extraction apparatus for aqueous chemistry of the heaviest elements*, in *TASCA15*. 2015: GSI, Darmstadt.
17. Walter Loveland, D.J.M., Glenn T. Seaborg, *Modern Nuclear Chemistry*. 1. ed. 2006, Hoboken, New Jersey: John Wiley & Sons, Inc. 671.
18. W. J. McDowell, B.L.M., *Liquid Scintillation Alpha Spectrometry*. 1994: CRC Press.
19. Horrocks, D.L., *Applications of liquid scintillation counting*. 1974, New York: Academic Press.
20. *Fluorescence_and_Phosphorescence.pdf*. [cited 2017 15.39, 02.03.17]; Available from: https://physik.unibas.ch/Praktikum/VPII/Fluoreszenz/Fluorescence_and_Phosphorescence.pdf.
21. Leo, W.R., *Techniques for nuclear and particle physics experiments : a how-to approach*. 2nd rev. ed. ed. 1994, Berlin: Springer.

22. Wilson, E.J.N., *An introduction to particle accelerators*. 2001, Oxford: Oxford University Press.
23. Burcham, W.E., *Nuclear physics : an introduction*. 2nd ed. ed. 1973, London: Longman.
24. Choppin, G., et al., *Chapter 11 - Mechanisms and Models of Nuclear Reactions*, in *Radiochemistry and Nuclear Chemistry (Fourth Edition)*. 2013, Academic Press: Oxford. p. 313-338.
25. Hermes, F., et al., *Analysis of (particle, xn) reactions on tantalum and gold*. Nuclear Physics A, 1974. **228**(1): p. 175-179.
26. Haba, H., *Superheavy element chemistry at GARIS*. Vol. 131. 2016. 07006.
27. Morita, K., *SHE research at RIKEN/GARIS*. Nuclear Physics A, 2015. **944**(Supplement C): p. 30-61.
28. Schaedel, M., M. Schädel, and SpringerLink, *Chemistry of Superheavy Elements*. The Chemistry of Superheavy Elements. 2003: Springer US.
29. Hoffman, D.C., *Chemistry of the transactinide elements*. 1990, Lawrence Berkeley Lab., CA (USA).
30. Pyykkö, P., *Relativistic effects in structural chemistry*. Chemical Reviews, 1988. **88**(3): p. 563-594.
31. Fure, K., *SISAK ekstraksjonskjemi for grunnstoff 107, bohrium*. 1998, K. Fure: Oslo.
32. J. Magill, G.P., R. Dreher, Z. Sóti, *Karlsruher Nuklidkarte*, in *Chart of the Nuclides 8th edition 2012*. 2012, Nucleonica GmbH: Hermann-von-Helmoltz-Platz 1, 76344 Eggenstein-Leopoldshafen, Germany.
33. Science, N.C.f.A.-B. *RIKEN Heavy Ion LINAC (RILAC)*. [cited 2017 25.04.17]; Available from: http://www.nishina.riken.jp/facility/RILAC_e.html.
34. Samadani, F., *Liquid Chemistry of Hassium Tetroxide using Osmium in Model Experiments with SISAK*, in *Faculty of Mathematics and Natural Sciences*. 2010, University of Oslo: Oslo. p. 58.
35. Breivik, H., *Utvikling av et selektivt kjemisk separasjonssystem for hassium i sentrifugesystemet SISAK*. 2001, H. Breivik: Oslo.
36. Physics, N. *Department of Accelerators Isochronous cyclotron U-120M*. 13.18, 16.02.17]; Available from: <http://accs.ujf.cas.cz/>.
37. CAS, N.P.I.o.t. *Nuclear Physics Institute of the CAS public research institution*. 2010 [cited 2017 25.09.17]; Available from: <http://www.ujf.cas.cz/>.
38. Sturza, J., *Personal communication*, S. Wulff, Editor. 2017.
39. Metals, H.P. *Technical Data Sheet Havar*. [cited 2017 13.52, 21.04.2017]; Available from: <http://www.hpmetals.com/download/Havar.pdf>.
40. Ziegler, J.F. *The Stopping and Range of Ions in Matter*. [cited 2017 30.01.17]; Site with download of the SRIM program and information about the program]. Available from: <http://www.srim.org/>.
41. Ortec. *MAESTRO Multichannel Analyzer Emulation*. 2015; Available from: <http://www.ortec-online.com/products/application-software/maestro-mca>.
42. Corporation, O. *Origin Graphing & Analysis*. [Analysis program] [cited 2016 13.10.16]; Available from: <http://www.originlab.com/>.
43. Bissem, H.H., et al., *Entrance and exit channel phenomena in d- and He3- induced preequilibrium decay*. Physical Review C, 1980. **22**(4): p. 1468-1484.
44. Kondratyev, S.N., et al., *Cross sections of 3He interaction with 93Nb experimental data and possible predictions*. Yad. Fiz., 1996. **59**(12): p. 2121-2135.
45. Ikezawa, E. *RILAC Team*. [cited 2017 25.04.2017]; Description of the components of the RILAC]. Available from: <http://www.riken.jp/en/research/labs/rmc/accel/rilac/>.

46. Science, N.C.f.A.-B. *Discovery of a New Element*. [cited 2017 27.09.17]; Web page of the RIKEN Nishina Center for Accelerator-Based Science about the 113 element and the RILAC]. Available from: http://www.nishina.riken.jp/research/113_e.html.
47. Science, N.C.f.A.-B. *GARIS*. [cited 2017 25.04.17]; Available from: <http://www.nishina.riken.jp/RIBF/GARIS/concept.html>.
48. Haba, H., et al., *RIKEN Gas-filled Recoil Ion Separator (GARIS) as a Promising Interface for Superheavy Element Chemistry—Production of Element 104, 261Rf, Using the GARIS/Gas-jet System—*. Chemistry Letters, 2009. **38**(5): p. 426-427.
49. Meissner, F., et al., *Revision of the decay data of 166–170 Re, including new isomers 167m, 169m Re*. Zeitschrift für Physik A Hadrons and Nuclei, 1992. **343**(3): p. 283-292.
50. Browne, E., *Nuclear data sheets update for A = 174*. Nuclear Data Sheets, 1991. **62**(Supplement C): p. 1-99.
51. Komori, Y., *161016 RILAC 23NaBT plan*, S. Wulff, Editor. 2016.
52. Hult, E.A., *Utvikling av verktøy for SISAK α -væskescintillasjonsanalyse*. 1999, E.A. Hult: Oslo.
53. ORTEC. *Model 552 Pulse-Shape Analyzer and Timing Single-Channel Analyzer Operating and Service Manual*. 2002 [cited 2017 02.10.17]; Available from: <https://www.ortec-online.com/-/media/ametekortec/manuals/552-mnl.pdf>.
54. Corporation, O. *SGompertz fit function*. 2012 [cited 2017 08.09.17]; The description of the SGompertz fitting function]. Available from: <http://www.originlab.com/doc/Origin-Help/SGompertz-FitFunc>.
55. AGENCY, I.A.E., *Radiotracer Residence Time Distribution Method for Industrial and Environmental Applications*. Training Course Series. 2008, Vienna: INTERNATIONAL ATOMIC ENERGY AGENCY.
56. Corporation, O. *LogNormal*. 2012 [cited 2017 08.09.17]; Description of the LogNormal fitting function for Origin]. Available from: <http://www.originlab.com/doc/Origin-Help/LogNormal-FitFunc>.
57. Haba, H., et al., *Production of 265Sg in the 248Cm(22Ne,5n)265Sg reaction and decay properties of two isomeric states in 265Sg*. Physical Review C, 2012. **85**(2): p. 024611.
58. Wilk, P.A., et al., *Evidence for New Isotopes of Element 107: 266Bh and 267Bh*. Physical Review Letters, 2000. **85**(13): p. 2697-2700.
59. Omtvedt, J.P., *Loke*. 2012. p. Aquisition program for α -scintillation spectrometry.
60. *Volund*.
61. Haile, B.G., *Investigation of using γ -ray induced Compton electrons for calibration of α spectra*, in *Department of Chemistry*. 2008, University of Oslo: Oslo.
62. Omtvedt, J.P., *RIKEN UiO_control_system v03 21Oct2016.vi*. 2016. p. Control program for controlling liquid flow, gas flow and valves. Output for the phase purity meters. .
63. Haba, H., *Report on 160616BT*. 2016.
64. Haba, H., et al., *Production and decay studies of 261Rf, 262Db, 265Sg, and 266Bg for superheavy element chemistry at RIKEN GARIS*, in *6th Asia-Pacific Symposium on Radiochemistry*. 2017: Jeju Island, Korea.
65. Haba, H., et al., *Production of 262Db in the 248Cm(19F,5n)262Db reaction and decay properties of 262Db and 258Lr*. Physical Review C, 2014. **89**(2): p. 024618.
66. Eichler, R., et al., *Chemical characterization of bohrium (element 107)*. Nature, 2000. **407**(6800): p. 63-65.
67. Zhi, Q., et al., *Alpha-decay properties of 266Bh*. Nuclear Physics Review, 2006. **23**(4): p. 400-404.

68. Morita, K., et al., *New Result in the Production and Decay of an Isotope, 278113, of the 113th Element*. Journal of the Physical Society of Japan, 2012. **81**(10): p. 103201.
69. Wang, K., et al., *A Proposed Reaction Channel for the Synthesis of the Superheavy Nucleus $Z = 109$* . Chinese Physics Letters, 2004. **21**(3): p. 464.
70. Reisdorf, W. and M. Schädel, *How well do we understand the synthesis of heavy elements by heavy-ion induced fusion?* Zeitschrift für Physik A Hadrons and Nuclei, 1992. **343**(1): p. 47-57.
71. Reisdorf, W., *Analysis of fissionability data at high excitation energies*. Zeitschrift für Physik A Atoms and Nuclei, 1981. **300**(2): p. 227-238.
72. Morita, K., et al., *Decay Properties of 266Bh and 262Db Produced in the 248Cm + 23Na Reaction*. Journal of the Physical Society of Japan, 2009. **78**(6): p. 064201.
73. Haba, H., et al., *Production and decay properties of the 1.9-s isomeric state in 261Rf*. Physical Review C, 2011. **83**(3): p. 034602.
74. Dvorak, J., et al., *Observation of the 3n Evaporation Channel in the Complete Hot-Fusion Reaction 26Mg+248Cm Leading to the New Superheavy Nuclide 271Hs*. Physical Review Letters, 2008. **100**(13): p. 132503.
75. Sikkeland, T., A. Ghiorso, and M.J. Nurmi, *Analysis of Excitation Functions in Cm(C,xn)No Reactions*. Physical Review, 1968. **172**(4): p. 1232-1238.
76. Eskola, K., et al., *Studies of Lawrencium Isotopes with Mass Numbers 255 Through 260*. Physical Review C, 1971. **4**(2): p. 632-642.
77. Viktor Zerkov, N., International Atomic Energy Agency. *Experimental Nuclear Reaction Data (EXFOR)*. 26.04.17 [cited 2016-2017 05.09.17]; Available from: <https://www-nds.iaea.org/exfor/exfor.htm>.

Appendix A - Acronyms and abbreviations

AKUFVE - Swedish acronym “Anordning för Kontinuerlig Undersökning av Fördelingsjämvikter vid Vätskeextraktion” [34] which means “Arrangement for continuous investigations of distribution ratios in liquid-liquid extraction”

BI – Beam Integral

ECR - Electron Cyclotron Resonance

ER – Evaporation Residues

FSE – Flow Solvent Extractor

GARIS – Gas-filled Recoil Ion Separator

HPGe-detector – High-Purity Germanium detector

JAEA – Japan Atomic Energy Agency

LINAC – Linear Accelerator

LS – Liquid Scintillation

MANON - Measurement system for Alpha-particle and spontaneous fission events ON line

MDG – Membrane Degasser

OCL – Oslo Cyclotron Laboratory

MPS – Membrane Phase Separator

PSD – Pulse Shape Discrimination

RFQ - Radio Frequency Quadrupole

RILAC – RIKEN Heavy-Ion Linear Accelerator

RIKEN - Rikagaku Kenkyusho (Institute of Physical and Chemical Research)

RTC – Recoil Transfer Chamber

SISAK - Short-lived Isotopes Studied by the AKUFVE-technique

TOA: Tri-octyl-amine

Appendix B – Propagation of uncertainty

For the propagation of uncertainty, there is the general equation shown in Equation 4. The uncertainty of f , which is a function of variables $a, b, c \dots z$. By using the uncertainties in these variables, $\sigma_a, \sigma_b, \sigma_c \dots \sigma_z$, the uncertainty of f , σ_f , can be calculated.

$$\sigma_f^2 = \left(\frac{\partial f}{\partial a}\right)^2 * \sigma_a^2 + \left(\frac{\partial f}{\partial b}\right)^2 * \sigma_b^2 + \left(\frac{\partial f}{\partial c}\right)^2 * \sigma_c^2 + \dots + \left(\frac{\partial f}{\partial z}\right)^2 * \sigma_z^2 \quad (4)$$

An example in using this equation is under presented for the calculation of the gas-jet transport yields, where DC is the direct catch measurements and AL is the measurements with aluminum foil.

$$\sigma_{Yield} = Yield * \sqrt{\left(\frac{\sigma_{DC}}{DC}\right)^2 + \left(\frac{\sigma_{AL}}{AL}\right)^2}$$

Appendix C - Řež experiments

Calculations and analysis

Calculations for the corrected values from the γ -spectra analysis.

The measured activity from the HPGe-detector had to be corrected for the Beam integral (BI), the intensity of the gamma line (I_γ), the detector efficiency (ϵ) and the half-life of the nuclei, to get the activity at the end of irradiation (A):

Correction for beam integral:
$$A_{BI} = \frac{Net\ counts}{live\ time\ (s) * (mean\ BI\ (\mu A) + 44)}$$

Correction for I_γ :
$$A_{BI, I_\gamma} = A_{BI} * \left(\frac{100\%}{I_\gamma\%}\right)$$

Correction for ϵ :
$$A_{BI, I_\gamma, \epsilon} = A_{BI, I_\gamma} * \left(\frac{100\%}{\epsilon\%}\right)$$

Correction for half-life:
$$A_{Corr.} = A_{BI, I_\gamma, \epsilon} * e^{\lambda t}$$

Calculations for energy loss in the path through the target chamber.

SRIM calculated the amount of energy of the beam in a given material per thickness of that material. The values from SRIM was plotted in Origin as seen in Figure 54 below, and using the marker tool, the x and y values was used to find the loss of energy in the specific thickness of the materials in the target and target chamber.

Setting the marker tool in the correct value of x on the plotted line gave the range of the beam particles in that material. Subtracting the thickness of the material from the range, and then putting the marker tool in the correct y-value on the plotted line then gave the remaining beam energy. This was done for every material the beam went through, including the He-gas the beam entered on the backside of the target.

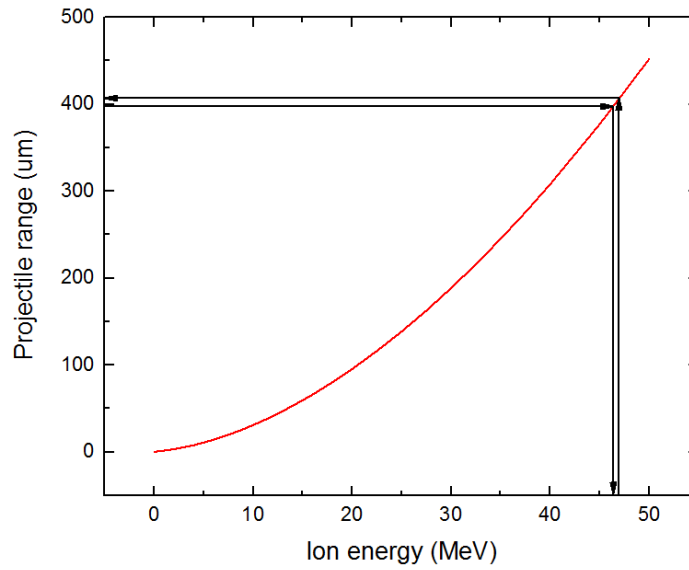


Figure 54: Range of a $^3\text{He}^{2+}$ beam in HAVAR-foil.

The energy of the compound nucleus (E_{recoil}) was calculated based on the energy of the $^3\text{He}^{2+}$ -beam (E_{beam}), mass number of the incident particles (m) and mass number of the target particle (M) as shown in Equation 5 below:

$$E_{\text{recoil}} = \frac{m}{m + M} * E_{\text{beam}} \quad (5)$$

Cross section calculations

To calculate the estimated reaction rate (R) based on cross section (σ) experiments listed in the EXFOR[77], Equation 6 below was applied, where incident particles per second (I), number of atoms in the target (N) and target thickness (x):

$$R = \sigma * I * N * x \quad (6)$$

The reaction rate from this experiment was calculated by using the measured activity (A) at the end of irradiation, the decay constant (λ) and irradiation time (τ) as shown in Equation 7.

$$R = \frac{A}{1 - e^{(-\lambda * \tau)}} \quad (7)$$

Using the calculated reaction rate, the experimental cross sections were calculated by using the rearranged version of equation 4, shown in Equation 8.

$$\sigma = \frac{R}{I * N * x} \quad (8)$$

Pictures of equipment and instruments

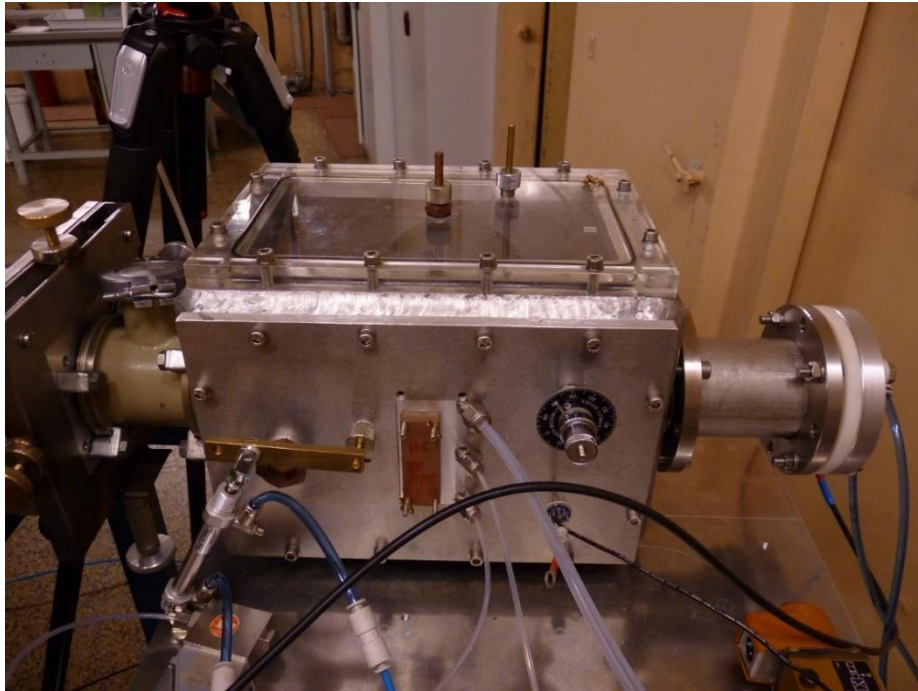


Figure 55: Picture of the outside of the target chamber, on the side where the foils are changed and the gas from the gas-jet system enters and exits.

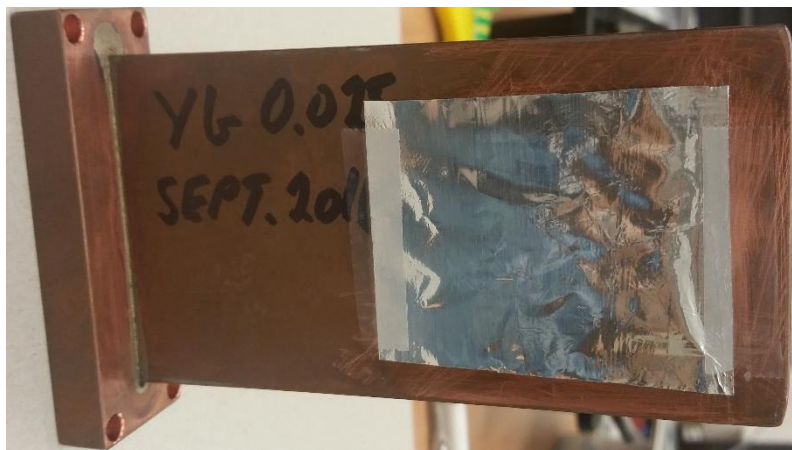


Figure 56: Aluminum foil taped to the back of the ytterbium target holder for aluminum catcher foil experiment.



Figure 57: Setup for direct catch of KCl aerosols.



Figure 58: Step by step placing of glass-fiber filter in filter holder in the direct catch setup.

HPGe-spectrum with lutetium target

Channels of first half of the spectrum (Channel nr.)

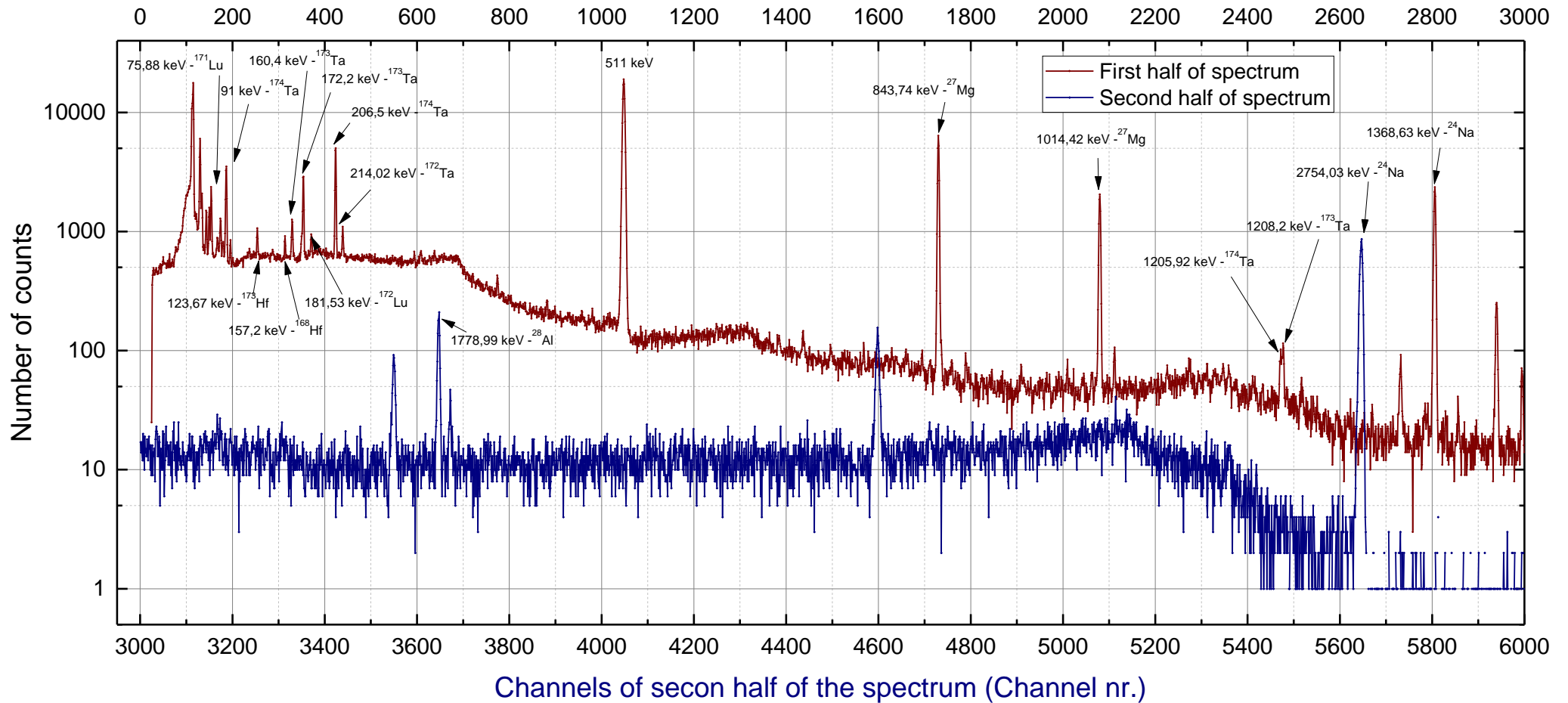


Figure 59: Example of a semi-logarithmic plot of an analyzed HPGe-spectrum. Target irradiated was natural lutetium. First half of the spectra is the red graph in the upper part and the second half of the spectra is the blue graph in the lower part.

Appendix D – Rhenium experiment in RIKEN

Calculations and analysis

Calculations for the corrected values from the γ -spectra analysis.

The measured activity from the HPGe-detector had to be corrected for the Beam intensity (BI), the intensity of the gamma line (I_γ), the detector efficiency (ϵ) and the half-life of the nuclei, to get the activity at the end of irradiation (A):

Correction for beam intensity:
$$A_{BI} = \frac{\text{Net counts}}{\text{live time (s)} * (\text{Beam intensity})}$$

Correction for I_γ :
$$A_{BI, I_\gamma} = A_{BI} * \left(\frac{100\%}{I_\gamma\%}\right)$$

Correction for ϵ :
$$A_{BI, I_\gamma, \epsilon} = A_{BI, I_\gamma} * \left(\frac{100\%}{\epsilon\%}\right)$$

Correction for half-life:
$$A_{Corr.} = A_{BI, I_\gamma, \epsilon} * e^{\lambda t}$$

Analysis of the transport time measurements

Transport through the gas-jet, MDG and 5 + 20 cm capillary

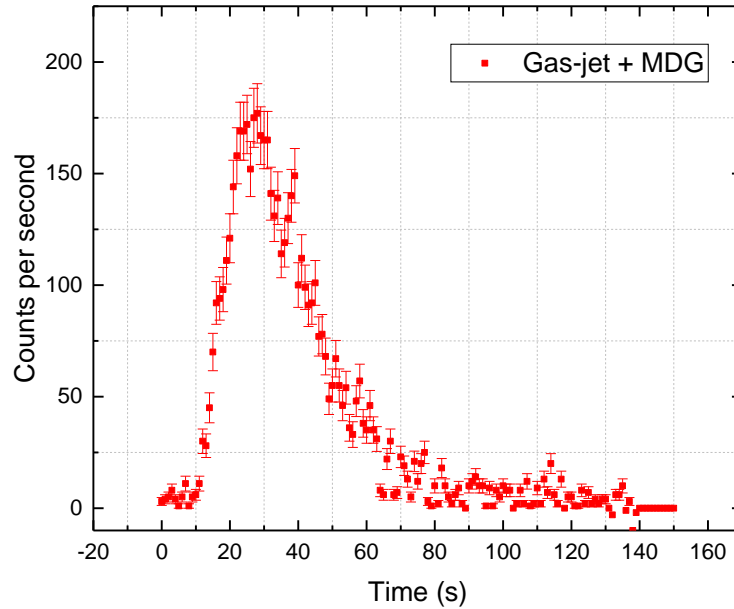


Figure 60: Plot of the added time spectrum of counted ^{170}Re through the gas-jet, MDG and 5 + 20 cm capillary.

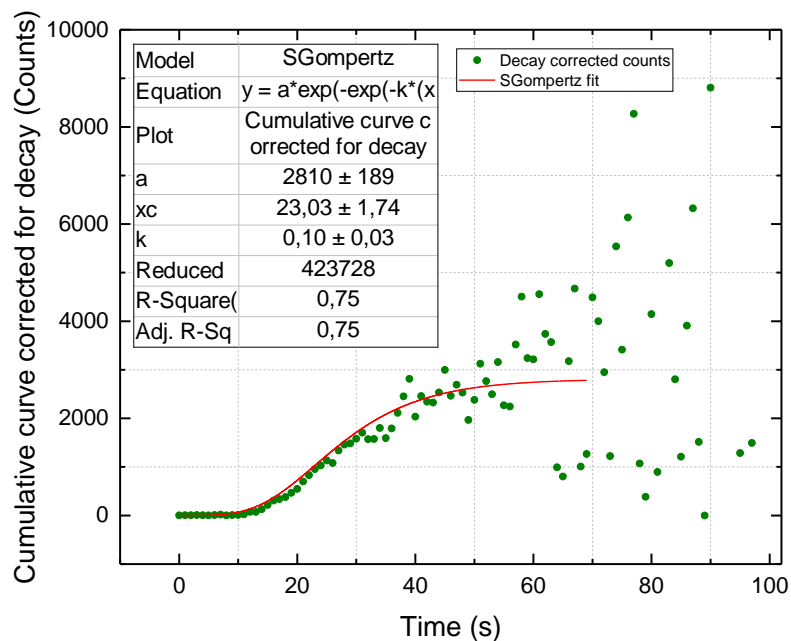


Figure 61: The plot in Figure 60 corrected for radioactive decay. The fitting with SGompertz function (red line) gives the growth curve of the ^{170}Re nuclei collected after the gas-jet, MDG and 5 + 20 cm capillary.

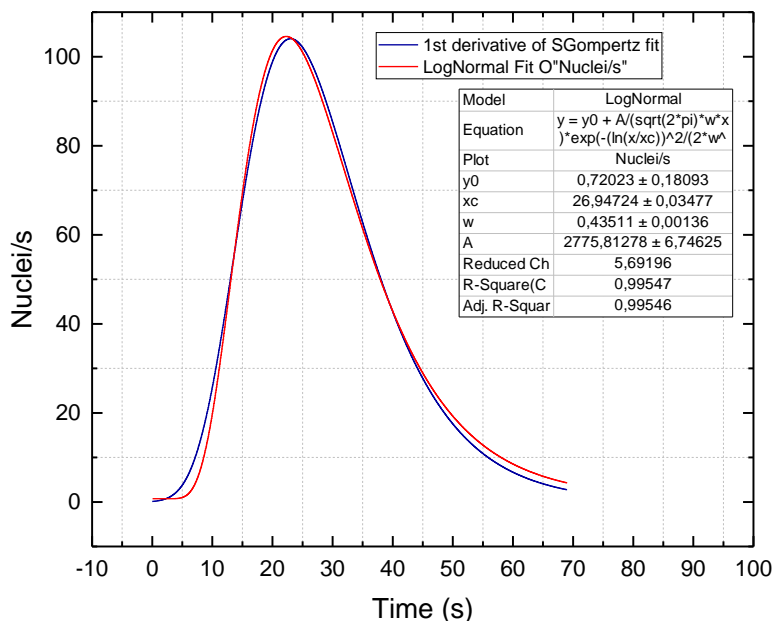


Figure 62: Plot of the derivative of the decay corrected time spectrum of ^{170}Re through the gas-jet, MDG and 5 + 20 cm capillary.

Transport trough the gas-jet, MDG, 5cm capillary and 50 cm FSE

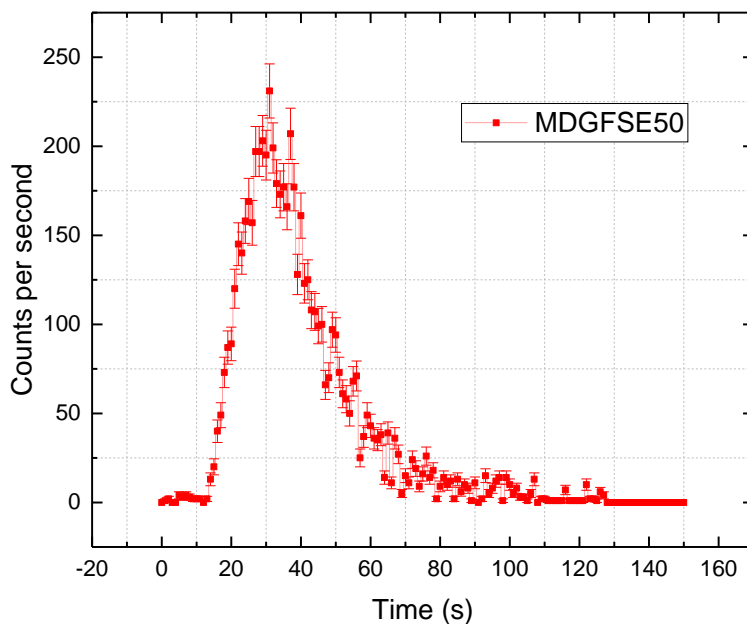


Figure 63: Plot of the added time spectrum of counted ^{170}Re through the gas-jet, MDG, 5 cm capillary and 50 cm FSE.

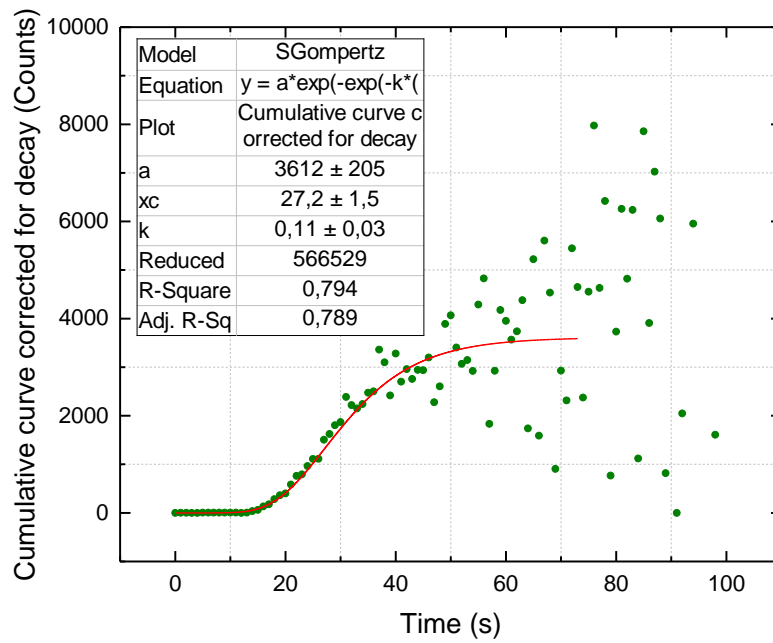


Figure 64: The plot in Figure 63 corrected for radioactive decay. The fitting with SGompertz function (red line) gives the growth curve of the ^{170}Re nuclei collected after the gas-jet, MDG, 5 cm capillary and 50 cm FSE.

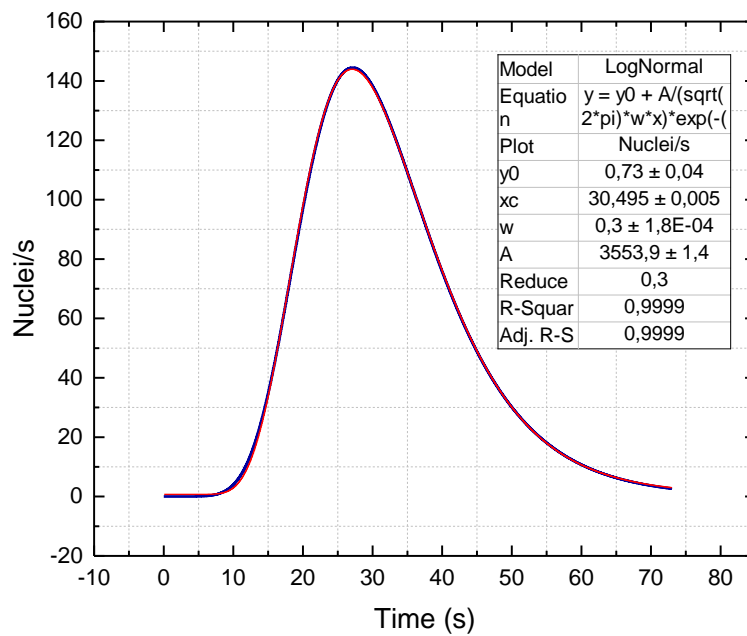


Figure 65: Plot of the derivative of the decay corrected time spectrum of ^{170}Re through the gas-jet, MDG, 5 cm capillary and 50 cm FSE.

Transport through the gas-jet, MDG, 5cm capillary and 100 cm FSE

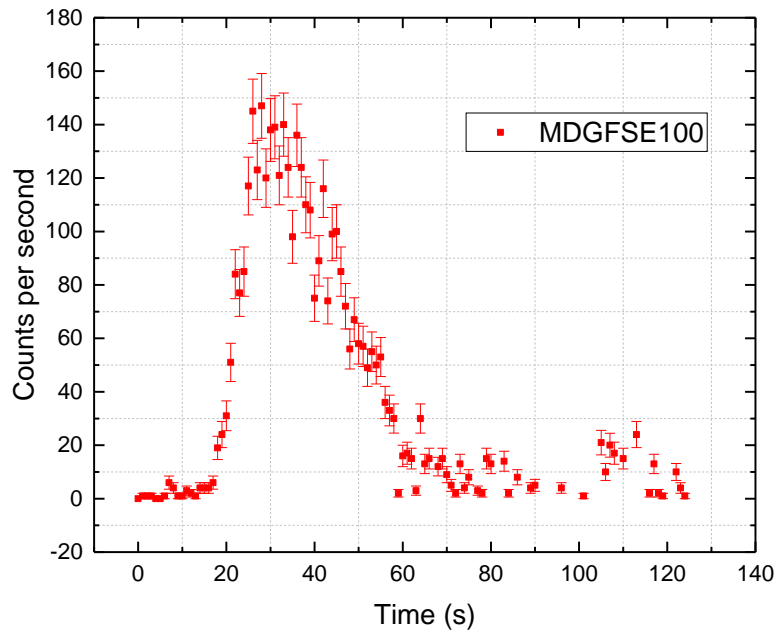


Figure 66: Plot of the added time spectrum of counted ^{170}Re through the gas-jet, MDG, 5 cm capillary and 100 cm FSE.

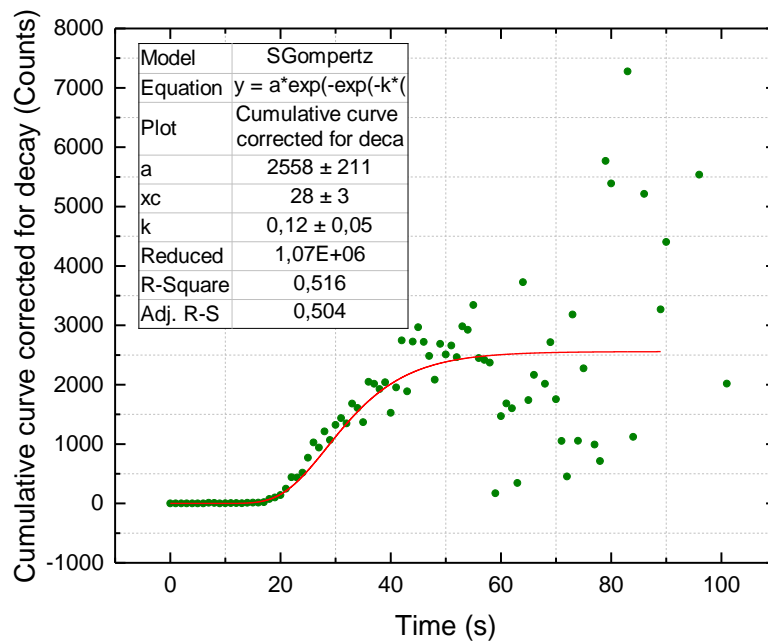


Figure 67: The plot in Figure 66 corrected for radioactive decay. The fitting with SGompertz function (red line) gives the growth curve of the ^{170}Re nuclei collected after the gas-jet, MDG, 5 cm capillary and 100 cm FSE.

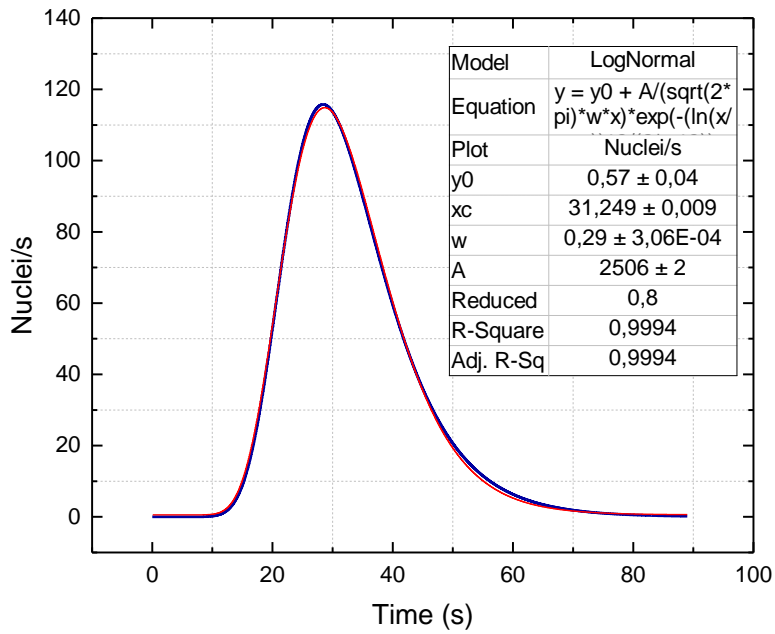


Figure 68: Plot of the derivative of the decay corrected time spectrum of ^{170}Re through the gas-jet, MDG, 5 cm capillary and 100 cm FSE.

Transport trough the gas-jet, MDG, 5cm capillary and 50 cm FSE, MPS and 20 cm capillary

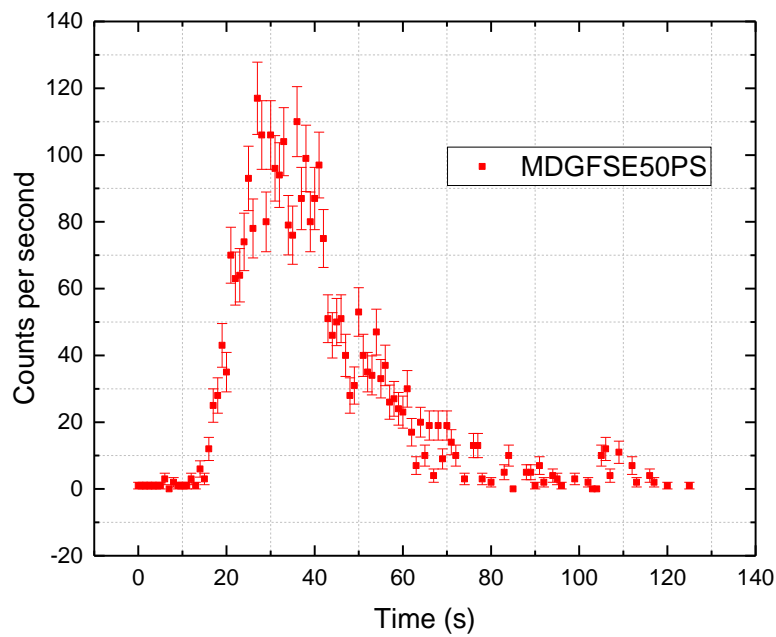


Figure 69: Plot of the added time spectrum of counted ^{170}Re through the gas-jet, MDG, 5 cm capillary, 50 cm FSE, MPS and 20 cm capillary.

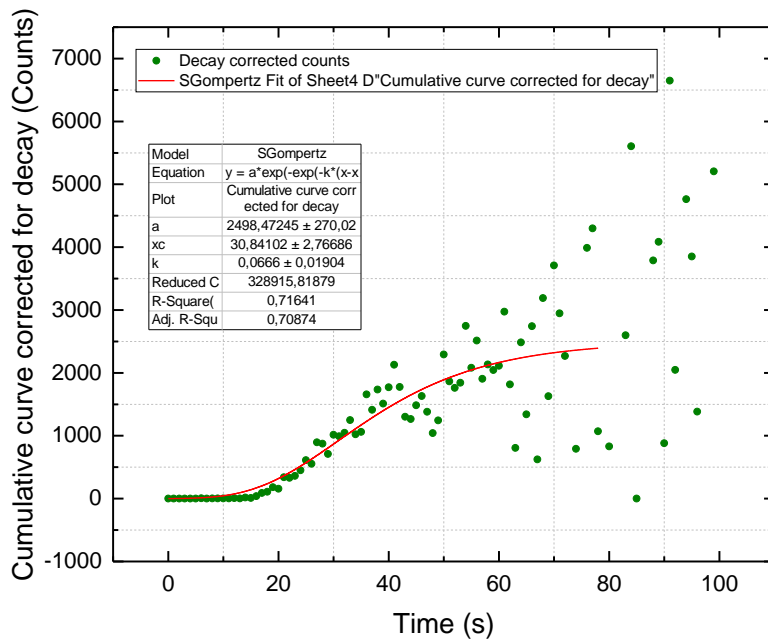


Figure 70: The plot in Figure 69 corrected for radioactive decay. The fitting with SGompertz function (red line) gives the growth curve of the ^{170}Re nuclei collected after the gas-jet, MDG, 5 cm capillary, 50 cm FSE, MPS and 20 cm capillary.

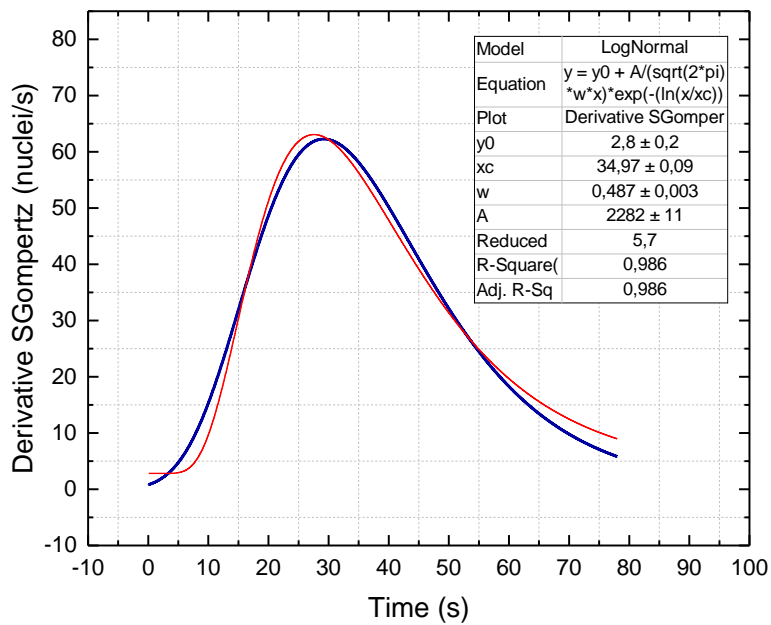


Figure 71: Plot of the derivative of the decay corrected added time spectrum of ^{170}Re through the gas-jet, MDG, 5 cm capillary, 50 cm FSE, MPS and 20 cm capillary.

Transport trough the gas-jet, MDG, 5cm capillary and 100 cm FSE, MPS and 20 cm capillary

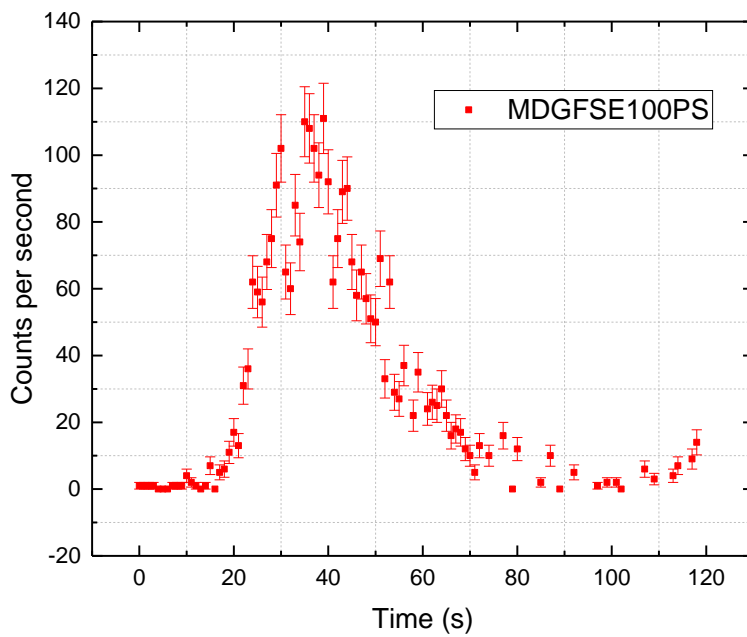


Figure 72: Plot of the added time spectrum of counted ^{170}Re through the gas-jet, MDG, 5 cm capillary, 100 cm FSE, MPS and 20 cm capillary.

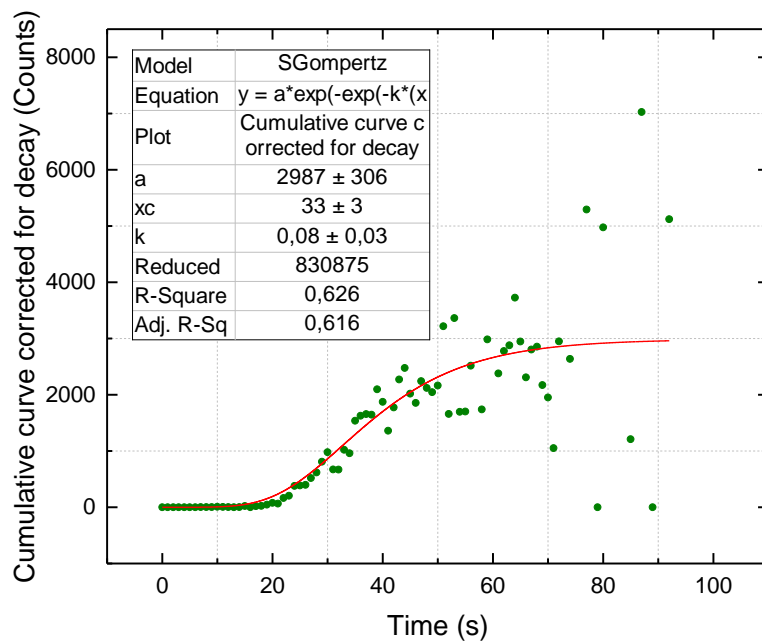


Figure 73: The plot in Figure 72 corrected for radioactive decay. The fitting with SGompertz function (red line) gives the growth curve of the ^{170}Re nuclei collected after the gas-jet, MDG, 5 cm capillary, 100 cm FSE, MPS and 20 cm capillary.

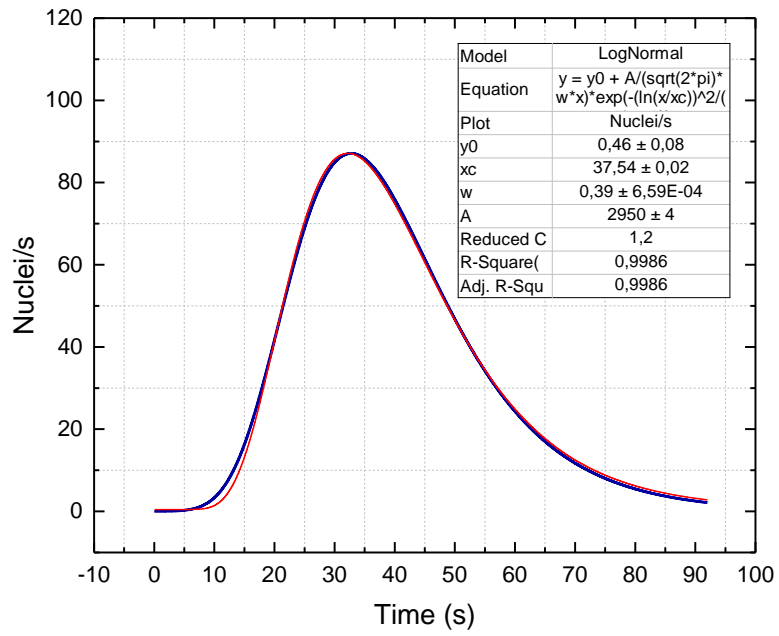


Figure 74: Plot of the derivative of the decay corrected added time spectrum of ^{170}Re through the gas-jet, MDG, 5 cm capillary, 100 cm FSE, MPS and 20 cm capillary.

HPGe-spectrum from rhenium production

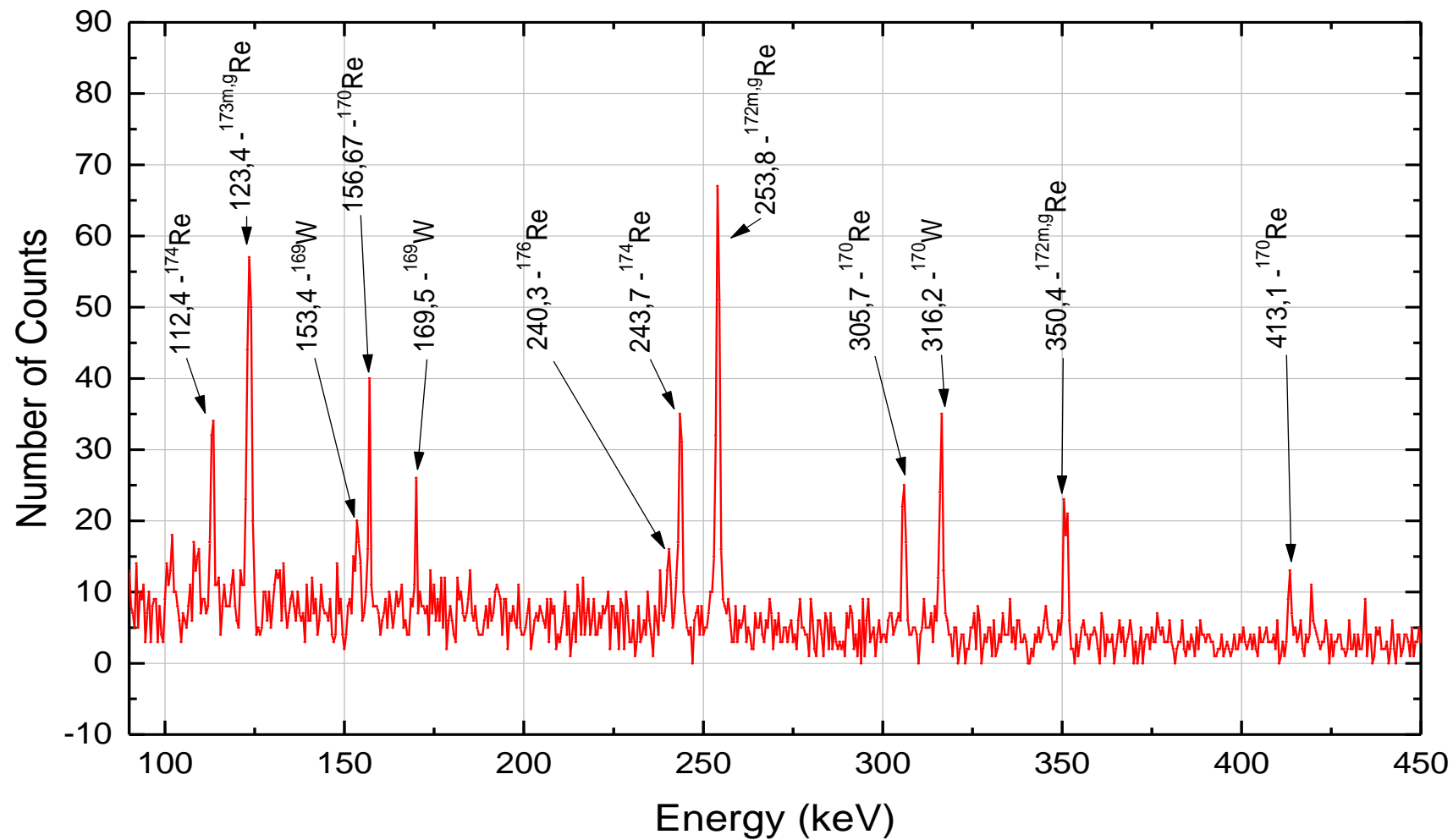


Figure 75: Example of a plot of an analyzed HPGe-spectrum from rhenium production experiment in RIKEN.

Pictures of equipment and instruments



Figure 76: Rotating ^{152}Gd target used to produce rhenium isotopes.

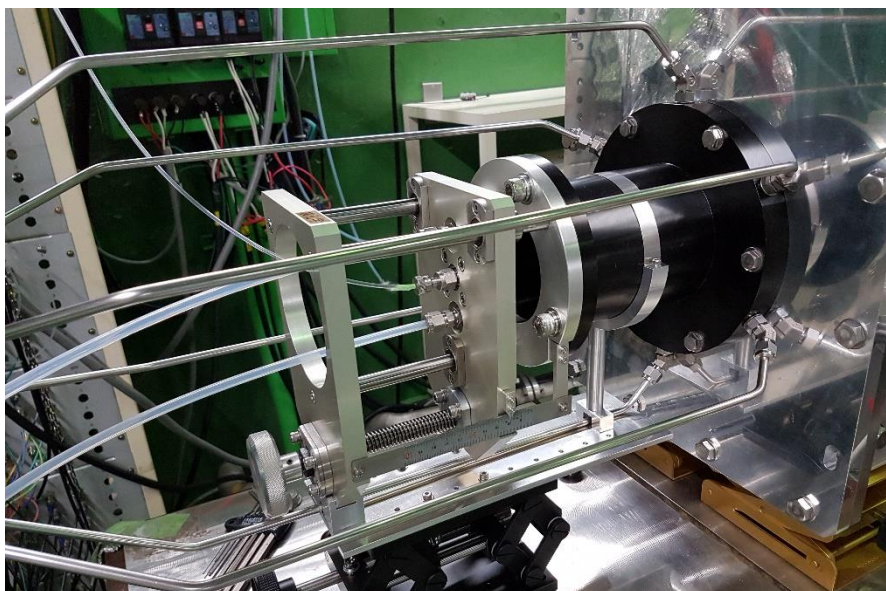


Figure 77: Outside of gas-jet chamber, showing the six gas-in ports on the side of the RTC, and the outgoing gas-jet transport capillary.

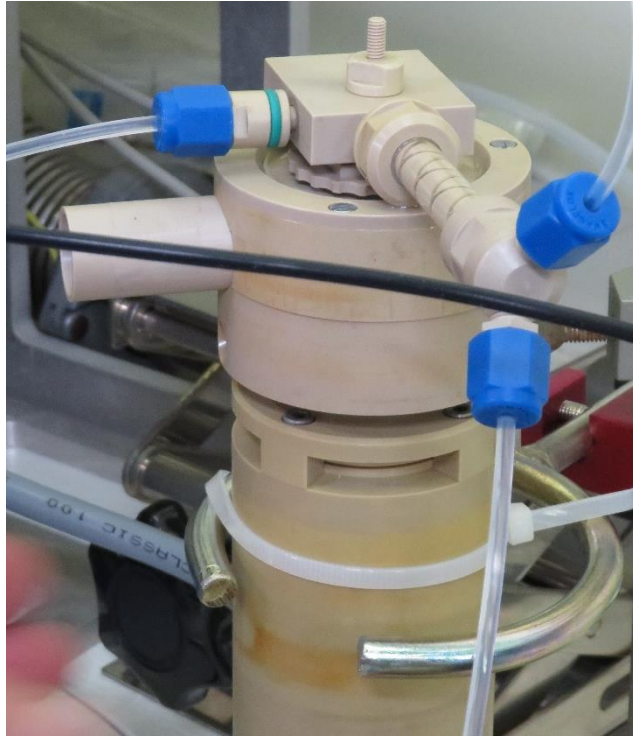


Figure 78: SISA degasser with connected “zigzag” mechanical mixer.

List of chemicals

1.

Name: 1-Methylnaphtalene

Manufacturer: Wako

Lot: KPE0960

Prod. No.: 132-10065

CAS: 90-12-0

Purity: 97 %

Density (20 °C): 1,019-1,025 g/mL

2.

Name: PBBO (2-(4-Biphenyl)-6-phenyl-benzoxazole)

Manufacturer: Sigma-Aldrich

Lot: BCBK1210V

Prod. No.: 14448-25G

CAS: 17064-47-0

Purity: ≥ 98.0 % (TLC)

Melting point: 198-199 °C

3.

Name: Toluene

Manufacturer: Wako

Lot: DSR6721

Prod. No.: 204-01866

CAS: 108-88-3

Purity: 99.5 %

Density (20 °C): 0,864-0,868 g/mL

4.

Name: TOA (Trioctylamine)

Manufacturer: Wako

Lot: LAH0018

Prod. No.: 209-09275

CAS: 1116-76-3

Purity: 97.0 %

Density (20 °C): 0,805-0,812 g/mL

5.

Name: Hydrochloric Acid

Manufacturer: Wako

Lot: LAN1340

Prod. No.: 087-02735

CAS: 7647-01-0

Concentration: 0.05 mol/L

Density (20 °C): 0,998 g/mL

Appendix E – Bohrium experiment in RIKEN

Pictures of equipment and instruments



Figure 79: ^{248}Cm rotating target in target chamber in RIKEN.

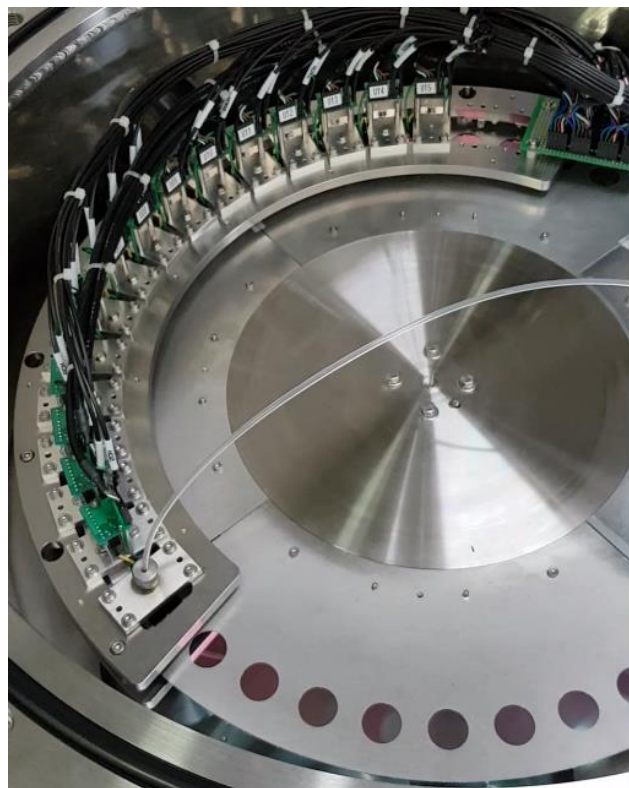


Figure 80: MANON II rotating wheel detector system, showing the rotating gold coated Mylar foils, the capillary from the gas-jet transport system and the 15 up detectors.

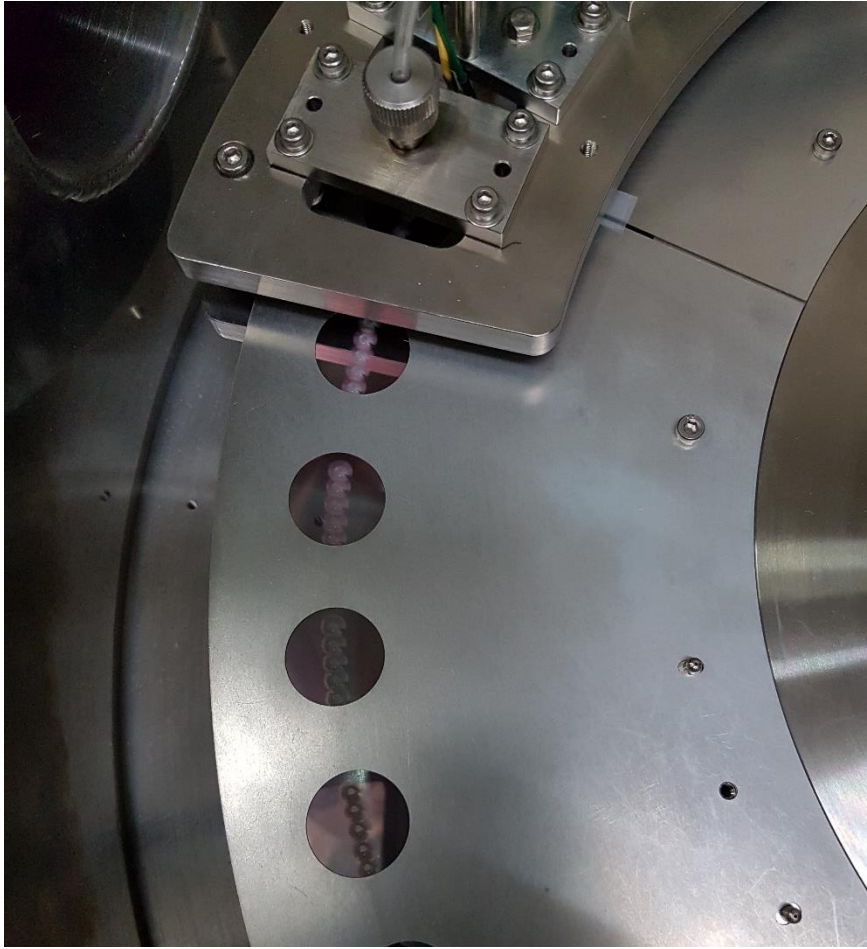


Figure 81: Mylar foils in MANON II after ~12 hours of aerosol collection.

List of Figures

Figure 1: Periodic table of element, where the red square marks the homologues of the super-heavy elements 104-108. Figure reprinted from source [6].	4
Figure 2: Schematic of a simple SISAK setup for continuous liquid-liquid extraction. Figure reprinted from source [8].	4
Figure 3: Schematic of the different possible deexcitation paths of the excited states of an aromatic compound's π -electron system. Figure reprinted from [1].	7
Figure 4: Graph illustrating a scintillator light pulse with a fast and a slow component and the total light output.	8
Figure 5 Schematic of a photomultiplier tube connected to a light guide and a meander detector cell.	10
Figure 6: Schematic of the concept of a cyclotron.	11
Figure 7: Schematic of a linear accelerator.	12
Figure 8: Excitation function for the $^{181}\text{Ta}(^3\text{He},\text{xn})\text{M}$ reaction, where $\text{M} = ^{181}\text{Re}, ^{180}\text{Re}, ^{179}\text{Re}, ^{178}\text{Re},$ and ^{177}Re . The measured values are from the work of Hermes, F., et al.[25].	14
Figure 9: Periodic table of elements, bold line showing the super-heavy elements. Figure reprinted from source [6].	16
Figure 10: The Isochronous cyclotron U-120M at the Řež cyclotron facility.	22
Figure 11: Simple schematic of the target chamber.	23
Figure 12: Schematic of the total setup of the gas-jet system commissioned in the Řež experiments.	25
Figure 13: Target holder with aluminum foil mounted on the back with strips of tape.	26
Figure 14: Example of a semi-logarithmic plot of an analyzed HPGe-spectrum. Target irradiated was natural lutetium. First half of the spectra is the red graph in the upper part and the second half of the spectra is the blue graph in the lower part.	27
Figure 15: Schematic drawing showing compound nuclei made from a beam hitting a target. The reaction to the left happens too far into the target, and the energy of the compound nucleus is not enough to eject it from the target. The two other reactions happens far enough into the target so that the compound nucleus escapes. The reaction in the middle shows a reaction where the compound nucleus has just enough energy to exit the target.	28
Figure 16: Plot of the measured excitation function for the $^{93}\text{Nb}(^3\text{He}^{2+},\text{xn})^{92-95}\text{Tc}$ reactions,, with data from the works of Bissem, H.H., et al.[43] and Kondratyev, S.N., et al. [44].	29
Figure 17: Overview of the RILAC and connected GARIS at the RIKEN Nishina Center for Accelerator-Based Science. The ECR ion source supplies ions that are entered into the RILAC from a variable-frequency RFQ. Figure reprinted from source [46].	38
Figure 18: Schematic of GARIS and the connected gas-jet transport system. Figure reprinted from source [48].	39
Figure 19: Cut through schematic of the Membrane Degasser. Figure reprinted from source [16].	40
Figure 20: Cut through schematic of the Membrane Phase Separator and the connected Teflon capillary. Figure reprinted from source [16].	40

Figure 21: ^{174}Re activity plotted as a function of GARIS' magnetic field.	42
Figure 22: Schematic of the setup for experiments testing the transport time of produced rhenium.....	43
Figure 23: D-values of rhenium isotopes for varying TOA-concentration when extracting from 0.5 M HNO_3 from previous experiments performed by Y. Komori.. Figure reprinted from source [51].	43
Figure 24: Schematic of the supply of helium and ^{227}Ac source, providing $^{219}\text{Rn}/^{215}\text{Po}$ for the connection experiments.....	45
Figure 25: Teflon block meander detector cell for the liquid scintillation detector.....	45
Figure 26: Schematic of the electronics for scintillation detection and pulse shape discrimination. Explanation for the abbreviations: HV – High Voltage, PMT – Photo Multiplier Tube, CSPA – Charge Sensitive Pre-Amplifier, DLA – Delay Line Amplifier, DA – Delay Amplifier, PSD – Pulse Shape Discriminator, TAC – Time to Amplitude Converter, ADC – Analog to Digital Converter, MUX – Multiplexer.	47
Figure 27: Setup I for testing the compatibility of the membrane and detector systems.	48
Figure 28: Setup II for testing the compatibility of the membrane and detector systems.....	49
Figure 29: Setup III for testing the compatibility of the membrane and detector systems.	49
Figure 30: Setup IV for testing the compatibility of the membrane and detector systems.	49
Figure 31: Screenshot from “riken-re-ttime.exe” showing a time-spectrum of a single sorted energy peak from a single list-mode file from transport only through the gas-jet. The gray graph shows the beam, the blue graph shows the total counts in the blue marked peak, the orange shows the counts in the marked background and the green graph shows the blue graph minus the background.	50
Figure 32: Screenshot showing the energy spectrum in "riken-re-ttime.exe" written by Jon Petter Omtvedt. Here the blue marked peak is the peak for the 156 keV γ -ray from ^{170}Re , while the orange marked area is the background above the peak. The x-axis in the energy spectrum are channels with channels corresponding to the energy half the channel number..	51
Figure 33: Plot of the added time spectrum of counted ^{170}Re through the gas-jet.....	52
Figure 34: The plot in Figure 33 corrected for radioactive decay. The fitting with SGompertz function (line) gives the growth curve of the ^{170}Re nuclei collected on the glass-fiber filter on top of the HPGe-detector.....	52
Figure 35: Graph of the true transport function, fitted with the lognormal function. Middle point of the integral of the graph is given as “xc” in the lognormal fit response table in the graph.....	53
Figure 36: Plot of an α -spectrum of ^{219}Rn and ^{215}Po measured with setup II for 5 minutes....	54
Figure 37: Measured Compton spectrum (black line) with plot of the second derivative of the spectrum. Where the second derivative curve crosses zero on the uphill part of the graph is the Compton inflection point.	54
Figure 38: Graphs from the phase purity meters monitoring the phases coming out of the MPS. Graph A shows pure phases, while graph B shows organic phase (green) leaking into the aqueous phase (orange).	55
Figure 39: An example of a typical γ -ray spectrum after 10 seconds of aerosol collection on glass fiber filter.....	56

Figure 40: Graph showing the efficiency of the gas-jet transport of ^{174}Re as a function of the gas-jet chamber pressure for different gas flows and RTC depths.	58
Figure 41: Logarithmic plot of the radioactive decay of the 305.7 keV γ -line from ^{170}Re , fitted exponentially to find the measured half-life of ^{170}Re	59
Figure 42: α -spectrum of ^{219}Rn , ^{211}Bi and ^{215}Po , measured with setup IV.	63
Figure 43: Patterns of decay for $^{266/267}\text{Bh}$ from previous experiments with $^{266/267}\text{Bh}$ at RIKEN and [3, 58, 66-68]. Reprinted from source [3].	69
Figure 44: Excitation function of $^{248}\text{Cm}(^{23}\text{Na},\text{xn})^{271-\text{x}}\text{Bh}$. The Curves are calculated by HIVAP code, while the points are the experimentally investigated values. Figure reprinted from source [3].	70
Figure 45: Schematic of the MANON II rotating wheel detector system. Figure reprinted from source [26].	72
Figure 46: α -particle spectrum measured with the 15 Si up detectors in MANON II. Figure reprinted from source [3].	73
Figure 47: Time interval comparison of (a) ^{262}Db and (b) ^{258}Lr in this work and previous investigations by H. Haba ($^{248}\text{Cm}(^{23}\text{Na},5\text{n})$), shown as the red curve, to a previous experiment with $^{248}\text{Cm}(^{19}\text{F},5\text{n})$, shown as the blue curve [65]. Figure printed from source [3].	75
Figure 48: Plot of the decay times and the α -energy spectrum of the ^{266}Bh events measured in this work and previous investigations of ^{266}Bh . Figure reprinted from source [3]	76
Figure 49: Plot of the time intervals of ^{266}Bh measured during the RIKEN beam times for bohrium production. Figure reprinted from source [3].	76
Figure 50: Plot of the excitation function of the $^{248}\text{Cm}(^{23}\text{Na},\text{xn})^{271-\text{x}}\text{Bh}$ reactions compared to the curves showing the HIVAP calculations. The contribution from the investigation performed in this work is marked with a black circle. Figure reprinted from source [3].	77
Figure 51: Plot of the time intervals of events assigned to ^{266}Bh from the different works noted in the legend. Figure reprinted from source [3].	78
Figure 52: Plot of the decay times and the α -energy spectrum of all assigned ^{266}Bh events [58, 66-68, 72]. Figure reprinted from source [3]	79
Figure 53: Plot of the maximal cross sections for the $^{248}\text{Cm}(\text{X},5\text{n})$ reactions, with different projectiles as a function of the atomic number of the compound nucleus. The dotted line is an exponential fit. Figure reprinted from source [3].	79
Figure 54: Range of a $^3\text{He}^{2+}$ beam in HAVAR-foil.	92
Figure 55: Picture of the outside of the target chamber, on the side where the foils are changed and the gas from the gas-jet system enters and exits.....	93
Figure 56: Aluminum foil taped to the back of the ytterbium target holder for aluminum catcher foil experiment.....	93
Figure 57: Setup for direct catch of KCl aerosols.....	94
Figure 58: Step by step placing of glass-fiber filter in filter holder in the direct catch setup..	94
Figure 59: Example of a semi-logarithmic plot of an analyzed HPGe-spectrum. Target irradiated was natural lutetium. First half of the spectra is the red graph in the upper part and the second half of the spectra is the blue graph in the lower part.	95

Figure 60: Plot of the added time spectrum of counted ^{170}Re through the gas-jet, MDG and 5 + 20 cm capillary.....	98
Figure 61: The plot in Figure 60 corrected for radioactive decay. The fitting with SGompertz function (red line) gives the growth curve of the ^{170}Re nuclei collected after the gas-jet, MDG and 5 + 20 cm capillary.....	98
Figure 62: Plot of the derivative of the decay corrected time spectrum of ^{170}Re through the gas-jet, MDG and 5 + 20 cm capillary.....	99
Figure 63: Plot of the added time spectrum of counted ^{170}Re through the gas-jet, MDG, 5 cm capillary and 50 cm FSE.....	99
Figure 64: The plot in Figure 63 corrected for radioactive decay. The fitting with SGompertz function (red line) gives the growth curve of the ^{170}Re nuclei collected after the gas-jet, MDG, 5 cm capillary and 50 cm FSE.....	100
Figure 65: Plot of the derivative of the decay corrected time spectrum of ^{170}Re through the gas-jet, MDG, 5 cm capillary and 50 cm FSE.....	100
Figure 66: Plot of the added time spectrum of counted ^{170}Re through the gas-jet, MDG, 5 cm capillary and 100 cm FSE.....	101
Figure 67: The plot in Figure 66 corrected for radioactive decay. The fitting with SGompertz function (red line) gives the growth curve of the ^{170}Re nuclei collected after the gas-jet, MDG, 5 cm capillary and 100 cm FSE.....	101
Figure 68: Plot of the derivative of the decay corrected time spectrum of ^{170}Re through the gas-jet, MDG, 5 cm capillary and 100 cm FSE.....	102
Figure 69: Plot of the added time spectrum of counted ^{170}Re through the gas-jet, MDG, 5 cm capillary, 50 cm FSE, MPS and 20 cm capillary.....	102
Figure 70: The plot in Figure 69 corrected for radioactive decay. The fitting with SGompertz function (red line) gives the growth curve of the ^{170}Re nuclei collected after the gas-jet, MDG, 5 cm capillary, 50 cm FSE, MPS and 20 cm capillary.....	103
Figure 71: Plot of the derivative of the decay corrected added time spectrum of ^{170}Re through the gas-jet, MDG, 5 cm capillary, 50 cm FSE, MPS and 20 cm capillary.....	103
Figure 72: Plot of the added time spectrum of counted ^{170}Re through the gas-jet, MDG, 5 cm capillary, 100 cm FSE, MPS and 20 cm capillary.....	104
Figure 73: The plot in Figure 72 corrected for radioactive decay. The fitting with SGompertz function (red line) gives the growth curve of the ^{170}Re nuclei collected after the gas-jet, MDG, 5 cm capillary, 100 cm FSE, MPS and 20 cm capillary.....	104
Figure 74: Plot of the derivative of the decay corrected added time spectrum of ^{170}Re through the gas-jet, MDG, 5 cm capillary, 100 cm FSE, MPS and 20 cm capillary.....	105
Figure 75: Example of a plot of an analyzed HPGe-spectrum from rhenium production experiment in RIKEN.....	106
Figure 76: Rotating ^{152}Gd target used to produce rhenium isotopes.....	107
Figure 77: Outside of gas-jet chamber, showing the six gas-in ports on the side of the RTC, and the outgoing gas-jet transport capillary.....	107
Figure 78: SISAK degasser with connected “zigzag” mechanical mixer.....	108
Figure 79: ^{248}Cm rotating target in target chamber in RIKEN.....	111

Figure 80: MANON II rotating wheel detector system, showing the rotating gold coated Mylar foils, the capillary from the gas-jet transport system and the 15 up detectors. 111

Figure 81: Mylar foils in MANON II after ~12 hours of aerosol collection. 112

List of Tables

Table 1: A list of commonly used solvents and their structure [19].	9
Table 2: Table showing the loss of energy of the beam through the target, the energy of the ejected compound nucleus and the thickness of the active part of the target.	28
Table 3: Activity with uncertainties (unc.) of produced nuclei measured with aluminum catching foil.	30
Table 4: Activity with uncertainties (unc.) of produced nuclei measured with gas-jet system and direct catch.	31
Table 5: List of the yields from transporting the produced nuclei with the gas-jet system.	32
Table 6: Cross sections of the produced nuclei measured with aluminum catching foil.	33
Table 7: Transport yields with uncertainty (unc.) of ^{174}Re in the gas jet system with varying pressure in the gas-jet chamber, 2 or 5 cm gas-jet chamber depth and a helium gas-flow-rate of 1.5 or 5 L/min.	58
Table 8: Total available amounts of ^{170}Re and ^{174}Re at chemistry laboratory in RIKEN after aerosol collection for 10 seconds.	59
Table 9: Mean residence times with uncertainties (unc.) measured through the different parts of the membrane system.	61
Table 10: Chemical yields of ^{170}Re and ^{174}Re through the MDG, FSE (50 or 100 cm) and MPS, with averages and uncertainties (unc.). Run number 3-1 is not included in the average. Reprinted from source [2].	61
Table 11: Observed correlations and random correlations in previous experiments at RIKEN and this work [3], which is marked in yellow.	74